Electronic stopping power of slow ions in solids from first principles

M. Ahsan Zeb

Department of Physics

University of Cambridge

A thesis submitted for the degree of

Doctor of Philosophy

August 2013

Dedicated to my friend Rukhshanda Naheed.

Preface

This thesis describes the work undertaken at the Department of Earth Sciences and Cavendish Laboratory, University of Cambridge between January 2010 and August 2013, under the supervision of Prof. Emilio Artacho. It does not exceed 60,000 words. The research presented is my own work and includes nothing which is the outcome of work done in collaboration or which has been submitted for a previous degree except where specified in the text and Acknowledgements. Parts of this thesis have been published:

1. Electronic Stopping Power in Gold: The Role of d Electrons and the H/He Anomaly. M. Ahsan Zeb, J. Kohanoff, D. Sánchez-Portal, A. Arnau, J. I. Juaristi, and Emilio Artacho, Phys. Rev. Lett. 108, 225504 (2012).
This work is presented in chapter 5.

2. Electronic stopping power of H and He in Al and LiF from first principles. M. Ahsan Zeb, J. Kohanoff, D. Sánchez-Portal, and Emilio Artacho, Nuclear Instruments and Methods in Physics Research Section B: Beam Interactions with Materials and Atoms 303, 59 (2012).
Parts of chapter 6 and 8 are published in this paper.

3. Interplay between spin-orbit coupling and Hubbard interaction in SrIrO3 and related Pbnm perovskite oxides. M. Ahsan Zeb and Hae-Young Kee, Phys. Rev. B 86, 085149 (2012).
This work is done in collaboration with Hae-Young Kee. It is presented as appendix B.

Acknowledgements

I would like to acknowledge great help and support from my supervisor, Emilio Artacho, without which I could not have possibly done the work presented in this thesis. I also owe many thanks to Jorge Kohanoff at Queen's University Belfast in the UK and Daniel Sánchez-Portal at Donostia International Physics Center in Spain for providing me with their TDDFT-Siesta codes and Hae-Young Kee at University of Toronto, Canada for advising me on the work presented in Appendix B. Financial support from Islamic Development Bank Jeddah and Cambridge Commonwealth Trust & Cambridge Overseas Trust is highly appreciated, I am very grateful to these institutions indeed. I would also like to thank my colleagues at Earth Sciences, Cavendish Lab and Clare College for providing me with a friendly environment and emotional support.

Abstract

Coupled electron-ion dynamics, at the Ehrenfest dynamics level, using the time dependent density functional theory with the SIESTA pseudopotential code is used to simulate strongly non-adiabatic process of the passage of slow ions through solids. It is an improvement over a previous method that considers only the electron dynamics, describes the moving ion with its screened Coulomb potential, and places a chain of atomic orbital bases along its trajectory. We consider the projectile and the atoms of the target material on equal footing. That is, just like the target atoms, the projectile is described with its pseudo-potentials and atomic orbital basis is attached to it. This improved description of the process and the projectile leads to a much better agreement with the experiments.

We calculate the electronic stopping power of slow ions with velocity $v \sim 0.05 - 0.50$ a.u. in various crystalline metals and ceramics. Nonlinearities in the velocity dependence of the stopping and the threshold effect are discussed. We find reasonably good qualitative and quantitative agreement with the available experimental data. For H and He ions moving in gold, we also calculate the electron-hole pair spectrum around the fermi level by projecting the time evolved electronic state onto the ground state for the instantaneous nuclear configuration. We find that there is a significant contribution to the stopping from the deep lying d-band states even for a slow projectile. For the series of insulators explored, the material dependence of the threshold and other electronic stopping features are presented. Interesting results are found for the variation with the impact parameter and projectile dependence, especially when comparing sparsely packed with densely packed systems.

Contents

Appendix A

Appendix B

List of Figures

Nomenclature

α	Fine structure constant
$\hbar$	Reduced Plank's constant
ε_e	Electronic stopping cross-section
c	Speed of light in vacuum
e	Elementary charge
E_{KS}	Electronic energy in Kohn-Sham density functional theory formalism
m	Electron mass
r_s	Wigner-Seitz radius, electron density parameter
S_H	Electronic stopping power of H
S_e, S	Electronic stopping power
S_{He}	Electronic stopping power of He
S_n	Nuclear stopping power
v	Projectile velocity
v_0	Bohr velocity
v_F	Fermi velocity
v_{th}	Threshold projectile velocity

Z_1	Atomic number of projectile
Z_2	Atomic number of target element
a.u.	Hartree atomic units
asec	Auto second
DFT	Density functional theory
ED	Ehrenfest dynamics
Fig.	Figure
GGA	Generalised gradient approximation
KS	Kohn-Sham
LDA	Local density approximation
MD	Molecular dynamics
TDDFT	Time dependent density functional theory

Chapter 1

Introduction

1.1 *Passage of charged particles through matter*

Passage of charged particles through matter involves a rich variety of physical phenomena of fundamental as well as technological importance. For example, Rutherford scattering, ionisation and secondary electron emission, Auger effect, bremsstrahlung, defect production, compositional changes, radiation damage and structural phase transformations. Sputtering, ion-implantation and ion-beam mixing are only a few examples of important processes whereby moving ions are employed for materials modification producing materials for modern technological applications.

1.2 *Radiation damage*

Solids have a rigid arrangement of atoms — on a periodic lattice in case of crystalline solids. A charged particle moving through solid that can transfer a few tens of eV energy to these atoms (their nuclei, to be more precise) can displace them from their original position giving rise to vacancies and other point defects in the crystal structure. At higher transferred energies when a displaced atom, usually called primary knocked-on atom (PKA), acquires appreciable kinetic energy and velocity, it can displace more atoms in the solid just like the original charged particle. A displacement cascade develops due to the repetition of this process, producing damage to the initial atomic arrangement. For example, in nuclear waste from the nuclear reactors that consists of radioactive elements, radioactive decays producing swift α-particles along with the recoil atoms damage the structure of the encapsulating material decreasing its durability and strength of withholding the radiations coming out. It is interesting that even a neutron that is electrically neutral can start a cascade by colliding with an atom and setting it in motion or by inducing a nuclear reaction releasing an α-particle. This is exactly what happens inside nuclear reactors where neutrons produce damage to the reactor walls impacting their lifetime.

1.3 *Electronic and Nuclear stopping power*

A charged particle moving through matter interacts with its constituent electrons and nuclei and slows down by losing its kinetic energy to them. The terms projectile and target are usually used for the moving particle and the material it is moving through. While the projectile moves a unit distance, the amount of energy it transfers to the electrons and nuclei of the target are defined as its electronic and nuclear stopping powers in that target material. These are usually denoted by S_e and S_n. For a given target and projectile traversing it (along a specific direction for crystalline solid targets), these quantities depend on the velocity of the latter. Both S_e and S_n first increase and then decrease with velocity, however, as schematically shown in Fig. 1.1, maximum of S_e occurs at much higher velocity than that of S_n. For very slow projectiles with velocity $v << v_0$, where v_0 is the Bohr velocity, nuclear stopping S_n dominates, while for fast projectiles with $v \gtrsim v_0$ nuclear stopping is suppressed and electronic stopping S_e contributes almost exclusively to the energy loss of the projectile.[1] These two velocity regimes are shown in Fig. 1.1.

The energy that a projectile transfers to the nuclei, measured by the nuclear stopping power, is used to work against their potential energy displacing them from their original positions either permanently producing disorder in the structure or just creating vibrations or phonons. On the other hand, the energy that a projectile transfers to the electrons, measured by the electronic stopping power, is used to excite them to the higher energy quantum states raising the effective electronic temperature that helps heal any damage present in the crystal structure.

---

[1] At still higher velocities, radiative losses appear that increase with projectile velocity.

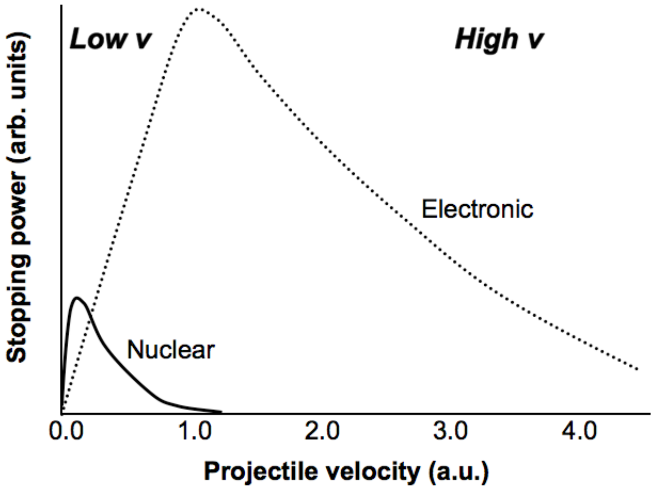

Figure 1.1: Typical dependence of electronic and nuclear stopping on projectile velocity.

Since, as can be seen in Fig. 1.1, appreciable nuclear stopping occurs only at very low velocities, a projectile produce most of the damage when it has sufficiently slowed down, i.e., just before it comes to rest. It seems counterintuitive but a slow moving ion gets a longer interaction time so it can transfer more energy to the target nuclei.

1.4 *Ion ranges in solids*

Ions from a beam incident on a solid penetrate it, slow down, produce damage and finally stop. Even for a beam of mono-energetic ions, various factors, e.g., a range of the available impact parameters for their scattering from the nuclei, lead to a straggling in their range — the total distance travelled, and the penetration depth relative to the target surface. The depth profile and the range distribution are very important quantities that determine, for example, the electronic properties in semiconductor devices doped with the projectile impurity using ion-implantation technique. Similarly, for cancer treatment, radiotherapy to be effective, killing cancerous cells need producing damage to the right region of the target tissue.

1.5 *Including electronic stopping in radiation damage simulations*

Various methods have been developed to calculate the damage to solids on irradiation with ions. Stopping and Range of Ions in Matter (SRIM) program, uses binary collision theory for nuclear stopping with interatomic potentials derived from quantum mechanical calculations and an average fitting to a large number of the available experiments for the electronic stopping [1]. Molecular dynamics simulations can give more insight into the process. Electronic stopping can be included as a friction term in the equations of motion describing the nuclear dynamics [2]. Based on a model given by Caro and Victoria [3], Duffy and Rutherford devised a method [4–8] that also allows transfer of energy from the electronic subsystem back to the nuclei. They couple the nuclear dynamics with a model for the electronic energy that obeys the heat diffusion equation. The energy given to the electrons by the moving ions act as a source term in the diffusion equation while the energy transferred back to the nuclei is controlled by a local Langevin thermostat. As a result, this model is able to describe the defect annealing that tend to repair the damage. Empirical time dependent tight binding model [9, 10] is an efficient way to simulate the quantum dynamics of the electrons coupled to the classical nuclear dynamics [11–16] giving a more accurate picture of the radiation damage event.

1.6 *Channeling*

Trajectories of ions moving through crystalline solids can get aligned to the open channels' axes — the space between the atomic rows or planes. This is called channeling. It is also done purposefully, by aligning the ion beam with a particular crystallographic direction of the target crystal. Under this condition, the projectile avoids small impact parameter collisions with the target ions reducing its nuclear stopping and increasing its range significantly.

1.7 *Electronic stopping of slow ions in solids*

In this thesis we focus on the role of electrons in the projectile energy loss process, i.e., the electronic stopping power. In the high velocity regime shown in Fig. 1.1, the problem of projectile energy loss is relatively transparent and simple. A fast enough positively charged projectile cannot keep bound electrons with it. It is quite like a structureless point object with its bare charge and unscreened Coulomb potential. This simplifies the theory. After the work of a large number of people over many decades we now have Bohr-Bethe-Bloch formula that gives very accurate values of electronic stopping power at high projectile velocities. We will give a brief description of it in chapter 2.

In contrast to this, in the low velocity regime screening of the projectile charge by the target electrons is very effective and the character of the electronic states bound to the projectile, i.e., projectile's atomic electronic structure, is a major player in the problem. The projectile is no more a structureless point object but a complex entity with a significant size. The extent of screening and hence the effective charge and size of the projectile depend on its velocity as well as on the electronic structure of the target material. This means that the projectile, the moving object, is not a fixed entity but its very own nature depends on its velocity and the stopping medium or target material.

1.7.1 *Theory vs experiment*

Several theories and methods that we briefly review in chapter 2 have been developed to calculate the electronic stopping power S of slow projectiles. Except a model developed based on the density of electronic states [17], a common feature to the methods that do not consider explicit dynamics of the electrons is that they lead to a velocity proportional electronic stopping power, i.e., $S \propto v$. Perhaps the most accurate of these methods is based on quantum scattering of electrons at the fermi surface from the screened potential of the projectile that is obtained using density functional theory [18, 19]. For a free electron gas or jellium model of solids, these non-linear calculations for stopping of slow H and He, S_H and S_{He}, show a cross-over between two regimes: for a low electron density with $r_s > 2.77$, where r_s is Wigner-Seitz radius, $S_H > S_{He}$, where as for a higher electron density with $r_s < 2.77$, the converse it true. This is shown in the left panel of Fig. 1.2.

A velocity proportional stopping has been observed experimentally in many free-electron-like *sp*-bonded metals [22, 23] and the jellium model has allowed a deep understanding of the dynamic screening of the projectile and its relation to

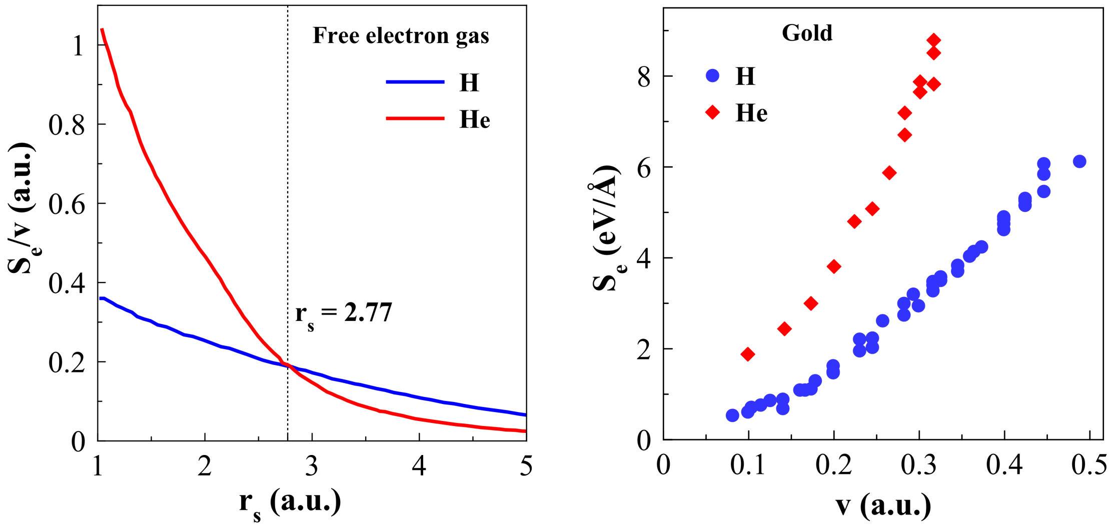

Figure 1.2: Left: Electronic stopping power of slow H and He in jellium as a function of electron density showing a cross-over at $r_s = 2.77$, taken from Echenique et al., Ref. [18]. Right: Experimental results for gold taken from Refs. [20, 21] showing non-linear velocity dependence of electronic stopping power.

the stopping phenomenon [24]. Even the jellium prediction of an oscillation of the proportionality coefficient with the projectile's atomic number Z_1 has been verified [25] and reproduced by ab initio atomistic simulations [26]. However, phenomena that cannot be accounted for within the jellium paradigm have been described only qualitatively so far [17, 27–29]. Experiments on noble metals Cu, Ag and Au, show pronounced nonlinearities in $S_e(v)$ [20–22, 27, 30–32]. For example, in the case of slow H and He ions in gold, $S_e(v)$ is shown in the right panel of Fig. 1.2. It displays an increase in the slope roughly around $v \simeq 0.18$ a.u. [20, 21, 32]. This is usually attributed to a threshold projectile velocity v_{th} needed to excite the d-band electrons that are relatively tightly bound. That is, below v_{th}, only the s-band electrons are considered to contribute to the stopping. But, this also means $r_s = 3.04 > 2.77$ for $v < v_{th}$ that should give $S_{He} < S_H$, which is not true — $S_{He} > S_H$ down to very low velocities $v \sim 0.05$ a.u.. Similarly, it is very interesting that in Al that is an sp-bonded metal for which jellium model works well for H, i.e., $S_H \propto v$, $S_{He}(v)$ shows three regimes with different slopes [33]. These flagrant discrepancies with the established paradigm for such problems [18, 25] demand a more complete theory that can capture all the essential physics behind the non-adiabatic processes of energy transfer from the projectile to the target electrons and give us an insight into the problem.

1.7.2 *Threshold effect in insulators*

Electronic stopping of slow projectiles in insulators is expected to get severely suppressed below a threshold velocity due to the fact that the valence and the conduction bands in the latter are separated by a band gap requiring a finite amount of energy to create electronic excitations. The threshold velocity v_{th} and the velocity dependence of the electronic stopping around it depend on the projectile-target system. These are hard to observe experimentally due to technical problems at very low velocities. However, calculations show that the electronic stopping kicks off with a high power of projectile velocity [34, 35].

The band gap of target insulator is affected by the presence of the projectile. Calculation on LiF (band gap $\sim$ 14 eV) shows that a proton reduces its band gap by $\sim$ 2 eV while an antiproton closes it [36]. This is supposed to be the reason that the earliest experiments [37] on slow H in Al_2O_3, SiO_2 and LiF did not see the effect down to very low projectile velocities ($v = 0.33$ a.u.) even though all these target materials are wide band gap insulators. Later experiments covering velocities down to 0.2 a.u. also found no threshold effect [38, 39] except under grazing incidence, which showed a threshold velocity of $v \simeq 0.2$ a.u. in LiF[40]. Recently, measurements at velocities as low as 0.1 a.u.[41, 42] found a clear velocity threshold. First-principles simulations [29] based on TD-DFT were able to reproduce the behaviour, albeit with a clear underestimation of the stopping power and overestimation of the threshold. In this thesis, for the projectile-target systems for which the electronic stopping remains significant at the lowest velocity considered, we find that it usually goes down with velocity linearly. That is the reason that we linearly extrapolate our results to estimate the threshold velocity in such cases.

1.7.3 *First principles simulations*

First-principles calculations provide predictions of varied ground state properties within a few percent accuracy. However, despite a long history, our ability to perform predictive theoretical simulations of non-adiabatic processes coupling many adiabatic energy surfaces is very much behind what has been accomplished for adiabatic situations. A substantial progress has only been made for weakly non-adiabatic problems such as the chemistry of vibrationally excited molecules landing on metal surfaces [43], but not in the stronger coupling regime of the electronic stopping.

Recently, simulating the electron dynamics explicitly using time dependent density functional theory with real-time evolution of the electronic wavefunction has been very successful for study of electronic stopping phenomena [29]. SIESTA code [44–46] was used that employs pseudopotentials and the numerical atomic orbital basis set. The projectile was described with its screened Coulomb potential moving at constant velocity and a chain of atomic orbital bases was placed along its trajectory. As the dynamics of ions was not considered, all the target atoms were fixed.

1.7.4 *Coupled ion-electron dynamics*

We upgrade this method by simultaneouly considering, on the Ehrenfest dynamics level, the ion dynamics so that we can simulate the coupled ion-electron dynamics of a system of ions and electrons. This means that for simulating the passage of ions through solids, we can now use the projectile atom described by its pseudopotentials with attached basis orbitals just like the target atoms. This improved description of the process and the projectile lead to a much better quantitative agreement with the experiments [47, 48] showing that this method can give usual first-principles accuracies for strongly coupled non-adiabatic processes in condensed matter.

1.8 *Thesis structure*

In the next chapter we briefly review the current theories and methods used to calculate the electronic stopping both in the high velocity regime and in the low velocity regime. Our method is described in detail in chapter 3 while we explain some important relevant technical details in chapter 4. We present our results for the electronic stopping power of H and He in gold in chapter 5. In the same chapter, we also present our results for the evolution of the excitation spectrum as the projectile excites more and more electrons above the fermi surface. Results for the electronic stopping of H and He in Al and Na are given in chapter 6 and 7. We consider three different impact parameters in Al while two cases, the bulk and a 8 unit cell thick film for Na.

Insulators are considered in chapters 8 and 9. In chapter 8, we calculate the stopping of the same two projectiles, H and He, in LiF and compare our results with previous SIESTA-TDDFT calculations [29]. We also see the effect of low impact parameter trajectories on the stopping in this chapter. More insulators — quartz, magnesia, zircon, alumina and SiC — are considered in chapter 9. We present our results for the electronic stopping of H and He in various channels of α-quartz sampling a range of impact parameters. The same two projectiles are considered in magnesia and zircon, while in alumina we also consider Li. For SiC, electronic stopping of gold is presented. The summary, conclusion and outlook is given in chapter 10. Appendix A gives some supplementary details related to chapter 5. I also worked on a smaller project that is not related to the title of this thesis. It is included at the end as Appendix B.

Chapter 2

Electronic stopping

A Brief Review

When a projectile propagates in a material, electrons are scattered off its screened Coulomb potential. A slow projectile tends to neutralise itself by capturing electrons from the target material, while a fast projectile tends to lose its electrons. Whether a projectile would be considered slow or fast depends on the mean orbital speed of its atomic electrons. Bohr used Thomas-Fermi model of atom and suggested that the projectile would lose all its electrons at $v > Z_1^{2/3} v_0$, while at $v < Z_1^{2/3} v_0$, the charge on the projectile would increase linearly with velocity [49–51]. Here, Z_1 is the atomic number of the projectile and v_0 is the Bohr velocity. In different velocity regimes, different approximations are employed to calculate the energy loss of a projectile. In the following we present some theories that have been developed to calculate the electronic stopping power.

2.1 High velocity regime

At $v > Z_1^{2/3} v_0$, the projectile is a bare nucleus that interacts with the target electrons through its unscreened Coulomb potential. Bohr assumed [52–54] that during the passage of such a fast projectile, the target electrons do not move and their interaction with the projectile imparts only a transverse momentum impulse to them. As the projectile moves a distance dx, the corresponding change in momentum Δp of a target electron, using classical mechanics, is given by $\Delta p = \int F_\perp dt$. Here, $F_\perp$ is the Coulomb force on the electron transverse to the projectile motion and $dt = dx/v$ is the interaction time. For an impact parameter b and normal distance between the projectile and the electron x, $F_\perp = \frac{Z_1 e^2}{x^2+b^2}\frac{b}{\sqrt{x^2+b^2}}$ (in Gaussian units). Substituting these values of $F_\perp$ and dt, we obtain

$$\Delta p = \int_{-\infty}^{+\infty} \frac{Z_1 e^2}{x^2+b^2}\frac{b}{\sqrt{x^2+b^2}}\frac{dx}{v} = \frac{2Z_1 e^2}{vb} \tag{2.1}$$

The electron gets a kinetic energy T, given by

$$T = \frac{\Delta p^2}{2m} = \frac{2Z_1^2 e^4}{mv^2 b^2} \tag{2.2}$$

where m is the electron mass. Total energy dE transferred to the target electrons of density n_e while the projectile moves a distance dx, is given by

$$dE \; = \; n_e dx \int_{b_{min}}^{b_{max}} T \, 2\pi b \, db \tag{2.3}$$

Here, using the cylindrical coordinates with the axis along the projectile motion, we have integrated over all possible values of impact parameter b taken between b_{min} and b_{max} that are estimated below. Substituting value of T, the electronic stopping S_e is given by

$$\begin{aligned} S_e &= \frac{dE}{dx} \\ &= \frac{4\pi Z_1^2 e^4 n_e}{mv^2}\int_{b_{min}}^{b_{max}} \frac{db}{b} \\ &= \frac{4\pi Z_1^2 e^4 n_e}{mv^2} ln(b_{max}/b_{min}) \end{aligned} \tag{2.4}$$

Since the maximum energy T_{max} that can be transferred to an electron in a collision with the projectile corresponds to electron velocity equal to $2v$, using

Eq. 2.2, we can write

$$\begin{aligned} T_{max} &= \frac{1}{2}m\,4v^2 = \frac{2Z_1^2e^4}{mv^2b_{min}^2} \\ b_{min} &= \frac{Z_1e^2}{mv^2} \end{aligned} \tag{2.5}$$

The minimum energy that can be transferred to the electrons cannot be taken to be zero because it gives a divergent contribution to the stopping power. It is taken as the mean excitation energy I instead. This gives,

$$\begin{aligned} T_{min} &= I = \frac{2Z_1^2e^4}{mv^2b_{max}^2} \\ b_{max} &= \frac{2Z_1e^2}{(2mv^2I)^{1/2}} \end{aligned} \tag{2.6}$$

Using the b_{min} and b_{max} given above, Eq. 2.4 becomes,

$$S_e = \frac{2\pi Z_1^2e^4n_e}{mv^2}ln(\frac{2mv^2}{I}) \tag{2.7}$$

Bohr formula above contains all the essential features, however, later after the invention of quantum mechanics, a more precise calculation by Bethe [55] employing quantisation rules and accounting for the uncertainty in the electron's position obtained the stopping power twice the above result:

$$S_e = \frac{4\pi Z_1^2e^4n_e}{mv^2}ln(\frac{2mv^2}{I}) \tag{2.8}$$

This result is further improved by Bethe [56, 57], Møller [58], Bloch [59, 60] and a number of other authors taking into account relativity, shell structure of atoms, and polarisation or Barkas-Anderson effect. [61–88] With these corrections, Bethe-Bloch formula becomes very accurate (within a few %) for projectile velocities higher than its atomic electron velocities. The radiative effects at still higher velocities set an upper limit to the projectile velocity for the validity of this formula. For intermediate values of target atom's atomic number Z_2, the Bethe-Bloch formula is valid for $10^{-1} \lesssim v/\sqrt{c^2 - v^2} \lesssim 10^3$ where c is the speed of light in vacuum. [89, 90] A discussion on Bethe-Bloch formula along with its various corrections is tempting but beyond our scope as we will primarily deal with the electronic stopping power of slow ions in this thesis. A description of various corrections can be found in, for example, Refs.[91, 92] and various theoretical and experimental aspects of the problem are discussed in Ref. [80].

2.2 Low velocity regime

The target electrons screen the charge of a slow projectile very efficiently. The extent of screening and hence the effective charge and size of the projectile depend on both its electronic structure and velocity as well as on the electronic structure of the target material. In the following, various theories employing different assumptions for slow projectile stopping are reviewed.

2.2.1 Binary collision theories

Firsov assumed that at low velocities ($v < v_0$) the projectile forms quasi-molecules with individual target atoms over its interaction period with them. He considered a surface between the two atoms of such a quasi-molecule where the normal component of the electric field vanishes. Flux of electrons across this surface from the target atom side to the projectile side leads to a momentum transfer to the projectile equal to $-mv$. During its passage through a material, a series of such events slow down the projectile. Using Thomas-Fermi atomic model, Firsov obtained the electronic stopping cross section ε_e ($S_e/atom$) as

$$\varepsilon_e \quad = \quad \frac{0.35(Z_1+Z_2)^{5/3}}{1+0.16(Z_1+Z_2)^{1/3}r_{min}/a_0}\frac{\hbar}{a_0}v \tag{2.9}$$

where r_{min} is the distance of closest approach between the projectile and the target atoms. We note here that the Firsov theory gives a linear dependance of stopping on the projectile velocity v.

Lindhard-Scharff model considers binary collision between the projectile ion and the target electrons. They derived an expression for the electronic stopping power, given by [93]

$$S_e = \xi_e 8\pi n_e e^2 a_0 \frac{Z_1 Z_2}{(Z_1^{2/3} + Z_2^{2/3})^{3/2}} \frac{v}{v_0} \tag{2.10}$$

where $\xi_e \approx Z_1^{1/6}$. Their derivation is not published but their basic treatment of the problem of projectile energy loss can be found in Ref.[94]. A detailed derivation, based on Thomas-Fermi model of atom, can also be found in a relatively recent article by Tilinin [95]. A common feature of the above formula with that of Firsov's is the linear dependance of electronic stopping power on projectile velocity. Experiments on several simple metals agree with such a linear behaviour of electronic stopping with projectile velocity, for example, for a H moving through Al [33].

2.2.2 Target as electron gas I

Fermi and Teller [96] derived an expression for the electronic stopping power of a slow ($v << v_F$) muon in a free electron gas with Fermi velocity v_F. They assumed that only electrons within a thickness v at the fermi surface can exchange energy with the projectile. They further assumed that collisions at a distance greater than the size of neutralised screened projectile will not contribute to the energy loss process and thus set a corresponding lower cutoff on the momentum transfer. Their result is the following.

$$S_e = \frac{2}{3\pi} \frac{m^2 e^4 v}{\hbar^3} ln \frac{v_F}{\alpha c} \tag{2.11}$$

where $\alpha = 1/137$ and c is speed of light in vacuum. Just like Firsov and Linhar-Scharff formulae, this result gives a linear velocity dependance to the electronic stopping power.

As suggested by Fermi [97], Lindhard considered the target material as a dielectric medium and calculated the electronic stopping of a non-relativistic charged projectile moving in it [98]. He assumed that the projectile is a point charge moving with a constant velocity. The electronic stopping power in this formalism is simply $Z_1 e$ times the electric field at the projectile's position. His result is:

$$S_e = -\frac{Z_1^2 e^2}{\pi v^2} Im \left\{ \int_0^\infty \frac{dk}{k} \int_{-kv}^{+kv} d\omega \frac{\omega}{\varepsilon(k,\omega)} \right\} \tag{2.12}$$

where $\varepsilon(k,\omega)$ is dielectric constant of the medium that depends on wavevector k and frequency ω. At high projectile speed where classical dielectric function can be used, above result reduces to the Bethe stopping formula [55]. At low velocities, using the Random Phase Approximation (RPA) Lindhard obtained,

$$S_e = -C(\chi) \frac{4 Z_1^2 e^4 m^2}{3\pi \hbar^3} v \tag{2.13}$$

where $C(\chi) = \int_0^1 \frac{z^3 dz}{(z^2+\chi^2 f(z))^2}$, $\chi = \sqrt{e^2/\pi\hbar v_F}$ and $f(z) = \frac{1}{2} + \frac{1-z^2}{4z} \log\left|\frac{z+1}{z-1}\right|$. A simplified result [98] is

$$\begin{aligned} S_e &= const.\left(\frac{2mv^2}{\hbar\omega_0}\right)^{3/2} \frac{4\pi Z_1^2 e^4}{mv^2} \\ &\propto v \end{aligned} \tag{2.14}$$

where $\omega_0 = (4\pi e^2 n_e/m)^{1/2}$ is classical plasma frequency of the electron gas and $const. \sim 0.05 - 0.1$.

Instead of the classical electric field, Ritchie [99] used the quantum perturbation theory to calculate the charge density in presence of the projectile. Using a different approximation for the dielectric function he obtained

$$S_e = \frac{2}{3\pi} \frac{Z_1^2 e^4 m^2}{\hbar^3} \left[ln\,(1 + \pi v_F/\alpha c) - \frac{1}{1 + \alpha c/\pi v_F} \right] v \tag{2.15}$$

This also gives a velocity proportional stopping power for a slow projectile as all previous results in this section.

2.2.3 Target as electron gas II

The problem of electron scattering off the screened potential of the projectile can be treated with Feynman-diagrams. Summing over all the terms in diagrammatic perturbation series and and accounting for the Pauli's exclusion principle only in the very last transition by restricting the final states to empty states outside the fermi surface, the electronic stopping power of a proton is calculated [100], given by

$$\begin{aligned} S_e &= n_e v_F \sigma_{tr}\, v \\ \sigma_{tr} &= \frac{4\pi}{k_F^2} \sum_{l=0}^{\infty} (l+1) sin^2(\delta_l - \delta_{l+1}) \end{aligned} \tag{2.16}$$

where σ_{tr} is transport cross-section, k_F is Fermi wavevector and δ_l is phase shift for lth partial wave for scattering of electrons at the Fermi surface. Atomic units ($\hbar = e = m = 1$) are used here. This method also gives a velocity proportional stopping power.

Ferrell and Ritchie [101] calculated the phase shifts by direct numerical integration [102] of the radial part of Schrodinger equation with a Yukawa-type screened proton potential with a screening length $\kappa = 3(\frac{4}{9\pi})^{1/3}\frac{1}{\sqrt{r_s}}$. The Friedel sum rule $\frac{2}{\pi}\sum_l (2l+1)\delta_l = 1$ [103] was satisfied to within 1.7% at electron density parameter $r_s = 2$ but deviations were found for lower electron densities (90% at $r_s = 6$). They overcome this problem by adjusting the screening length κ such that the Friedel sum rule is satisfied.

Density functional theory based non-linear calculations of electron distribution around a proton in electron gas [104, 105] showed that the results are considerably different from the linear response theory or linear screening calculations. Echenique et al. [18, 19] assumed that for a slow projectile, the charge distribution and hence the potential around it is approximately the same as if it were a fixed impurity atom. They used the density functional theory to calculate the phase shifts for the scattering of electrons at the fermi surface of an electron gas off the self-consistent screened potential of the projectile. The Friedel sum rule was satisfied to within 0.02 electrons. Their results for the electronic stopping power of slow H and He projectiles in a free electron gas are extensively used as a standard for comparison with experiments and other more advanced methods, e.g., time dependent density functional theory (TDDFT) for electron dynamics or Ehrenfest dynamics based on TDDFT that we use.

All above theories and methods for calculating stopping of a slow projectile give a velocity proportional electronic stopping. However, experiments on transition metals show a clear deviation from this behaviour [22, 106]. By setting a minimum on the energy transfer from the projectile to the electrons by limiting scattering angle or by limiting the effective electron density depending on the average energy transfer to an electron in a binary collision with the projectile the non-linear behaviour of the electronic stopping was qualitatively reproduced [17, 22, 27, 28, 30, 32, 107, 108].

2.2.4 Molecular Dynamics Methods

Electronic stopping power can be calculated using molecular dynamics methods that explicitly treat the electrons as quantum mechanical objects. Time dependent tight binding [9, 10] with empirically parametrized functions for Hamiltonian and overlap matrix elements [109, 110] is a very efficient method to simulate the dynamics of a system of ions and electrons [9, 11–16]. Ions are treated classically with forces derived from Hellmann-Feynman theorem. Electrons are represented by single-particle density matrix $\rho(t)$. Time evolution of $\rho(t)$ is determined by quantum Liouville equation

$$\iota\hbar\frac{\partial\rho(t)}{\partial t} = [h_e(\mathbf{R}(t)), \rho(t)]$$

where $h_e(\mathbf{R}(t))$ is single-electron Hamiltonian at time t when nuclear configuration is $\mathbf{R}(t) = \{\mathbf{R_1}(t), \mathbf{R_2}(t), \mathbf{R_3}(t), ...\}$ and $[.., ..]$ shows the commutation. Electronic energy $E(t)$ is given by

$$E(t) = Tr[\rho(t)h_e(\mathbf{R}(t))]$$

where $Tr[..]$ is taking the trace [13].

During the passage of a projectile through a material, its energy loss to the electrons increases the electronic energy that can be calculated using above equation [14–16]. This semi-empirical approach is very efficient and reasonably accurate for large scale simulation of the whole radiation damage event.

A more accurate method to calculate the electronic stopping power is treating the problem with time dependent density functional theory [111]. This *ab* *initio* approach has proven reasonably successful [29]. First, the single particle Kohn-Sham ground state is calculated using ground state (time independent) density functional theory. Time evolution of this state governs the dynamics of the electrons. Under the action of a time dependent potential (due to a moving projectile, for example) energy of the electronic system becomes a function of time. Using this method, Pruneda et al. [29] calculated the electronic stopping power of proton and antiproton in LiF. The target atoms, Li and F, were fixed and the projectiles were described with their screened Coulomb potential propagating at a constant speed. Despite somewhat poor representation of the projectiles, they recovered the threshold [41] and Barkas-Anderson [67, 74, 91] effects.

In this thesis, we take a step further. First, we improve the description of the projectile by considering it an atom just like all the target atoms. Second, the coupled dynamics of both the nuclei and the electrons is simulated. This so called Ehrenfest dynamics is implemented in SIESTA code [45, 46] and can also be used to study other non-adiabatic processes. We present detailed implementation of this method in chapter 3.

Chapter 3

Coupled ion-electron dynamics based on TDDFT

Siesta *implementation*

In classical molecular dynamics (MD) simulations, nuclei follow classical trajectories in a potential determined by the electronic ground state, whereas the dynamics of electrons is constrained to the ground state only. They are assumed to follow the nuclei adiabatically. That is, electrons stay in the ground state corresponding to the instantaneous configuration of the nuclei. In Ehrenfest dynamics (ED), on the contrary, we explicitly describe the dynamics of the electrons without this constraint. The effective mean field potential offered to the electrons is time dependent due to nuclear motion. It leads to transitions between various electronic states and thus a non-adiabatic energy exchange between the electronic and nuclear subsystems.

A set of initial single particle states — solutions to the Kohn Sham density functional theory equations — is evolved with time using the Hamiltonian of the electronic subsystem. The latter is calculated using the instantaneous electron density and nuclear positions. Nuclear dynamics is determined using Newton's equations of motions. The forces on the nuclei are calculated from the instantaneous electronic potential energy surface. We will describe how all this is done in the following sections.

3.1 Electron Dynamics

In this section we will describe how the dynamics of electrons is simulated using density functional theory. First, we obtain electronic ground state for the initial configuration of the nuclei. Then we evolve it with time simultaneously with nuclear motion under classical equations of motion. Time is discretised with a small time step ($\sim asec$) to do this numerically. We use atomic orbitals basis set that is attached to the nuclear positions and changes with time due to nuclear motion. We keep the electronic wavefunction in instantaneous basis by changing the basis set whenever nuclei move. Details of these steps is described below.

3.1.1 Obtaining initial state

Although, it does not have to be so, we start electron dynamics with electrons in the ground state. To obtain the ground state of electrons, we solve a set of single particle Schrodinger-like Kohn-Sham (KS) DFT equations,

$$[\frac{-\hbar^2}{2m}\nabla^2 + \mathcal{V}_{KS}(\mathbf{r})]\psi_i(\mathbf{r}) = \epsilon_i\psi_i(\mathbf{r}) \tag{3.1}$$

where ∇^2 is Laplace operator, m is the electron mass. $\{\epsilon_i\}$ and $\{\psi_i(\mathbf{r})\}$ are the single particle KS energy eigenvalues and eigenstates. $\mathcal{V}_{KS}(\mathbf{r})$ in Eq. 3.1 is given by

$$\mathcal{V}_{KS}(\mathbf{r}) = Ke^2\int d\mathbf{r}'\frac{n(\mathbf{r}')}{|\mathbf{r}-\mathbf{r}'|} - Ke^2\sum_{\alpha=1}^{N_n}\frac{Z_\alpha}{|\mathbf{r}-\mathbf{R}_\alpha|} + \frac{\delta E_{xc}}{\delta n(\mathbf{r})} \tag{3.2}$$

$$n(\mathbf{r}) = 2\sum_{i=1}^{N/2}|\psi_i(\mathbf{r})|^2 \tag{3.3}$$

where $\mathbf{R}_\alpha$ is the position of αth nucleus, K is Coulomb constant, e is the elementary charge, and Z_α is the atomic number of αth nucleus. E_{xc} is the exchange correlation energy of the electrons. Its exact functional form is not known so it is approximated either with local density approximation (LDA) or generalised gradient approximation (GGA).

Although, the KS equations 3.1 are exact in principle, their solutions and hence the corresponding electron density are only approximate not only due to the approximate nature of E_{xc} but also due to the self interaction present in the Hartree potential, the first term in Eq. 3.2. The latter usually results in an extra delocalisation of the electron cloud. Since $\mathcal{V}_{KS}(\mathbf{r})$ is a functional of electron density $n(\mathbf{r})$ that is determined by the occupied single particle states $\{\psi_i(\mathbf{r})\}$, a self-consistent solution of Eq. 3.1 is found by iteration. We assume a spin-compensated non-magnetic system here so the sum in Eq. 3.3 is over the lowest energy $N/2$ KS states where N is total number of electrons.

3.1.1.1 Energy of the electronic subsystem

The total energy of the electronic subsystem including the nuclear-nuclear interaction is given by

$$\begin{aligned} E_{KS} &= \frac{-\hbar^2}{2m}\sum_{i=1}^{N/2}\int d\mathbf{r}\psi_i^*(\mathbf{r})\nabla^2\psi_i(\mathbf{r}) + \frac{1}{2}Ke^2\int d\mathbf{r}d\mathbf{r}'\frac{n(\mathbf{r})n(\mathbf{r}')}{|\mathbf{r}-\mathbf{r}'|} - Ke^2\sum_{\alpha=1}^{N_n}\int d\mathbf{r}\frac{Z_\alpha n(\mathbf{r})}{|\mathbf{r}-\mathbf{R}_\alpha|} \\ &+ E_{xc}[n(\mathbf{r})] + Ke^2\sum_{\alpha\neq\beta=1}^{N_n}\frac{Z_\alpha Z_\beta}{|\mathbf{R}_\alpha-\mathbf{R}_\beta|} \end{aligned} \tag{3.4}$$

where the first term is kinetic energy, second term is electron-electron Coulomb interaction or Hartree energy, third term is electron-nuclear Coulomb interaction, fourth term is exchange correlation energy and the last term is nuclear-nuclear Coulomb interaction energy. Using Eq. 3.1, we can write

$$\begin{aligned} E_{KS} &= Tr[H\rho] - \frac{1}{2}Ke^2\int d\mathbf{r}d\mathbf{r}'\frac{n(\mathbf{r})n(\mathbf{r}')}{|\mathbf{r}-\mathbf{r}'|} - \int d\mathbf{r}n(\mathbf{r})\frac{\delta E_{xc}}{\delta n(\mathbf{r})} \\ &+ E_{xc}[n(\mathbf{r})] + Ke^2\sum_{\alpha\neq\beta=1}^{N_n}\frac{Z_\alpha Z_\beta}{|\mathbf{R}_\alpha-\mathbf{R}_\beta|} \end{aligned} \tag{3.5}$$

$$H = \frac{-\hbar^2}{2m}\nabla^2 + \mathcal{V}_{KS}(\mathbf{r}) \tag{3.6}$$

where ρ is the density matrix and Tr stands for taking trace. When nuclei or ions start moving, $\mathbf{R}_\alpha \to \mathbf{R}_\alpha(t)$. Hence $\mathcal{V}_{KS}(\mathbf{r}) \to \mathcal{V}_{KS}(\mathbf{r},t)$ and $H \to H(t)$. Further, due to time evolution under $H(t)$, $\psi_i(\mathbf{r}) = \psi_i(\mathbf{r}, t = 0) \to \psi_i(\mathbf{r},\mathbf{t})$ and hence $n(r) \to n(r,t)$, which in turn feeds back a time dependence to H other than the one through $\mathbf{R}_\alpha(t)$. For clarity, we omit these time dependences and always write $H[\{\mathbf{R}_\alpha(t)\}, n(r,t)]$ as $H(t)$. In the next section, we will describe how the initial electronic state, solution set of Eq. 3.1 is propagated.

3.1.2 Time evolution

Time dependent density functional theory (TDDFT) gives us time dependent version of Eq. 3.1

$$\frac{\iota}{\hbar}\frac{\partial}{\partial t}\psi_i(\mathbf{r},t) = H(t)\psi_i(\mathbf{r},t) \tag{3.7}$$

where

$$\begin{aligned}
H(t) &= \frac{-\hbar^2}{2m}\nabla^2 + \mathcal{V}_{KS}(\mathbf{r},t) && (3.8)\\
\mathcal{V}_{KS}(\mathbf{r},t) &= Ke^2 \int d\mathbf{r}' \frac{n(\mathbf{r}',t)}{|\mathbf{r}-\mathbf{r}'|} - Ke^2 \sum_{\alpha=1}^{N_n} \frac{Z_\alpha}{|\mathbf{r}-\mathbf{R}_\alpha(\mathbf{t})|} + \frac{\delta E_{xc}[n(\mathbf{r},t)]}{\delta n(\mathbf{r},t)} && (3.9)\\
n(\mathbf{r},t) &= 2\sum_{i=1}^{N/2} |\psi_i(\mathbf{r},t)|^2 && (3.10)
\end{aligned}$$

We approximate the exchange correlation energy E_{xc} using LDA or GGA with instantaneous electron density and ignore any history effects. For an initial state $\psi_i(\mathbf{r}, t = 0)$ at $t = 0$, solution of Eq. 3.7 gives us state at a later time t

$$\psi_i(\mathbf{r},t) = \exp\,[\frac{\iota t}{\hbar}H(t)]\psi_i(\mathbf{r}, t = 0) \tag{3.11}$$

In practice, the above equation is not solved at once, instead, it is evolved over infinitesimal time steps using some suitable algorithm. We use Crank-Nicholson algorithm for this purpose which preserves time reversal symmetry and is very stable for time steps as big as a few atto seconds.

3.1.2.1 Crank-Nicholson algorithm

For an infinitesimal time dt after any time t, $\psi_i(\mathbf{r}, t+dt)$ can be written in terms of $\psi_i(\mathbf{r}, t)$ as

$$\psi_i(\mathbf{r}, t+dt) \quad = \quad \exp\,[\frac{\iota dt}{\hbar}H(t)]\psi_i(\mathbf{r}, t) \tag{3.12}$$

Crank-Nicholson algorithm approximates the exponential factor as

$$\exp\,[\frac{\iota dt}{\hbar}H(t)] \quad \simeq \quad \frac{1-\iota H dt/2}{1+\iota H dt/2} \tag{3.13}$$

so we can write

$$\psi_i(\mathbf{r}, t+dt) \quad \simeq \quad \frac{1-\iota H dt/2}{1+\iota H dt/2}\psi_i(\mathbf{r}, t) \tag{3.14}$$

In practice, since we use atomic orbital basis set that is non-orthogonal, above relation is changed to

$$\begin{aligned} \psi_i(\mathbf{r}, t+dt) &\simeq \frac{1-\iota S^{-1} H dt/2}{1+\iota S^{-1} H dt/2}\psi_i(\mathbf{r}, t) && (3.15)\\ &= \frac{S-\iota H dt/2}{S+\iota H dt/2}\psi_i(\mathbf{r}, t) && (3.16)\end{aligned}$$

where S is the overlap matrix of instantaneous basis set. The last relation increases computational efficiency by saving an inversion and a multiplication.

In the following section, we will describe how $\psi_i(\mathbf{r}, t)$ is written in new basis when the latter is changed due to nuclear motion.

3.1.3 Changing atomic orbitals basis set

We use an incomplete basis set of localised atomic orbitals that are attached to the nuclear positions to best describe the electronic system. When nuclei move, the basis orbitals move with them and our basis set is changed. We need to update KS wavefunctions for this change to advance our calculations in instantaneous basis set. Since we always seek computational efficiency, a method due to Tomfohr and Sankey [112] is widely used for this purpose.

3.1.3.1 Tomfohr-Sankey method

J. K. Tomfohr and O. F. Sankey devised a method [112] to update the wavefunction for the change in the basis set. What they did is very simple. They integrated time-dependent Schrodinger (or KS) equation written in orthogonalised basis over an infinitesimal time Δt during which the basis set changes abruptly. Taking limit $\Delta t \to 0$, they found the following result.

$$
\begin{aligned}
S_f^{1/2}\mathbf{C}_f &= S_i^{1/2}\mathbf{C}_i && (3.17)\\
\mathbf{C}_f &= S_f^{-1/2}S_i^{1/2}\mathbf{C}_i && (3.18)
\end{aligned}
$$

where S_i and S_f are initial and final (old and new) overlap matrix and $\mathbf{C}_i$ and $\mathbf{C}_f$ are expansion coefficients of the wavefunction in initial and final (old and new) basis sets.

In the following section, we will describe how the nuclear dynamics is simulated.

3.2 Nuclear Dynamics

Nuclei (ions) are treated as classical particles so their dynamics is described by Newton's equations of motion. To compute the dynamics numerically, all we need is initial conditions and forces on the nuclei at every time step. We can then use some suitable algorithm to compute the nuclear trajectories in position and velocity spaces. In the following, we will describe how the forces on the nuclei are calculated. We will give a brief description of Velocity Verlet algorithm that is widely used due to its stability.

3.2.1 Forces on the nuclei

Nuclei move in a potential that is determined by the electronic state. This potential is the expectation value of the electronic Hamiltonian, i.e., the electronic energy E_{KS}:

$$
E_{KS} = \sum_{i=occ} \langle\psi_i(\mathbf{r},t)|H(t)|\psi_i(\mathbf{r},t)\rangle
$$

where the sum is over the occupied states. Considering $E_{KS} = E_{KS}[\{\mathbf{R}_\alpha(t)\}, t]$, the force on the ith nucleus F_i is expressed as

$$F_i = -\nabla_{\mathbf{R}_i} E_{KS} \tag{3.19}$$

where $\nabla_{\mathbf{R}_i}$ is gradient operator with respect to the position of ith nucleus. The forces on nuclei are calculated a step before updating their positions and velocities. How the latter task is carried out is described below.

3.2.2 Atomic positions and velocities

We start the dynamics with atoms including the projectile at desired positions and with desired velocities. As time passes, we update the atomic positions and velocities using the so called velocity Verlet algorithm as described below.

3.2.2.1 Velocity Verlet algorithm

For nuclear dynamics, we calculate velocities at current time step and positions at the next time step using forces at current and previous time steps. Suppose the quantities to compute at current time step are denoted by new and their values computed at previous time step are denoted by old in subscript. Velocity verlet algorithm then gives v_{new} and x_{new}:

$$\begin{aligned} v_{new} &= v_{old} + \frac{(F_{old} + F_{new})}{2M} dt && (3.20) \\ x_{new} &= x_{old} + v_{new} dt + \frac{1}{2} \frac{F_{new}}{M} dt^2 && (3.21) \end{aligned}$$

where M, x, and v are mass, position and velocity of a particle and F is force acting on it. This is how we update atomic or nuclear positions and velocities.

This completes our description of the Ehrenfest dynamics as implemented in the SIESTA code [44–46].

Chapter 4

Simulating the passage of ions through matter

Technical details

In this chapter, we will describe how we simulate the passage of a projectile atom through a crystalline material and how we calculate the electronic stopping power of the projectile in that material from the energy of the electronic subsystem.

4.1 A projectile moving through a solid target

We perform all calculations using the Siesta method [44, 45] with atomic orbitals basis set [113]. Since we are only interested in the very low energy regime that is far below the core electrons excitation thresholds, only the valence electrons are considered explicitly and norm-conserving pseudopotentials generated using the Troullier-Martins scheme [114] are used to describe the core electrons. We consider a $n_x \times n_y \times n_z$ supercell , i.e., a larger unit cell with dimensions determined by n_x, n_y and n_z conventional unit cells along the three cartesian axes. The projectile is placed somewhere in the desired channel and DFT ground state is found. The projectile is then given an initial velocity along the channel axis while all atoms of the target material are initially quiescent. Using a time step of

~ 1 asec or smaller, depending on the projectile velocity, the system evolves by following the Ehrenfest coupled electron-ion dynamics until the projectile travels a distance of about 10 Å along the channel axis. While the electronic subsystem evolves at every time step, the nuclei are moved only at every third step under the action of quantum mechanical forces derived from the electron density at a step earlier. Due to technical issues, at least three electronic evolution steps are needed before we move the nuclei. We keep a record of the projectile's position and the electronic energy for all time steps of the Ehrenfest dynamics. This data is used to get the electronic energy as a function of distance travelled by the projectile that is used to calculate the electronic stopping power. How the stopping power is extracted is explained in the next section.

We use the generalised gradient approximation (GGA) for the exchange-correlation energy functional in the case of gold target and the local density approximation (LDA) in the case of other targets considered including various insulators. This choice is made quite arbitrarily except in the case of LiF for which we want to make a comparison with previous LDA calculations.

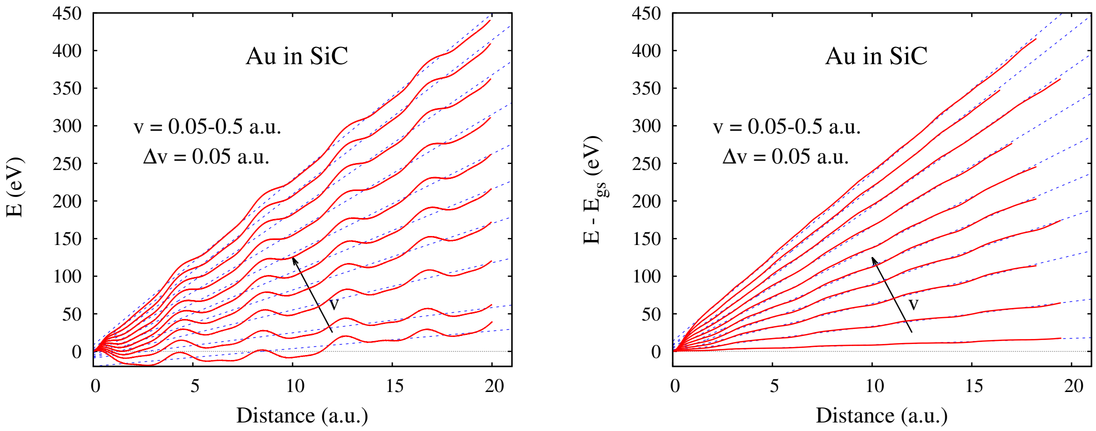

Figure 4.1: Extracting electronic stopping by fitting a line on energy E (left) and from the difference in energy and the ground state energy $E - E_{gs}$ (right). Note the difference in the slopes of the fitted lines between the two cases for $v = 0.05$ a.u..

4.2 Extracting the electronic stopping power

A projectile moving through a material excites electrons in the system to higher energy states. Electronic stopping power is the rate of change of electronic energy with respect to the distance travelled by the projectile. In our simulations, we compute the electronic energy as a function of time and projectile's position. To simulate the dynamics of a projectile moving in an infinitely extended solid, we consider the projectile in a "supercell" and use periodic boundary conditions. That is, the supercell is periodically repeated in all three spatial direction. The size of the supercell is taken large enough so that spurious effects of the repetition of the projectile are minimal.

However, due to limited computational power, the size of the supercell even along the direction of motion of the projectile cannot exceed a few lattice constants. Thus, the "energy vs distance" data that we obtain from our simulations is limited to only a few lattice constants. Obtaining an accurate value of the electronic stopping power from this data needs special care as the oscillations in the energy due to the periodicity of the target material becomes significant on the scale of total energy change.

Furthermore, at low velocities, where the nuclear stopping is sizable, the atoms in the target material are displaced from their initial positions by large distances. The corresponding change in the ground state electron energy of the system needs to be separated from the non-adiabatic change in it.

In the following, we will describe how we minimise the influence of the above factors on our electronic stopping power results. We will give some real examples as well.

4.2.1 Fitting a line on the total energy

If the electronic energy vs distance travelled by the projectile — E vs d — is linear with superimposed periodic oscillations, the electronic stopping S_e is simply the slope of the linear part. We use least square fitting to fit a line on the E vs d data and obtain the slope. This is demonstrated in the left panel of the Fig. 4.1 where we plot the E against d for a gold atom projectile in a [001] channel in SiC (red lines) for a set of projectile velocities. Electronic stopping power at a given

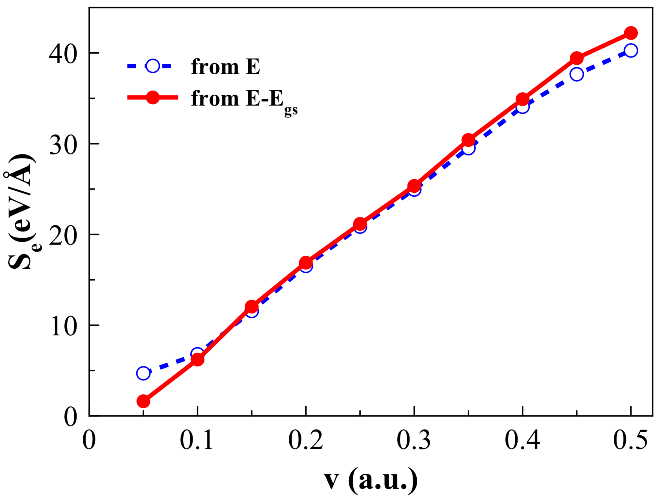

Figure 4.2: Electronic stopping power of gold in SiC calculated by fitting a line on the energy E (blue curve) and the excitation energy $E - E_{gs}$ (red curve).

velocity is the slope of the fitted line (dotted blue) for the corresponding curve. However, this method has some flaws, especially for low velocity cases where some factors other than the non-adiabatic energy transfer to the electrons also change the electronic energy significantly. How such cases are handled is discussed in the next section.

4.2.2 Fitting a line on the excitation energy

When atoms in the target material are displaced from their original positions, electronic energy of the system changes. For a violent channel that allows low impact parameter collisions between the projectile and the target atoms, or for a slow projectile that has a relatively larger interaction time, such contributions to the change in the electronic energy can be significant. As a result, E vs d loses the periodic oscillations part so we can not use fitting method described above to extract the electronic stopping power. To cure this problem, we calculate the ground state electron energy E_{gs} for the same atomic configurations as followed by the atoms under Ehrenfest dynamics (ED). For this purpose, we save the positions of all atoms at each time step during ED. Once we have these atomic trajectories, we calculate the ground state energy for a selected set of configurations from these

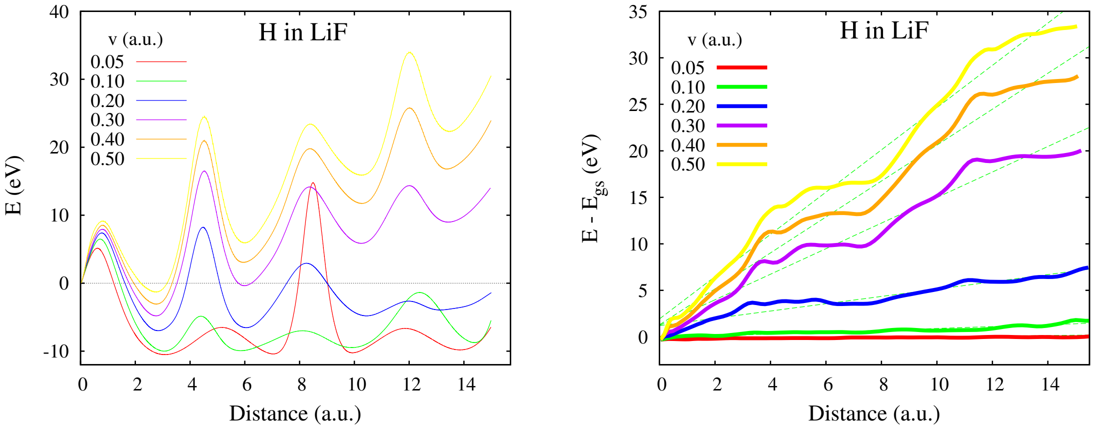

Figure 4.3: Left: Electronic energy E as a function of the distance travelled by a H projectile moving in LiF. Fitting a line on these curves does not give accurate stopping power. Right: The difference $E - E_{gs}$ is used to evaluate the stopping power.

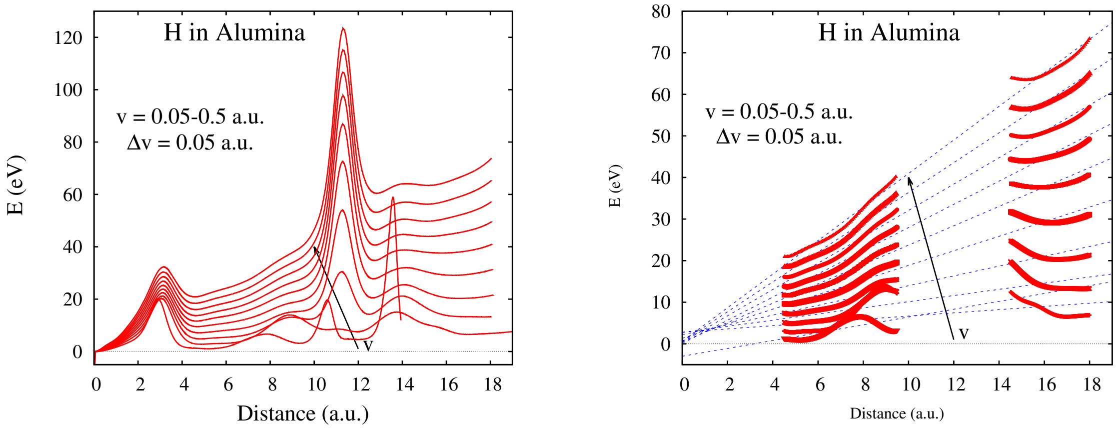

Figure 4.4: Left: Electronic energy E as a function of distance travelled by a H projectile moving in Al_2O_3. Fitting a line on these curves does not give accurate stopping power. The peaks in the E cause problem in the fitting lines on the data as they change the slopes of the lines from the average slopes of the full energy curves. Right: The peaks are removed to get average slopes of the curves.

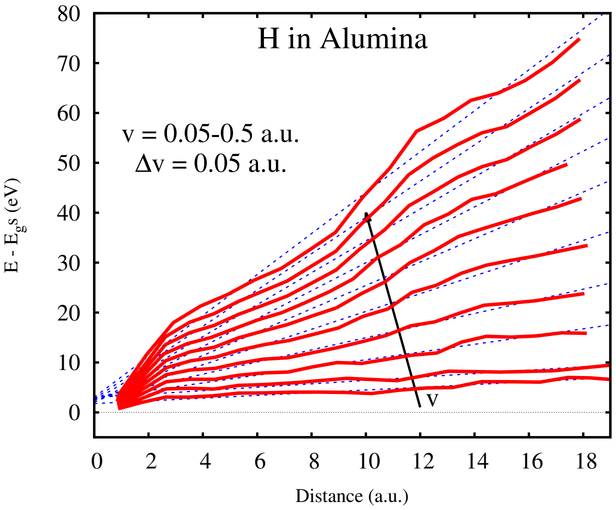

Figure 4.5: Electronic excitation energy $E - E_{gs}$ as a function of distance travelled by a H projectile moving in Al_2O_3. The peaks in the energy E in the left panel of Fig. 4.4 are due to the changes in the ground state energy E_{gs} and not in the excitation energy $E - E_{gs}$. This is the reason that clipping these peaks gives quite accurate electronic stopping power as shown in Fig. 4.6.

saved ones with a given interval of the ED time steps. For practical purposes, only a few points per $\mathring{A}$ travelled by the projectile suffice. Then the ground state energy E_{gs} is subtracted from the corresponding ED electron energy E. The stopping power is obtained by fitting a line to the difference $E - E_{gs}$. The right panel of Fig. 4.1 demonstrates this. As can be seen in Fig. 4.1, the slopes of the fitted lines for $v = 0.05$ a.u. obtained by the two methods described above are different. Fig. 4.2 shows the electronic stopping power calculated by the two methods described above. We consider the latter method more reliable. A more complicated situation is shown in Fig. 4.3, where due to violent collisions between the projectile and the target material atoms, the E vs d data alone cannot be used to obtain the stopping power and we have to employ the second method. The importance and power of this method is evident from this example case.

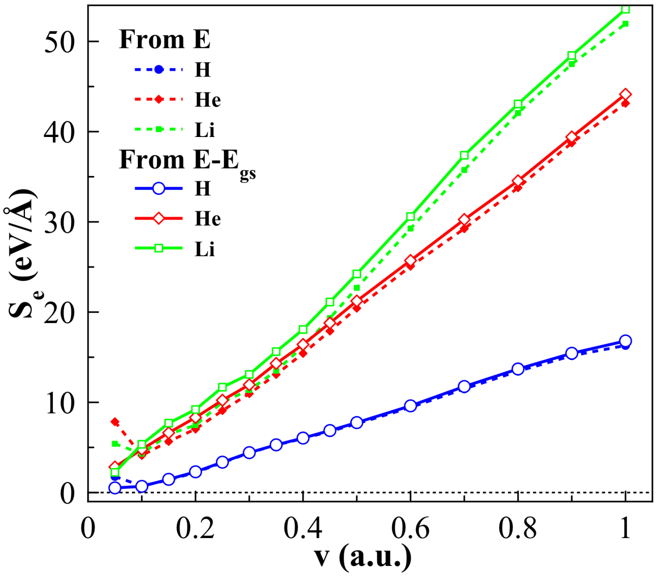

Figure 4.6: Electronic stopping power calculated by fitting a line on the energy $E(d)$ after removing the problematic peaks (dotted lines with filled symbols) and on the excitation energy $E - E_{gs}$ (solid lines with empty symbols). Although, the first method does not work at low velocities, it agrees reasonably well with the more accurate second method at higher velocities.

4.2.3 Clipping large peaks in the energy

When the energy has large peaks that change the slope of the fitted line from the average slope of the energy curves, we cannot find the stopping by fitting a line on the full data. Instead, trimming off the peaks removes their influence on the filling process and we obtain reasonably good agreement with the fitting on the excitation energy $E - E_{gs}$, except at very low velocities. This is demonstrated in Fig. 4.4. The reason that removing the peaks works is that these peaks are due to the changes in the ground state energy E_{gs} and not in the excitation energy $E - E_{gs}$ as shown in Fig. 4.5. In Fig. 4.6, we present the results obtained using these two methods for H, He and Li in alumina. At $v = 0.05$ a.u., fitting on $E - E_{gs}$ needs to be done to get accurate value of the stopping power. At higher velocities, simply clipping the "bad" peaks works well. However, we have not used this method for any projectile-target system studied in this thesis.

4.3 Summary

In this chapter, we describe the technical details of simulating the passage of a projectile atom through a crystalline material. We also describe how we extract the electronic stopping power from the energy vs distance data. Three methods are described and their results are compared for demonstration purpose.

Chapter 5

Electronic stopping power of H and He in gold

The role of d electrons and the H/He anomaly

5.1 Introduction

Recently, the electronic stopping power for swift ions in gold has been carefully characterized by experiments [20, 21, 32, 106, 107]. The experimental results show flagrant discrepancies with the established paradigm for such problems [18, 25]. Theoretical calculations based on time-dependent tight-binding [13], and detailed studies for protons based on first principles [30], only qualitatively agree with the experiments. This leaves us with very fundamental questions unanswered in spite of the apparent simplicity of the system. Most notably the H/He anomaly: the present understanding predicts a stopping power for H higher than for He at low velocities [25], which strongly contradicts the recent experiments [21].

Based on the jellium model (homogeneous electron gas) the electronic stopping power, S_e, is predicted to be $S_e \propto v$ for a slow projectile traversing a metallic medium [115, 116]. Such behaviour has been observed experimentally in many *sp*-bonded metals [22, 23], and the jellium model has allowed deep understanding of the dynamic screening of the projectile and its relation to stopping [24]. Even the jellium prediction of an oscillation of the proportionality coefficient with the projectile's atomic number Z has been verified [25] and reproduced by ab initio atomistic simulations [26]. However, phenomena that cannot be accounted for within the jellium paradigm have been described only qualitatively so far [17, 27–29]. Experiments on noble metals Cu, Ag and Au, show pronounced nonlinearities in $S_e(v)$ [20–22, 27, 30–32, 106, 107, 117]. In the case of slow H and He ions in gold [20, 21, 32, 106, 107], $S_e(v)$ displays an increase in the slope roughly around $v \backsimeq 0.18$ a.u. This is usually attributed to a threshold projectile velocity needed to excite the d-band electrons that are relatively tightly bound. A model was developed based on the ab initio density of electronic states and a stochastic treatment of excitations [17], which reproduces the threshold for protons.

Here we obtain the non-linear $S_e(v)$ and the H/He anomaly with our ab initio method described in chapter 3. We find very good quantitative agreement with some recent low energy ion scattering experiments on thin gold films [20, 21, 32, 107]. The results are analyzed in terms of the electronic excitations that are responsible for the energy loss, which very clearly shows why the slope of S_e increases with projectile velocity. In contrast to the usual idea that at low projectile velocity only electrons close to the Fermi energy contribute to the stopping, we find that there is a significant contribution from deep lying states even for a slow projectile. This means that at low velocities ($v < 0.2$ a.u.) the electrons accessible to excitations (s) are different from the ones involved in the screening of the projectile ($s + d$), the latter providing the excitation *mechanism*.

In the following sections, we give the computational details and present our results.

5.2 Computational Details

We used the Perdew-Burke-Ernzerhof (PBE) version [118] of the Generalised Gradient Approximation (GGA) to the instantaneous exchange and correlation functional. Only valence electrons in Au are considered explicitly and a norm-conserving pseudopotential is used to describe the core electrons (up to the $5p$ sub-shell). A double-zeta polarised split-valence basis was used for the valence electrons both for the projectile and the gold atoms. The grid cutoff for real

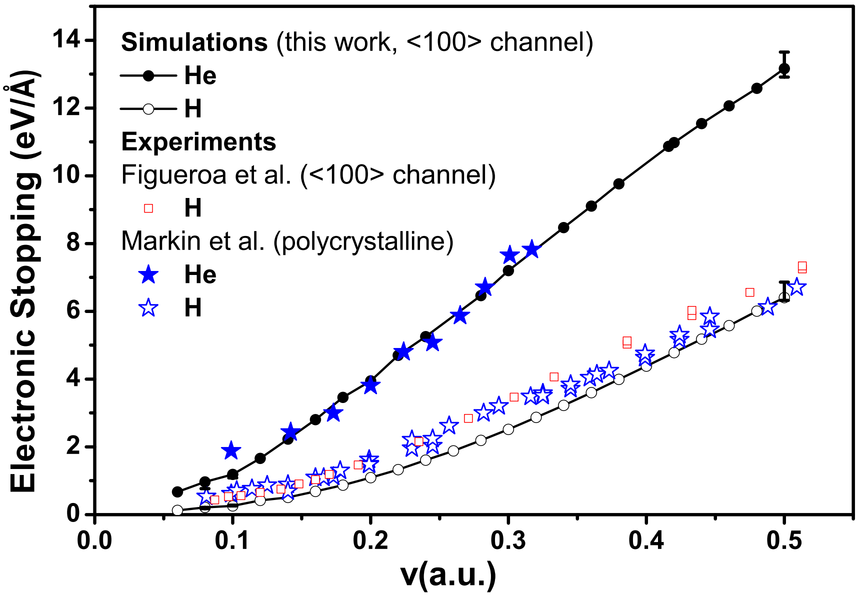

Figure 5.1: Electronic stopping power of H and He projectiles in gold as a function of projectile velocity. Results of our simulations are compared with the experimental data from Refs. [20, 21, 32, 107] on single and polycrystalline thin gold films.

space integration was 200 Ry [45]. Gold has a face centred cubic lattice with a single atom motif. The lattice parameter obtained for bulk gold was $a = 4.12$ Å, which is slightly larger than the experimental value of 4.08 Å as expected for GGA. After convergence tests, a $2 \times 2 \times 4$ supercell consisting of 64 gold atoms was selected. For integration in the Brillouin zone, 8 k-points were used with a $2 \times 2 \times 2$ Monkhorst-Pack [119] grid equivalent to a k-grid cutoff [45] of 8.256 Å.

The projectile (H or He) was initially placed at $(\frac{3}{4}a, \frac{3}{4}a, a)$ in the supercell and set in motion along $\langle 100 \rangle$ channel with a given initial velocity along the z-direction while all gold atoms are initially quiescent. We used a time step of 1 asec for the time evolution of the electronic wavefunctions. The nuclei were moved only at every third step. On the time scale of the simulation ($\sim 0.75 - 6.0$ fs for $v = 0.05 - 0.50$ a.u.), the gold nuclei only gained negligible velocities and did not move significantly. Electronic stopping power is extracted as the average slope of the electronic energy vs distance curve as described in section 4.2.1.

5.3 Results and Discussion

Fig. 5.1 shows our results for $S_e(v)$ for H and He projectiles in gold for the velocity range $v = 0.06 - 0.50$ a.u. We also plot results of some recent experiments performed on thin single crystal gold films oriented along $\langle 100 \rangle$ [32, 107] and polycrystalline gold films [20, 21]. The agreement between our simulations and the experiments is noticeable. Although the stopping power is still underestimated (especially for H around $v = 0.3$ a.u.), no previous ab initio approach had this level of agreement on the non-linear velocity dependence of the stopping power of real materials. Our results for the stopping power are well converged with respect to the basis size and the density of points on the real and the momentum space grids. A larger basis set for the projectile, however, (TZDP instead of DZP) increases the stopping power about 5% at $v = 0.5$ a.u., but considerably less at low velocity. The error bars in Fig. 5.1 indicate the dispersion in our results for v =0.08, 0.1 and 0.5 a.u. when the various parameters are varied, including the basis set (the bars for low velocities are hardly larger than the size of the circles). Details of all these convergence tests is included in Appendix A. The strict channelling in the simulation is partly behind the observed underestimation: calculations for a 30% smaller impact parameter give a 25% increase in S_e^{H} at $v = 0.28$ a.u. that reduces to 1% at $v = 0.5$ a.u.

We see a clear deviation from the linear behaviour around $v = 0.2$ a.u. in S_e of both H and He. This is unlike the $S_e \propto v$ of the uniform electron gas. It seems a plausible explanation that at low projectile velocity only s-band electrons from the states around the Fermi energy contribute to the stopping and at higher velocity electrons in the d band that lie relatively deeper in energy are also able to take part in it, resulting in an increase in the slope of S_e. Thus, comparisons have been made [21, 32, 107] with jellium using the average electron density n_e of the s electrons ($r_s = 3.01$ a.u., where $n_e^{-1} = \frac{4}{3}\pi r_s^3$), using $r_s = 1.49$ a.u., corresponding to an effective number of s and d electrons [21], or of the density in the $\langle 100 \rangle$ channel ($r_s = 1.8$ a.u.). However, the jellium predictions do not agree with the experimental results except at projectile velocities around $v = 0.6$ a.u. in the latter case, despite the expectation that all the d-band electrons are active for a projectile velocity $v \geq 0.47$ a.u. [27]. There is a further problem in

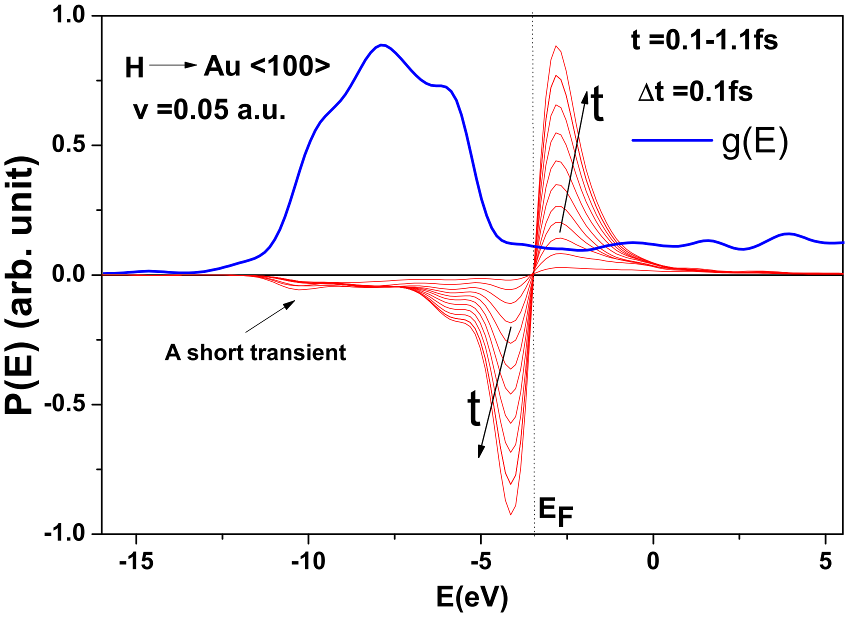

Figure 5.2: Excitation distribution $P(E)$ when H passes through gold with velocity 0.05 a.u., for time values between $t = 0.1$ fs and 1.1 fs in steps of $\Delta t = 0.1$ fs (light color; larger amplitude for longer t; Gaussian broadening $\sigma = 0.2$ eV). The dark curve is the electronic density of states $g(E)$ ($\sigma = 0.5$ eV). $P(E)$ and $g(E)$ are in different scales.

the comparison with jellium: If we assume that at low velocity only s electrons are actively participating in the stopping mechanism, the jellium model predicts $S_e^{\mathrm{H}} > S_e^{\mathrm{He}}$ [18], which is not the case.

To explain the above inconsistencies and get a better idea of the energy loss mechanism we compute the changes in the electronic distribution due to the excitation of the electrons when a projectile propagates through the material. Having $\{|\psi_n(t)\rangle\}$ and $\mathbf{X}(t)$, the set of evolved occupied KS states, and the corresponding atomic positions at time t, we calculate the adiabatic states $\{|\phi_i, \mathbf{X}\rangle\}$, i.e., the set of self-consistent static KS states for $\mathbf{X}(t)$. By projecting the evolved states onto the adiabatic states, $C_{in} = \langle\phi_i, \mathbf{X}(t)|\psi_n(t)\rangle$, the density of occupied energy states $O(E)$ at time t as a function of energy E are obtained as $O(E) = \sum_{i,n} |C_{in}|^2 \delta(E - E_i)$. Here E_i is the eigenvalue of the adiabatic state $|\phi_i, \mathbf{X}\rangle$. To compute the change in the electronic distribution or the (electron-

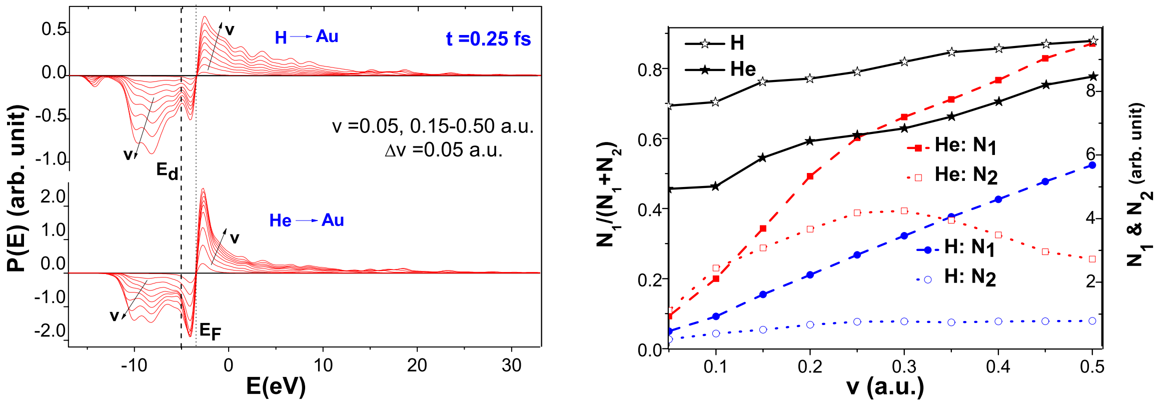

Figure 5.3: Left: Excitation distribution $P(E)$ due to the passage of a H (top) or He projectile (bottom) in gold evaluated at $t = 0.25$ fs for various projectile velocities, $v = 0.05 - 0.50$ a.u. in steps of 0.05 a.u. Increased projectile velocity gives curve with larger amplitude (indicated by arrows). The dashed and dotted vertical lines show the upper edge of the gold's $5d$-band E_d and the Fermi energy E_F. Right: Number of empty states below and above E_d, N_1 and N_2, and fraction $N_1/(N_1 + N_2)$ versus projectile velocity, due to the excitations for H or He.

hole) excitation distribution, $P(E)$, we subtract the ground state electronic distribution from $O(E)$. That is, $P(E) = O(E) - \Theta(E_F - E)g(E)$, where E_F is the Fermi energy of the system, $g(E)$ is the electronic density of states and $\Theta(E)$ is the Heaviside step function.

Fig. 5.2 shows the excitation distribution $P(E)$ as a function of energy at various instants from $t = 0.1$ fs to $t = 1.1$ fs with an interval $\Delta t = 0.1$ fs, for the passage of a H atom in gold along $\langle 100 \rangle$ with velocity $v = 0.05$ a.u. The electronic density of states of the bulk Au host $g(E)$ is also plotted in Fig. 5.2. The negative and the positive values of $P(E)$ show the density of empty and filled states below and above E_F, respectively, due to the electronic excitations caused by the moving projectile. Notice that despite being very slow ($v = 0.05$ a.u), the projectile is able to excite relatively tightly bound d-band electrons. A short initial transient behaviour is noticeable in Fig. 5.2: at energies deep below the Fermi energy, the number of empty states becomes larger initially, requiring a short time to adjust to a stationary regime. This is because in our simulations the projectile is a static impurity atom at $t = 0$ that suddenly acquires a finite velocity resulting in a large initial perturbation.

To see how the excitation distribution after the transient depends on the velocity of the projectile, we plot $P(E)$ against E in Fig. 5.3 at $t = 0.25$ fs for various projectile velocities, between 0.05 a.u. and 0.50 a.u. We see that, compared to the states just below the Fermi energy, the number of excitations from deep inside the d-band increases more quickly with the velocity of the projectile. This means that the effective number of d-band electrons involved directly in excitations provoking the stopping process increases with the projectile velocity. To see this more clearly, we separated the energy window into two parts at the upper edge of the d-band at energy E_d and calculated the total number of excitations N_1 and N_2 from the states below and above E_d for a constant distance travelled by the projectile. We find that $P(E) \propto t$ after the initial transient so we can estimate N_1 and N_2 as $N_1 = \frac{1}{v}\int_{-\infty}^{E_d} |P(E)|dE$ and $N_2 = \frac{1}{v}\int_{E_d}^{E_F} |P(E)|dE$, which we did using $P(E)$ at $t = 0.25$ fs. In the right panel of Fig. 5.3 we plot N_1 and N_2 and the fraction $N_1/(N_1 + N_2) = N_1/N$ against the projectile velocity as dashed, dotted and solid lines for H and He projectiles. We see that N_1 and N_1/N increase with v for both projectiles. For H, N_2 increases and saturates whereas for He it increases up to $v = 0.3$ a.u. but decreases for a faster projectile. Since there is one s electron and ten d electrons and N_1 also includes the contribution from the s-band states, ideally it should tend to $N_1/N \sim 10/11 = 0.909$ for high projectile velocity. N_1/N reaches only 0.88 and 0.78 for H and He at $v = 0.5$ a.u. Although the fraction of excitations from the deep lying states is higher for H, the absolute number is lower, as can be seen in the figure. Furthermore, in the case of H, $N_1 > N_2$ for the whole velocity range shown whereas for He, $N_2 > N_1$ in the very low velocity range.

We address now the low-velocity H/He anomaly. Fig. 5.4 presents the ratio $R = S_e^{\mathrm{He}}/S_e^{\mathrm{H}}$ in jellium [18]. The values of R for Au for $v = 0.1$ and $v = 0.5$ a.u. are plotted on the two dotted vertical lines at $r_s = 3.04$ and $r_s = 1.49$ a.u., which correspond to 1 and 8.24 electrons per bulk unit cell, i.e., the s electrons and the effective number of valence electrons (s and d) that fit the plasmon pole for bulk Au [21]. We see that for the faster projectile R is close to the jellium value and significantly larger than 1. However, for the slower one, we obtain $R = 4.7$, in clear disagreement with the jellium value of 0.79, but in agreement

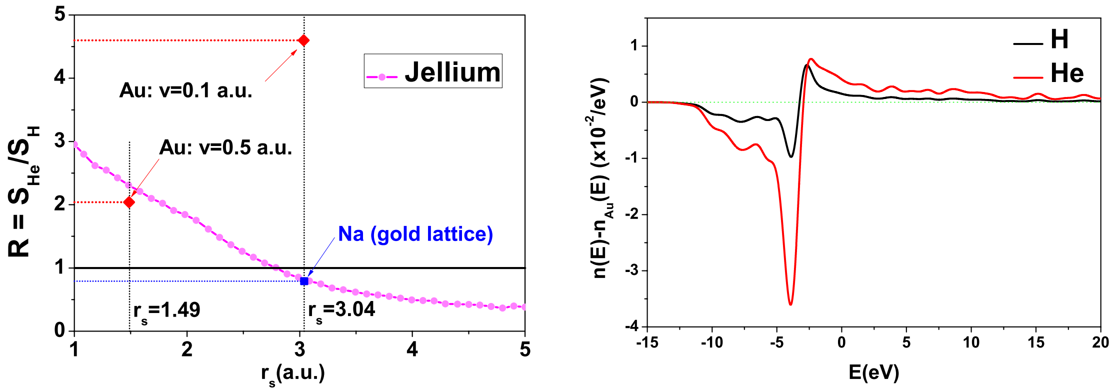

Figure 5.4: Left: The curve shows $R = S_e^{\mathrm{He}}/S_e^{\mathrm{H}}$ for jellium versus the electron density parameter r_s [18]. The values of R obtained for Au for $v = 0.1$ and 0.5 a.u. are associated with $r_s = 3.04$ and 1.49 a.u, respectively, following Ref. [21]. The calculated ratio R for a system made of Na atoms in bulk Au positions, $r_s = 3.04$, is also presented. Right: Projection of KS states for the system with projectile onto the KS states of bulk Au, for H and He, subtracting the Au density of states.

with experiment. We also plot R for the fictitious system built by putting Na atoms in the Au positions, which corresponds to an electron gas with $r_s = 3.04$. The plot shows a perfect agreement for the R values of Na and jellium [1]. These differences between jellium (or Na) and gold are thus due to the presence of gold's d electrons. This is consistent with the fact that, even if a slow projectile were unable to excite the d-band electrons appreciably, the presence of the projectile in gold constitutes a large static perturbation for the d electrons. This can be clearly seen by calculating the projection of the ground state of the gold with the projectile onto that without it and obtaining a distribution analogous to $P(E)$, now describing the static screening of the projectile. i.e., projecting the wave-functions of Au with the projectile onto the states of pure Au (Fig. 5.4). This means that for a slow projectile the response of the electrons in gold is far from the one described by the homogeneous electron gas model that includes just the

---

[1] The stopping power values for H and He in this Na are 3.902 eV/Å and 3.083 eV/Å, respectively, for $v = 0.5$ a.u., and 1.024 eV/Å and 0.715 eV/Å, for $v = 0.1$ a.u.; the corresponding values for jellium as extracted from Ref. [18] are 7.741 eV/Å and 17.874 eV/Å, respectively, for $v = 0.5$ a.u., and $r_s = 1.49$ Bohr; and 0.861 eV/Å and 0.710 eV/Å, for $v = 0.1$ a.u. and $r_s = 3.04$ Bohr.

s-band electrons.

5.4 Summary

To summarize, we have shown that realistic non-adiabatic stopping of projectiles in real metals can now be described from first-principles with acceptable accuracy, even at the Ehrenfest dynamics level. We used it to calculate the electronic energy loss on passage of H and He through Au and find good quantitative agreement with experiments. Many other problems involving non-adiabatic processes coupling many adiabatic energy surfaces can now be addressed with this technique.

Chapter 6

Electronic stopping power of H and He in Al

6.1 Introduction

Recent experiments on nanometer thick polycrystalline Al films show that while the jellium model for Al ($S_e \propto v$) works well for hydrogen (H^+ , D^+), the electronic stopping of He^+ ions in Al deviates from linearity.[33] The reason behind this was proposed to be the charge exchange processes due to the repeated shifting of $1s$ level of He up and down along the trajectory.[33] We demonstrated a successful application of coupled ion-electron dynamics using TDDFT to the electronic stopping power problem of low-velocity H and He projectiles in gold [47] in chapter 5 and of high-velocity H in aluminium [120, 121]. Using the same method we calculate here the electronic stopping power of low-velocity H and He in Al to see whether we can reproduce the experimental results.

6.2 Computational Details

The local density approximation (LDA) for the instantaneous exchange and correlation energy functional in the Ceperley-Alder [122] form parametrized by Perdew and Zunger [123] was employed. We considered two cases.

(**i**) electrons in up to $2p$ sub-shell of Al are described by norm-conserving

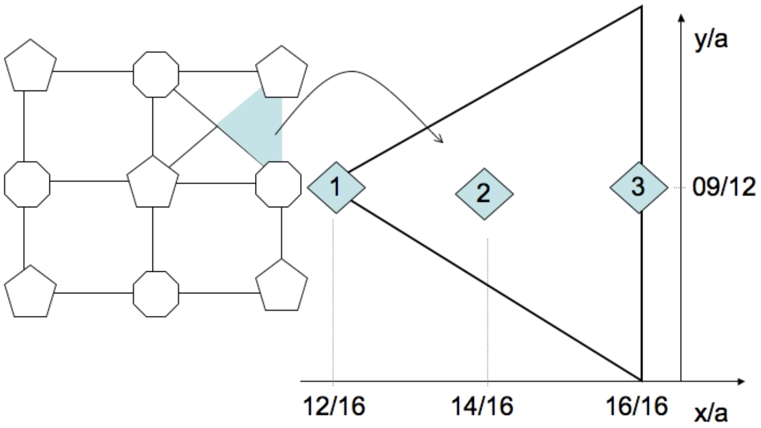

Figure 6.1: Position of [001] channels 1,2 and 3 in the xy-plane in the unit cell of Al crystal. Two {001} atomic planes spaced $a/2$ are shown with two different symbols.

pseudopotentials. We use a double-ζ polarised split-valence basis for the valence electrons of the host Al atoms as well as for the projectiles (H and He). The grid cutoff for real space integration is 200 Ry [44, 45]. The lattice parameters obtained from the relaxation of the bulk Al is 3.995 Å that is slightly smaller than the experimental value of 4.0495 Å as expected for LDA. We used $(2 \times 2 \times 4)$ supercell that is large enough to beat the spurious effects of the repetition. The Brillouin Zone integrations were performed with 9 k-points using a $3 \times 3 \times 3$ grid displaced by $(\pi/a, \pi/a, \pi/a)$, that is equivalent to a k-grid cutoff [45] of $\simeq 12$ Å.

(**ii**) Only 1s electrons of Al are described by a norm-conserving pseudopotential. All other electrons of Al atoms are considered explicitly. We use single-ζ for 2s and 2p, and a double-ζ polarised split-valence basis for the other valence electrons of Al atoms. To account for a more rapid variation of inner-shell wavefunctions of Al and resulting electron density and potentials in real space, we doubled the density of real space grid sampling points by increasing the grid cutoff four times to 800 Ry. The Brillouin Zone integrations were performed in this case with 8 k-points using a $2 \times 2 \times 2$ grid.

We considered three [001] channels at $y/a = 9/12$ and, $x/a = 12/16, 14/16$ and $16/16$. These are labelled as channel 1, 2 and 3 respectively, as shown in

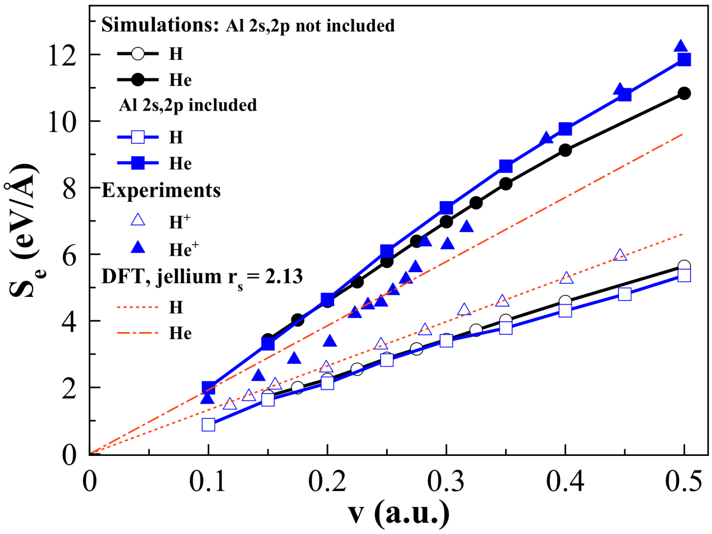

Figure 6.2: Electronic stopping power of H (open symbols) and He (filled symbols) in Al. Comparing the simulations with the experimental results from Ref. [33]. The two thin straight lines are the DFT results for H and He in jellium with $r_s = 2.13$ (dotted and dash-dotted lines, respectively).

Fig. 6.1. The projectile is placed at $z = a$ and given an initial velocity along the z-direction. Using a time step of 1 asec, the system evolves by following Ehrenfest coupled electron-ion dynamics. This is continued until the projectile travels a distance of $2a$ along the z-direction. Once the transient due to the sudden start of the projectile motion has disappeared [29], S_e is extracted as the average rate of change of the electronic energy with the distance travelled by the projectile as described in section 4.2.1.

6.3 Results and Discussion

Fig. 6.2 shows our results for the electronic stopping power of H and He in Al channel 1 for both cases **i** (black lines with circles) and **ii** (blue lines with squares), that is, for two different types of Al pseudoatoms. Experimental [33] and DFT results[18] for a jellium of electron density $r_s = 2.13$ that is adequate for Al [124], are also presented for comparison. We see that our results agree fairly with the experiments. For H, our simulations underestimate the electronic stopping by

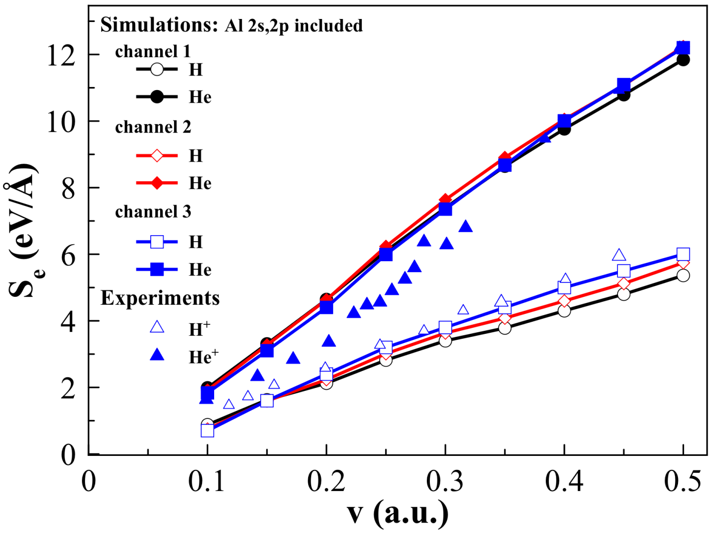

Figure 6.3: Electronic stopping power of H (open symbols) and He (filled symbols) in Al in three channels 1,2 and 3 shown in Fig. 6.1. Comparison is made with the experimental results from Ref. [33].

$\sim$ 15%, while for He our calculations underestimate it for $v \geq 0.35$ a.u. (up to $\sim$ 10%) for case **i** and overestimate it for $v \leq 0.25$ a.u. (up to$\sim$ 40%) for both Al pseudopotentials. With explicit inclusion of Al 2s and 2p electrons in calculations, the agreement of He stopping with the experiments for $v \geq 0.35$ a.u. becomes excellent. The change in the stopping power at lower velocities is small, which makes sense as a slow projectile is less likely to excite inner-shell Al electrons. In case of H, including inner-shell electrons of Al explicitly slightly decreases the electronic stopping at $v \geq 0.30$ a.u., whereas both pseudopotentials give identical stopping at lower velocities. This is interesting as including the inner-shell Al electrons is expected to do exactly the opposite.

As can be seen in Fig. 6.2, our results show that the stopping power is almost proportional to the velocity in the velocity range shown. There is, however, a slight decrease in the slope around $v = 0.4$ a.u. for both H and He projectiles. The jellium results shown in Fig. 6.2 perfectly agree with the experimental results for H in Al but for He they overestimate the electronic stopping in the jellium at low velocity and underestimate it at higher velocity. As Fig. 6.2 shows, compared to the jellium, our results for He are in much better agreement at higher velocities even without $2s, 2p$ Al's electrons.

Fig. 6.3 shows the stopping power of H and He in three different channels 1,2 and 3 shown in Fig. 6.1. Let's take H case first. As can be seen, the stopping power increases for channels 1 through 3 for $v \geq 0.4$ a.u. while a tiny decrease can be seen for lower velocities. As Fig. 6.1 shows, the projectile approaches the host Al atoms closer and closer as we move from channel 1 to 3. The stopping increases accordingly and for channel 3 we get almost a perfect agreement with the experiments. However, in an experiment, there is a distribution of positions relative to channel 1 with a range of impact parameter. But, at the moment, we do not have a method to find the weights i.e., the contributions of different channels to the stopping. All we can guess is that the projectile will tend to follow a low stopping path. For He, all the three channels considered produce almost the same stopping. However, as for H, the agreement with the experiments is improved as we move from channel 1 to 3.

The change of the slope observed in the experiments for He remains thus unclear. The authors of the experimental paper, however, point to charge effects on the projectile. They have not been contemplated here inasmuch the calculations always start with the adiabatic solution of the projectile in the solid, which unavoidably leads to a fully occupied $1s$ level. If a cationic projectile is used, there will be a time needed for that level to be filled, and there will also be a velocity dependence to this. An exploration of this effect would be thus timely. We leave it to the future work.

6.4 Summary

Theoretical simulations from first principles for the low-velocity electronic stopping power of light projectiles in Al have been presented. A good agreement with the experiments is obtained, although some key features have not been adequately reproduced. The observed change in the slope of the stopping power versus velocity curve escapes the simulations. Considering channels with smaller impact parameters improves the stopping. A proper consideration of possibly long transients related to charge could be revealing.

Chapter 7

Electronic stopping power of H and He in Na

7.1 Introduction

Energy loss of charged particles passing through a gas of free electrons has been a subject of extensive study using a variety of methods [125–131]. For H and He projectiles, theoretical calculations [18] based on phase shifts for electron scattering off the screened potential of the projectile obtained using DFT predict a crossover between two regimes with electron density: for low electron density with density parameter $r_s < 2.77$, electronic stopping power of H is higher than He, while for higher electron densities, the converse is true. In chapter 6, we calculated electronic stopping power of H and He in aluminium that is a free electron metal with $r_s = 2.07$ and lies in the higher density regime. In accordance with the DFT prediction, in Al indeed the stopping of He is larger than that of H. In this chapter, we consider sodium that is perhaps the best example of a free electron gas [132–135]. The valence electron density in sodium is low ($r_s = 3.86$) and according to the DFT results [18], the electronic stopping power of H in Na should be larger than that of He. Our calculations not only confirm this, we find a quantitative agreement with this free electron model for the electronic stopping power of H and He projectiles at low velocities. To see the effect of surfaces, we also perform calculations on a few-unit-cell-thick film of sodium. We find that the energy loss to the electrons in top few atomic layers at the surface is different than the bulk crystal.

7.2 Computational Details

The exchange and correlation energy functional is computed with the local density approximation (LDA) in the Ceperley-Alder [122] form parametrized by Perdew and Zunger [123]. Na pseudoatoms that we considered contain only the 3s valence electrons with the rest electrons in the inner atomic orbitals described by norm-conserving pseudopotentials. A double-ζ doubly polarised split-valence basis is used for all atoms. The grid cutoff for real space integration is 200 Ry [44, 45]. Sodium has a body centred cubic lattice with single atom motif. The lattice parameter we obtained by relaxing the structure is $a = 4.1486$ Å . This is slightly smaller than the experimental value of 4.23 Å as expected for an LDA functional. We used a $2 \times 2 \times 8$ supercell containing 64 Na atoms with a $3 \times 3 \times 1$ Monkhorst-Pack grid for the Brillouin zone integrations. This is equivalent to a k-grid cutoff [45] of $\simeq 12.45$ Å. We consider two cases, with the target sodium in the bulk or a film form.

(**i**) **The bulk case:** We considered a [001] channel at $(x/a, y/a) = (3/4, 3/4)$. The projectile was placed in the channel and, using a time step of an asec, allowed to move a distance of 30 a.u. along the z-direction with a given initial velocity.

(**ii**) **The film case:** We considered an 8 unit cell ($\sim$ 62.7 a.u.) thick film with a vacuum layer 28.26 a.u. wide. The film has the same structural parameters as the bulk Na, i.e., its structure is not relaxed. The lateral dimensions of the supercell we used are again 2×2. Relaxing the structure with the same supercell size decreases the interlayer distance close to the surfaces but does not change the position in the xy-plane significantly. The projectile starts moving towards the film from a distance of 11 a.u. away from the film surface and aims for the same [001] channel that is at $(x/a, y/a) = (3/4, 3/4)$. The dynamics is studied until the projectile penetrates the film around 20 a.u. deep.

Electronic stopping power is computed in both cases as the slope of a straight line fitted on the electronic excitation energy vs distance curve as described in section 4.2.2.

7.3 Results and Discussion

7.3.1 Na vs jellium

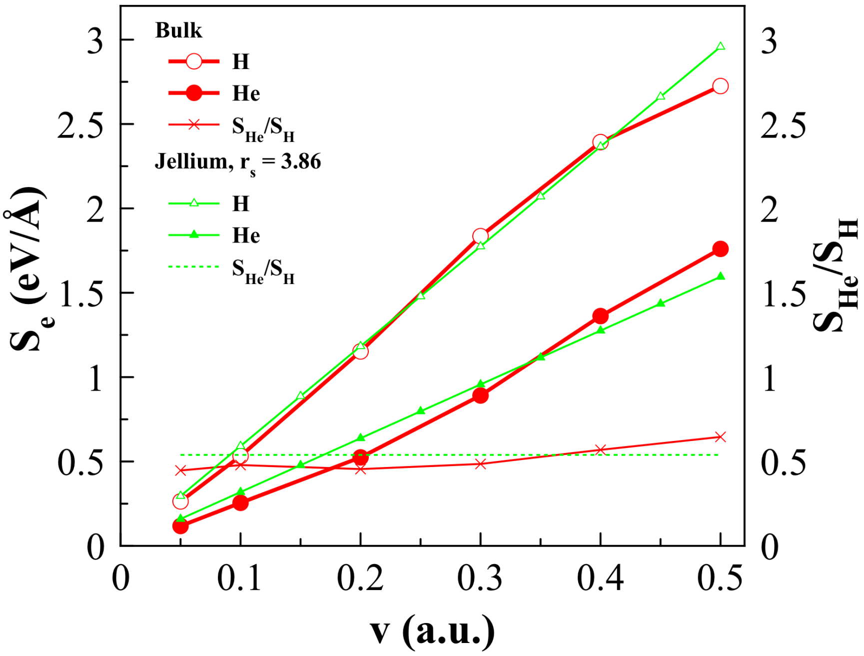

Figure 7.1: Electronic stopping power of slow H and He in the bulk Na and jellium with $r_s = 3.86$ that corresponds to average density of valence electrons in Na.

Fig. 7.1 shows the electronic stopping power of H and He, S_H and S_{He}, in the bulk Na. The stopping power of the same two projectiles in jellium with electron density parameter $r_s = 3.86$, that is appropriate for Na, are also plotted for comparison. First, note the agreement between the jellium and Na. There are only slight differences between the stopping in the two media. This is not surprising as the valence electrons in Na are only weakly bound and behave quite like jellium. At higher velocities, however, differences become more pronounced. At $v = 0.5$ a.u., for example, compared to the stopping in the jellium, H stopping power in the bulk Na is 7.8% lower while He stopping power is 10.3% higher.

As we expect for a free electron metal, there seems no threshold effect for Na. $S_e(v)$ in Na is linear with approximately the same slope as in jellium, except at

$v > 0.3$ a.u. where the slope for the H stopping slightly increases while that for He stopping slightly decreases. The ratio of the electronic stopping of He to that of H — S_{He}/S_H — for Na and jellium also agree reasonably well with each other. The differences are within $\sim 20\%$ in the velocity range shown.

7.3.2 The bulk vs the film

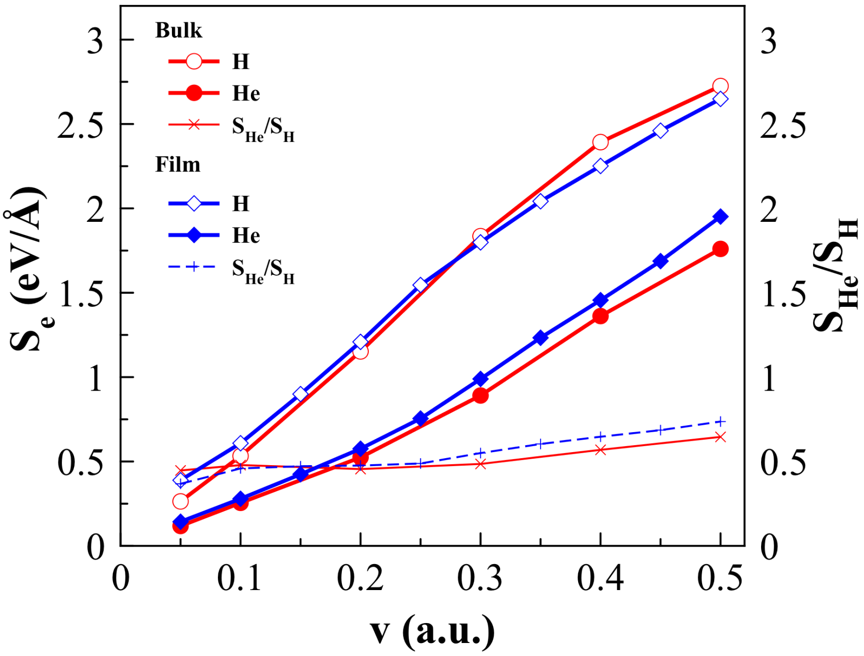

Figure 7.2: Electronic stopping power of slow H and He in an 8 unit cell thick film and the bulk Na.

In Fig. 7.2 we plot the electronic stopping power of H and He in the film and the bulk Na. As the figure shows, the stopping power for the bulk Na is slightly different than the film. It is interesting that, in the velocity range shown in Fig. 7.2, the latter always has higher stopping for He in contrast to H for which the stopping power is slightly smaller than the bulk for $v > 0.3$ a.u..

Fig. 7.3 shows the change in the electronic excitation energy $E - E_{gs}$ as the projectile moves for the four cases with H and He projectiles and the bulk and the film targets. Here, E is the electronic energy of evolved system while E_{gs}

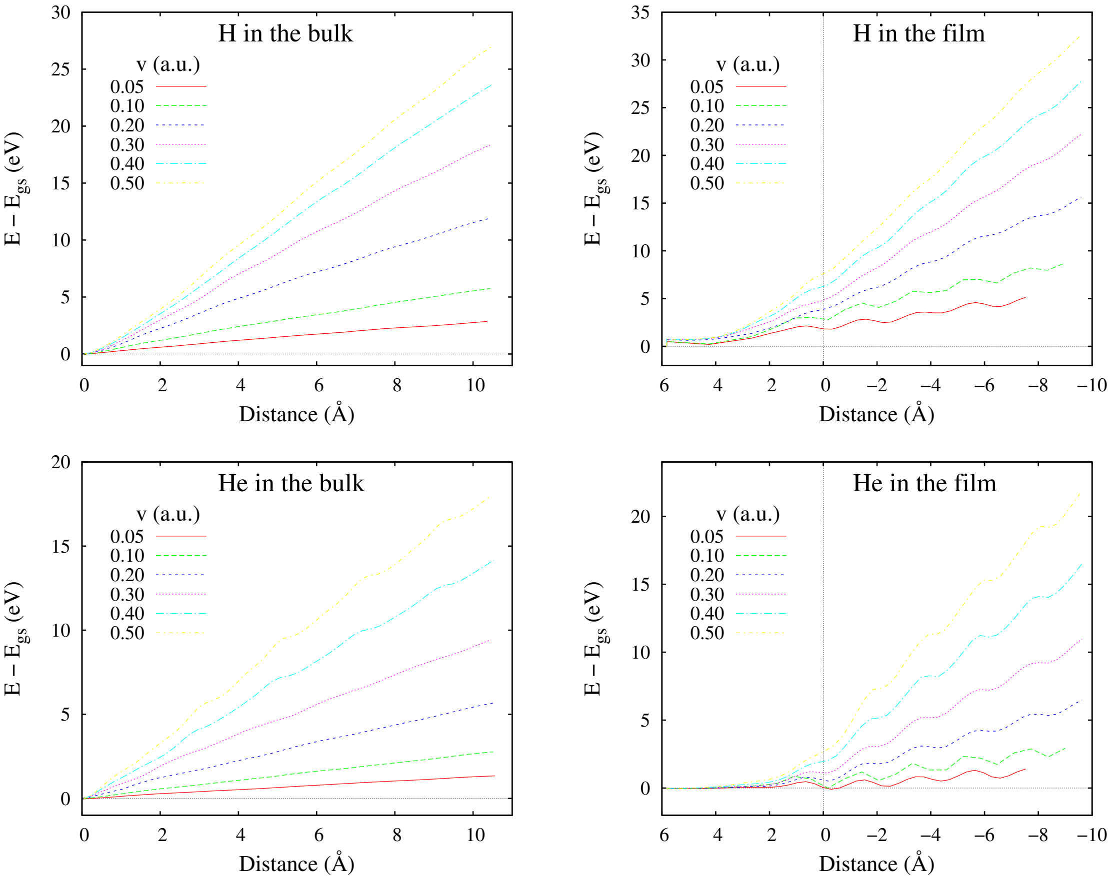

Figure 7.3: The change in the electronic excitation energy $E - E_{gs}$ as a function of the distance travelled by the projectile for the H (top row) and He (bottom row) projectiles and the bulk Na (left column) and the Na film (right column) targets. The horizontal axes of the plots show the distance measured from the projectile's initial position in the case of the bulk target and from the top atomic layer on the front surface of the film in the case of the film target. Electronic stopping power is taken as the average slope of these curves after the initial transient.

is the ground state electronic energy for the corresponding atomic arrangement. The horizontal axes of the plots show the distance measured from the projectile's initial position in the case of the bulk target and from the top atomic layer on the front surface of the film in the case of the film target. As can be seen, the initial transients in the energy for the bulk and the film cases are different as the projectile is present inside the bulk in the former case when the simulation

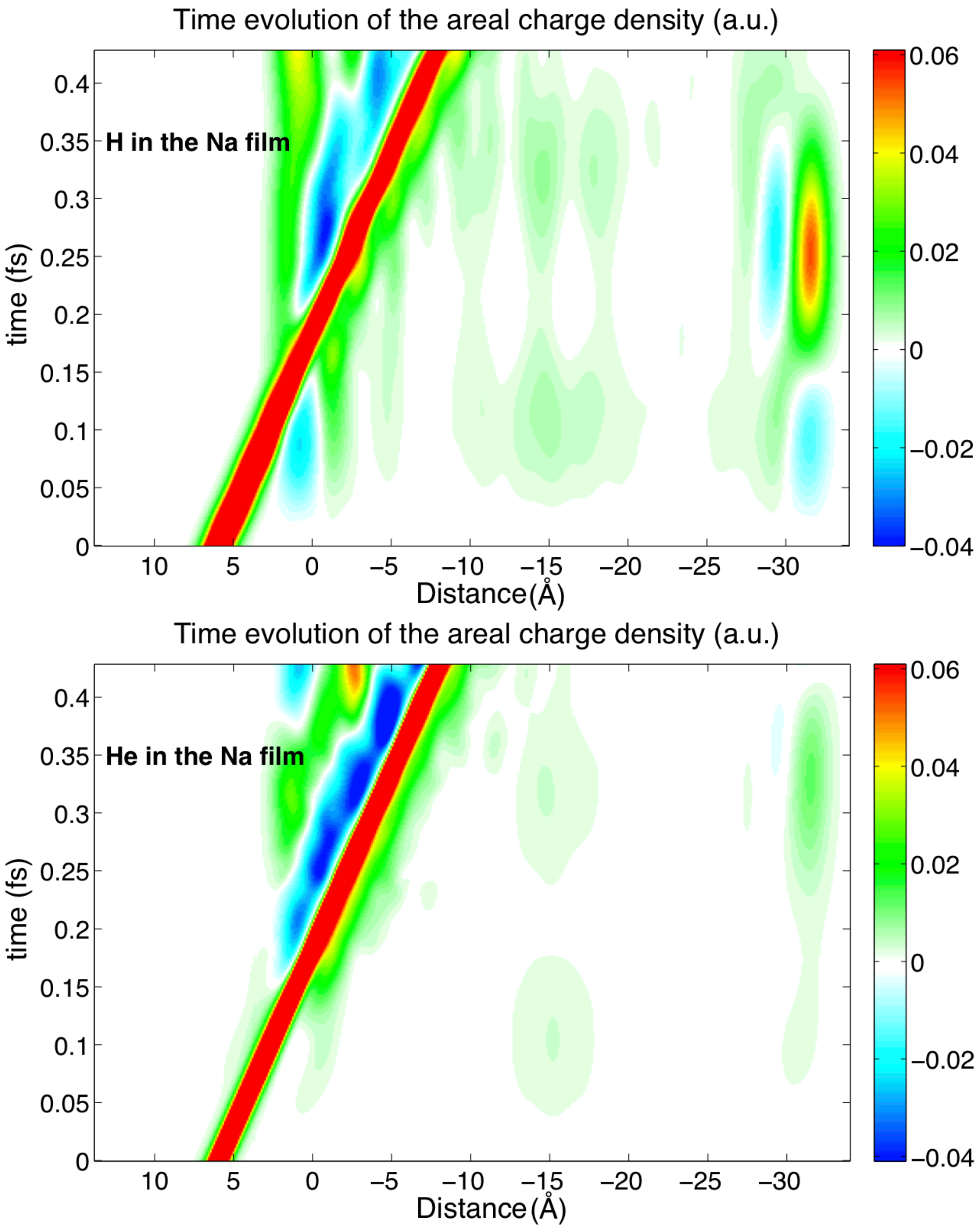

Figure 7.4: The time evolution of the change in the average areal electron density in the xy-plan as a function of the position along the film width, the z-direction, as a H (top) or He (bottom) projectile enters it. The position is labelled by the distance from the top atomic layer on the front surface of the film.

starts. However, the stopping power shown in Fig. 7.2 is calculated from the average slope of the energy vs distance curve only after it becomes stationary. Thus the difference in the stopping power calculated for the bulk and the film arise only due to the difference in their responses to the perturbation.

Comparing the bulk and the film plots in Fig. 7.3, we can see that the $E - E_{gs}$ curves for the film are much more oscillatory meaning that the position dependence of the electronic stopping is quite strong in case of the film while the bulk behaves more like a uniform electron gas. Remember that the film we consider is just 8 unit cell thick so its interior is not exactly like a bulk crystal.

7.3.3 Surface effects

In Fig. 7.4, we plot the change in the average areal charge density in the xy-plan as a function of the distance along the z-direction and time for the film case for the projectile velocity $v = 0.05$ a.u.. As in Fig. 7.3, the horizontal axes of the plots show the distance measured from the top atomic layer on the front surface of the film. Comparing the H and He projectiles — the top and the bottom plots — the response to the He atom stays very weak until it enters the film at about 0.15 fs while the H atom induces longitudinal oscillations in the electron density even when it is 5 Å away from the surface (at about 0.05 fs) and has travelled just more than an Å towards it. This is also seen in the right column of Fig. 7.3: compared to He, when a H atom moves towards the film, it not only excites a lot more electrons, it does so from a larger distance. He perturbs the electrons only when it reaches the film electrons. Note that relaxing the structure of the film pulls the atoms in the surface layers inwards by upto ~ 0.5 a.u., however, as we checked for $v = 0.5$ a.u., it does not alter the electronic stopping power for any of the H or He projectiles. Coming back to Fig. 7.4, we see that while travelling inside the film both projectiles induce a wake-like feature in the valence electron density as expected. We see that, compared to the H atom, the charge density oscillation behind the He atom is larger in the magnitude and shorter in the “wavelength” . However, H induces a much stronger oscillation at the far end of the film at ~ 0.25 fs whereas the corresponding feature in the He plot is at ~ 0.30 fs, which is not only much weaker but also delayed by ~ 0.05 fs. Since at

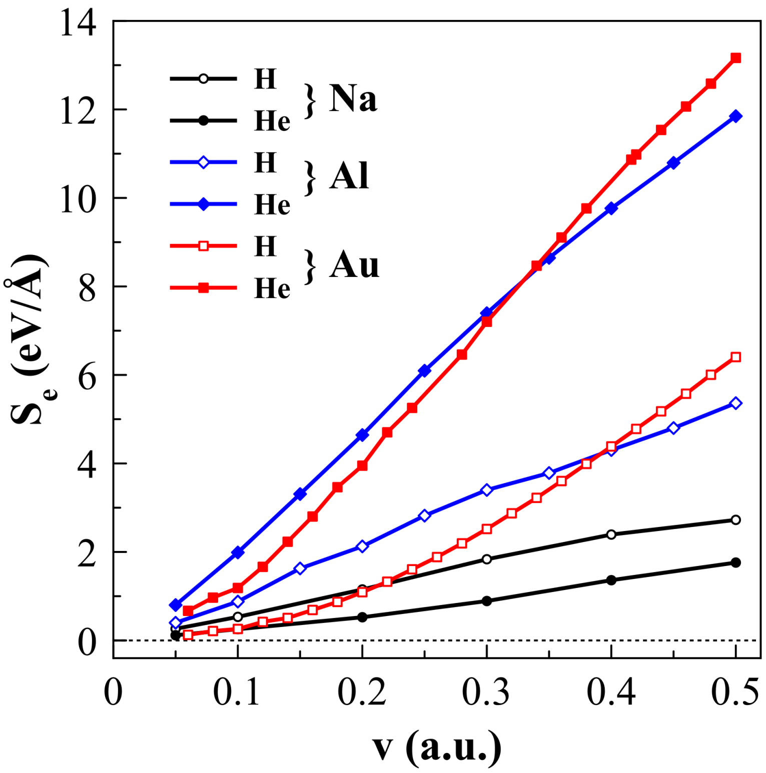

Figure 7.5: Electronic stopping power of slow H and He in metals — Na, Al and Au. Na that has low valence electron density ($r_s > 2.77$) offers a higher stopping to H than He.

$v = 0.05$ a.u., comparing the film and the bulk targets (see Fig. 7.2), the stopping power of H is lower in the film while that of He is higher in the film, the role of the oscillations in the charge density seems to lower the stopping. However, this needs more investigation and is not the final word.

7.3.4 Na, Al and Au

In Fig. 7.5, we compare electronic stopping power of H and He in Na, Al and Au. We see that for Na and Al, the stopping power is linear with the projectile velocity for both H and He projectiles. However, in case of Au, the slopes of the stopping curves change with the velocity as described in detail in chapter 5.

Fig. 7.6 shows results from Ref. [18] for jellium calculated using scattering

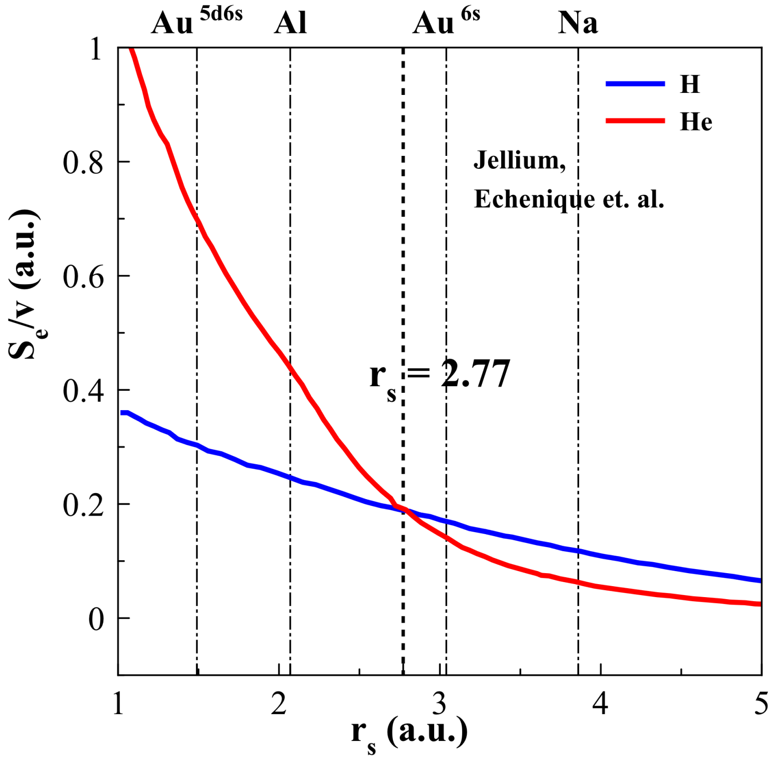

Figure 7.6: Stopping power of slow H and He in jellium as a function of electron density, from Echenique et al., Ref. [18]. Electrons at the fermi surface are scattered by the screened potential of the projectile. The scattering potential of static projectile atom calculated self consistently using density functional theory is used.

theory [101] with scattering potential of the projectile calculated using density functional theory. The slopes of the $S_e(v)$ curves for H and He are plotted against the electrons density parameter r_s. As mentioned in the introduction above and in section 1.7.1, the stopping power of He is larger than that of H for a high density jellium with $r_s < 2.77$ and the converse is true for jellium with low electron density ($r_s > 2.77$). The average density of valence electrons in Na and Al correspond to $r_s = 3.86$ and 2.07. In Au, considering only s electrons (Au^{6s}) gives $r_s = 3.04$ and all 11 s and d electrons (Au^{5d6s}) gives $r_s = 1.49$. These r_s values for the three metals are marked in Fig. 7.6 with vertical dot-dashed lines. Keeping these numbers in mind, we see that in Fig. 7.5, the relative stopping power of H and He agree with the jellium model: in Na, H has a higher stopping than He, whereas in Al and Au^{5d6s}, the opposite is true.

At $v \geq 0.2$ a.u., although, there is a small velocity window where the stopping power of both projectiles in Au are lower than Al, the slopes of the stopping curves are still larger for Au that, considering that its d electrons also taking part in the stopping process, has a higher valence electron density than Al. However, it is surprising that, even if we consider only s electrons in Au, its r_s is smaller than that for Na, but, stopping of H is smaller in Au than in Na at low velocities ($v < 0.2$ a.u.). Since Na agrees with the jellium model, as in we see in Fig. 7.1, this implies that behaviour of the valence electrons in Au differs from a free electrons gas even at low velocities when only s electrons are considered actively contributing in the stopping — the same conclusion we reached in chapter 5 before.

7.4 Summary

Electronic stopping power of H and He in the bulk Na and a film (8 unit cell thick) of it are calculated. We find good agreement with previous theoretical results for a homogeneous free electron gas target for the absolute and relative electronic stopping power of H and He projectiles. The stopping changes linearly with projectile velocity and shows no threshold effect for H and He projectiles. The difference between the stopping power in the bulk and the film targets is attributed to the charge density oscillations close the film surface but is surprisingly small.

Chapter 8

Electronic stopping power of H and He in LiF

8.1 Introduction

The electronic stopping power in insulators is expected to be substantially depressed for velocities below a threshold related to the finite band gap [34]. Experimental results on several insulators covering velocities down to ~ 0.2 a.u. were not clearly displaying such behaviour, [37–39] except under grazing incidence, which showed a threshold velocity of $v \simeq 0.2$ a.u. in LiF [40]. LiF was chosen as paradigmatic insulator, with its large band gap (in excess of 13 eV). Recent experiments managed to measure velocities as low as 0.1 a.u.[41, 42] displaying a clear velocity threshold, and first-principles simulations based on TD-DFT were able to reproduce the behaviour, albeit with a clear underestimation of the stopping power and overestimation of the threshold [29]. The simulation focused on the proton - antiproton comparison (achieving a remarkable agreement in the Barkas effect [29]), but was using a simplified description of the projectile, both for the basis set and for the potential. In this chapter, we calculate the electronic stopping power of H and He in LiF using the Ehrenfest coupled electron-ion dynamics. We sample a range of impact parameters by offsetting the projectile's initial position from [001] channel axis at $(x/a, y/a) = (3/4, 3/4)$ (we call them "channels" henceforth). We find a significant improvement over previous TD-DFT results

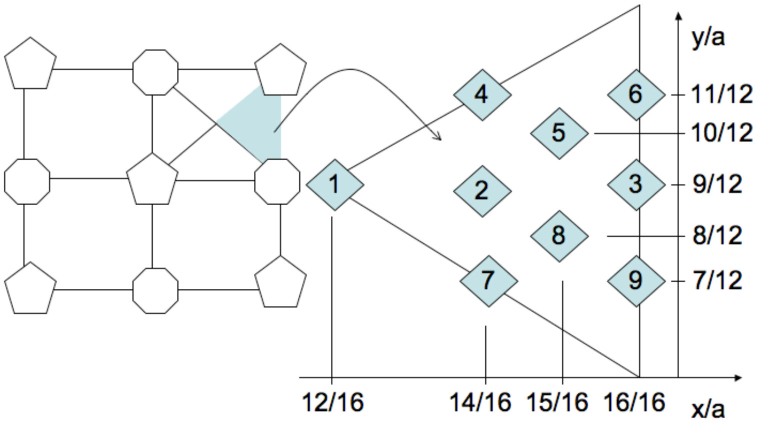

Figure 8.1: Position of [001] channels 1 through 9 in the xy-plane in the unit cell of LiF crystal. Sampling over the impact parameter is done using these channels. Two {001} (Li or F) atomic planes spaced $a/2$ are shown with two different symbols.

for H [29] and a good agreement with the experiments [42].

8.2 Computational Details

The local density approximation (LDA) for the instantaneous exchange and correlation energy functional in the Ceperley-Alder [122] form parametrized by Perdew and Zunger [123] was employed. All three electrons of Li and only valence electrons of F are considered explicitly. We use a double-ζ polarised split-valence basis for the valence electrons of the host material (LiF) as well as for the projectiles (H and He). The grid cutoff used for real space integration is 200 Ry [44, 45]. Relaxation of the cell size of bulk LiF gives a lattice parameter $a = 3.98$ Å. As expected for an LDA functional, it is slightly smaller than the experimental value (4.03 Å). A $2 \times 2 \times 4$ supercell with only the gamma point for the Brillouin Zone integrations is used.

Other than the most obvious choice for a [001] channel at $(x/a, y/a) = (3/4, 3/4)$, we sampled eight more channels or impact parameters. These are shown in Fig. 8.1 and labelled 1 through 9. For every channel, the projectile is

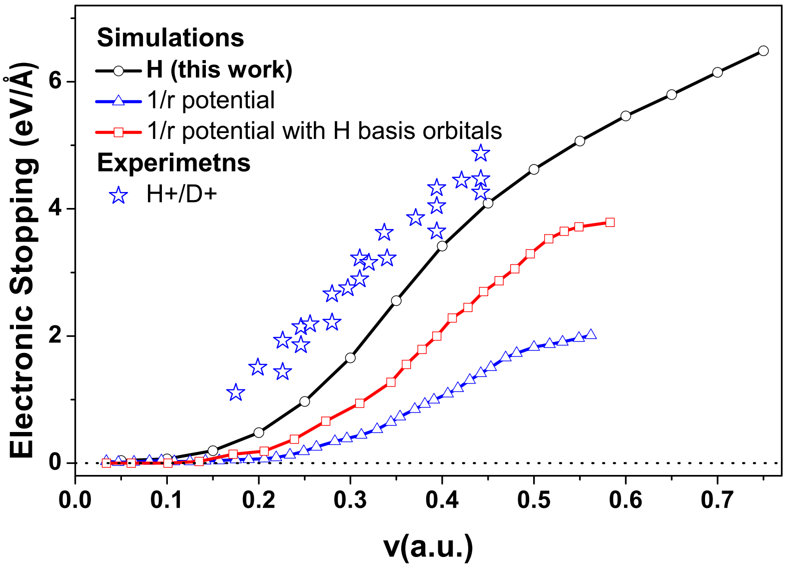

Figure 8.2: Electronic stopping power of H in LiF. Our results in a [001] channel (X, $(x/a, y/a) = (3/4, 3/4)$] are shown as black line with circles. Earlier TDDFT results from Ref. [29] with and without a chain of H basis orbitals along the trajectory are shown as red and blue lines with squares and triangles. Experimental results from Refs. [41, 42] are shown as stars.

given an initial velocity along the z-direction. A time step of 1 asec is used to integrate the coupled electron-ion dynamics until the projectile travels a distance of approximately $2a$. Electronic stopping power is extracted using the fitting scheme described in section 4.2.2, i.e., using the rate of change of the electronic excitation energy with the distance travelled by the projectile.

8.3 Results and Discussion

Fig. 8.2 shows our results for the electronic stopping power of H in LiF in channel 1. We also plot the experimental data [41, 42] and earlier TDDFT results [29] for a proton projectile represented by its bare (Fourier filtered) Coulomb potential. The host nuclei were fixed in Ref. [29] and only the dynamics of electrons was considered. Given the fact that there were no basis functions associated to the projectile and only the basis states of the host were used to describe the electrons

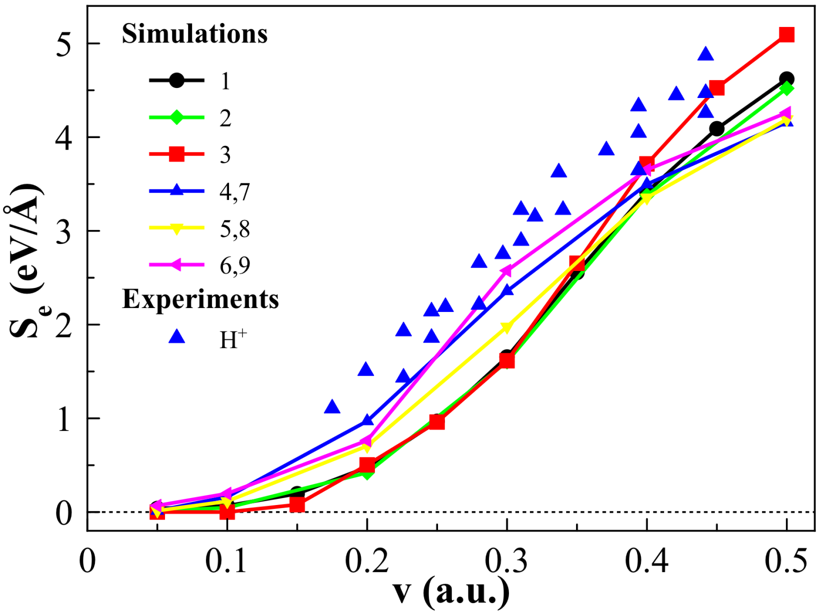

Figure 8.3: Electronic stopping power of H in LiF for various channels shown in Fig. 8.1. Comparison is made with the experimental results from Refs. [41, 42].

and their deformation to screen the projectile, a basis deficiency was expected then, which was corroborated by the substantial change in the electronic stopping power when corrected by inserting extra atomic orbitals along the path of the projectile [29]. Both (corrected and uncorrected) curves for the electronic stopping power from that paper are reproduced in Fig. 8.2, where they are compared with the results of the present study and the experimental ones. It is apparent that the full description of the projectile, with a moving basis set, and the use of the full ion-electron dynamics, offer a considerable improvement in the simulation with respect to Ref. [29].

As can be seen in Fig. 8.2, our results (black line with circles) show the same trend at low velocities as that of Ref. [29]. The electronic stopping power increases from zero smoothly around $v = 0.1$ a.u., the slope of the curve increasing with v for $v \leq 0.4$ a.u. and decreasing at higher velocities. Although the agreement is greatly increased, especially at high velocities, the threshold effect is overestimated in the simulations. In addition to possible deficiencies in the theory, let us stress here an important difference between theory and experiment: the theory

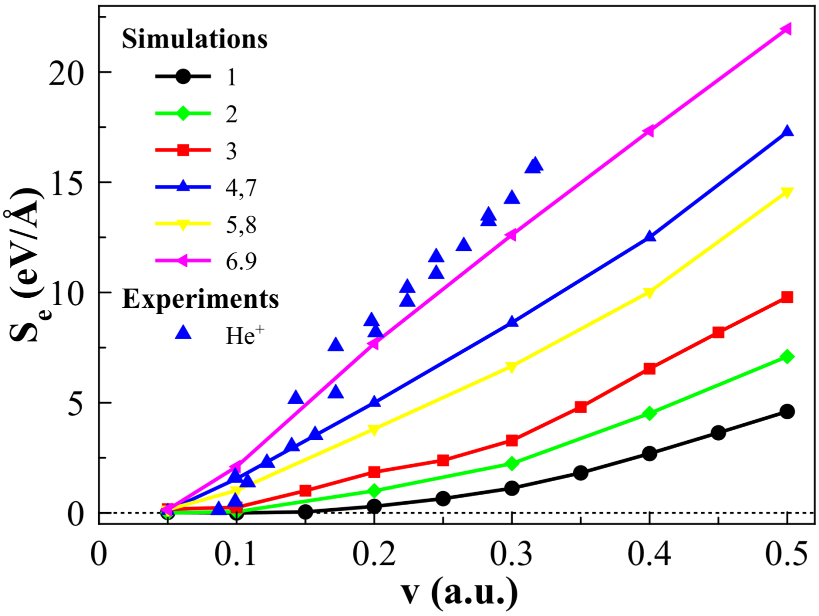

Figure 8.4: Electronic stopping power of He in LiF for various channels shown in Fig. 8.1. Comparison is made with the experimental results from Ref. [42].

simulates an ideal [001] channel, channel 1 in Fig. 8.1, while experiments use a beam in which different ions have essentially the same propagation direction but different impact parameter with respect to the nuclei in the target.

Fig. 8.3 shows the stopping power of H in LiF for various channels shown in Fig. 8.1. For the three pairs of symmetry related channels, the figure shows the averages. As expected, an enhanced electronic stopping power is obtained when sampling over higher electron-density regions, e.g., channels 4, 5 & 6 (or 7, 8 & 9) that offer smaller impact parameters compared to channel 1. Actual stopping that can be compared with the experimental results is a weighted average over all possible impact parameters. Furthermore, the experimental results here are for polycrystalline samples for which the random orientations of crystallites make the small impact parameter scattering highly probable. We have not averaged the results over the sampled channels (impact paramters) as there is no simple criteria to determine their relative contributions.

We can see in Fig. 8.3 that, compared to channels 4-9, channels 1,2 and 3 that offer relatively larger impact parameters give lower stopping for $v \leq 0.40$ a.u.,

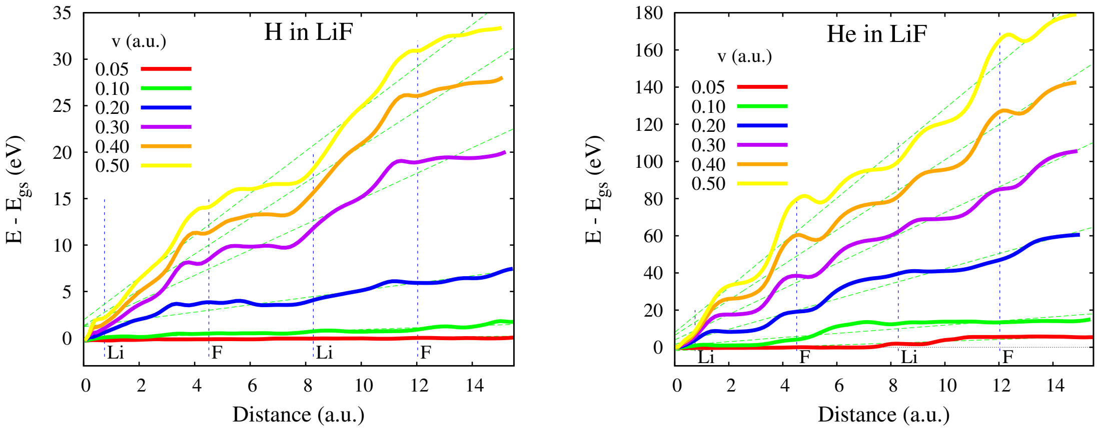

Figure 8.5: Position dependence of the electronic stopping power for H and He moving in LiF channel 6. The excess electronic energy $E - E_{gs}$, i.e., the difference between the energy of evolved electronic state and the ground state with the same atomic configuration, is plotted against the distance travelled by the projectile along the channel axis. Electronic stopping is the slope of these curves.

but higher stopping for higher velocities shown in the figure. Thus overall, even taking a simple average over channels 1-9 leads to a much better agreement with the experiments. As, can be seen in Fig. 8.3, sampling over channels with lower impact parameters pushes the threshold velocity down. Thus by averaging over the channels the threshold effect is reduced.

Stopping power of He in LiF is shown in Fig. 8.4 for the same channels discussed above. The experimental results taken from Ref. [42] are also plotted for comparison. Unlike the H case, our simulations hugely underestimate the stopping power of He in LiF, especially for channel 1 for $v \leq 0.10$ a.u.. Channels 6 and 9 that offer very small impact parameter, closely reproduce the experimental results for $v \leq 0.10$ a.u., but the slope of $S_e(v)$ curve for these channels is still marginally underestimated producing a lower threshold velocity ($\sim$ 0.05 a.u.) compared to the experiments ($\sim$ 0.09 a.u.). As can be seen in Fig. 8.4, the slopes of the other curves are even smaller. However, as expected, the lower the impact parameter, the higher the stopping and the slope of the stopping curve. But, compared to the H case, the differences are unexpectedly huge. For example, at $v \leq 0.5$ a.u., the ratio of the highest to the lowest stopping for channels 6,9 and

1 is about 5. The difference between the variation of H and He stopping with impact parameter is likely to be due to the difference in the sizes of these projectiles. A He atom is almost half the size of a H atom and the electron cloud of 1s orbital of a He atom is much more compact with peak electron density about four times higher than the corresponding orbital of a H atom. When a H atom is inside a solid, the electronic state bound to it resonates with the bulk spectrum of the solid, i.e., its valence band states, and spreads out. On the other hand, the electronic state bound to a He atom is much deeper in energy and hence, relatively speaking, keeps its identity. In other words, He nucleus will be much better screened than H's in the channel. This makes He much more sensitive to probe the target electron density gradients leading to larger differences in the electronic stopping for different impact parameter channels.

The stopping power presented above is the average slope of the electronic excitation energy vs distance curve. However, as we see in Fig. 8.5, the rate with which the projectile excites the electrons strongly depends on its position when we consider a channel offering small impact parameter, e.g, channel 6 and 9. Positions of Li and F atoms (or Li^+ and F^- to be more precise) that are the nearest atoms along the projectile trajectory are marked with vertical dotted lines. It is interesting that in case of H, the "local stopping" is very small when it is moving from F to Li and is quite large when it is moving from Li to F. On the other hand, He excites the electrons relatively more uniformly, with both the high and the low stopping regions occurring between the two types of the host atoms irrespective of the direction of motion relative to them. This means that this position dependence is not directly linked with the Li and F positions but arises due to some other reason. We leave further investigation of this to future work.

8.4 Summary

Theoretical simulations from first principles for the low-velocity electronic stopping power of light projectiles in LiF have been presented. For H projectile, a considerable improvement on previously reported simulations has been found. Compared to the experiments, our simulations overestimate the threshold effect.

Sampling a range of impact parameters leads to a better agreement of electronic stopping power with the experiments.

Chapter 9

Electronic stopping power in quartz, magnesia, alumina, zircon and SiC

In the previous chapter, LiF was introduced because it is the best studied — both theoretically and experimentally — wide band gap insulator in this field. As we see there, it shows some unexpected unknowns: the so very different impact parameter dependence when changing projectile from H to He. Some questions also arise there, e.g., how to average over the impact parameter to compare with the experiments? Apparently, it seems that the trajectories through denser regions are closer to the experiments. It also shows a threshold behaviour that should depend on the band gap but in a way that is still not understood. This stimulates further characterisation of the situation by making a comparative study with different insulators. We select quartz, magnesia and alumina — SiO_2, MgO and Al_2O_3 — because they represent varying packing of their structures (related to varying chemistry). Zircon is chosen because it is a prototypical case very heavily studied for nuclear waste storage. There is also interest (in both fundamentals and applications) in heavy projectiles. We consider Au in SiC because this projectile-target system has been extensively studied [136, 137].

9.1 Quartz, magnesia and alumina

9.1.1 Introduction

In this section we consider H and He projectiles moving in SiO_2, MgO and Al_2O_3. In case of quartz that has a narrow and a wide [001] channel, we consider both these and also sample low impact parameters by choosing an offset from the wide channel axis as the projectile's initial position. We find a good agreement with the available experimental data for H and He in quartz and alumina. Electronic stopping for projectile velocities down to $v = 0.05$ a.u. is calculated for all projectiles. We also consider Li in Al_2O_3.

9.1.2 Computational Details

The local density approximation (LDA) for the instantaneous exchange and correlation energy functional in the Ceperley-Alder [122] form parametrized by Perdew and Zunger [123] was employed. A double-ζ doubly polarised split-valence basis is used for all atoms. The grid cutoff [44, 45] for real space integration is 200 Ry and only the gamma point is considered for sampling the Brillouin zone. These details apply to all cases studied in this chapter.

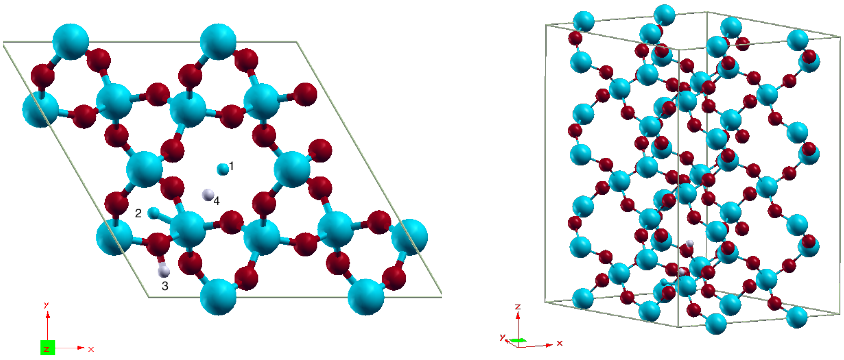

Figure 9.1: Crystal structure of α-quartz and the positions of the four [001] channels 1-4 in the xy-plane in its unit cell marked with small balls and labelled. Channel 1 and 2 are at the centres of the big and small hollow channels while channel 3 and 4 are used to sample smaller impact parameters in the bigger channel along the projectile trajectory.

Quartz has chemical formula SiO_2. We considered α-quartz with lattice parameters of the hexagonal crystal lattice: $a = b = 4.916$ Å and $c = 5.4054$ Å [138]. α-quartz has 3 formula units per unit cell. We used a $2 \times 2 \times 3$ supercell containing 12 SiO_2 formula units or 108 Si and O atoms. The structure of quartz is sparsely packed, showing ample interstices and channels of low electron density, e.g., a prominent wide and a relatively narrow channel along the c-axis at $(x, y) = (2.458, 2.458)$ Å and $(x, y) = (0.15, 2.80)$ Å in the supercell shown in Fig. 9.1. We considered both these as well as two more "channels" inside the big cavity with smaller impact parameters at $(x, y) = (0.4916, 0.8515)$ Å and $(x, y) = (1.9664, 3.4059)$ Å. The electronic stopping power of H and He projectiles is calculated for these four channels labelled 1,2,3 and 4 in Fig. 9.1. Electronic stopping power is extracted as the average slope of the electronic energy vs distance curve as described in section 4.2.1.

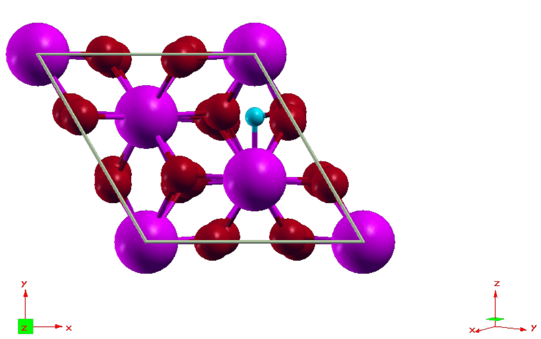

Figure 9.2: Crystal structure of α-alumina and the position of the [001] channel in the xy-plane in its unit cell marked with a small ball.

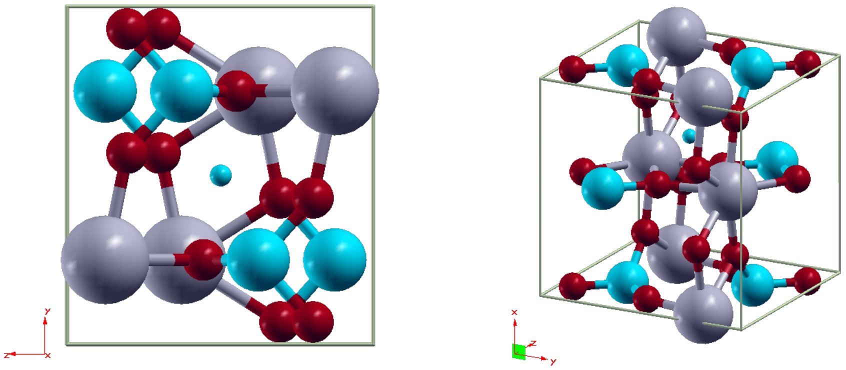

Figure 9.3: Crystal structure of zircon and the position of the [001] channel in the xy-plane in its unit cell marked with a small ball.

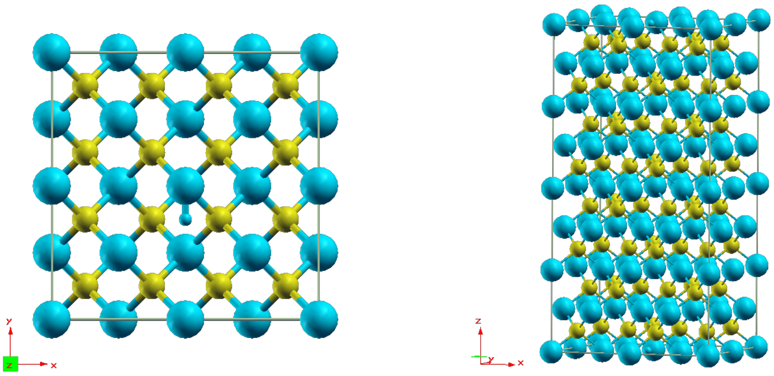

Figure 9.4: Crystal structure of α-SiC and the position of the [001] channel in the xy-plane in its unit cell marked with a small ball. $2 \times 2 \times 4$ supercell is shown in this figure.

Magnesia, MgO, has rock salt structure. The relaxed lattice parameter obtained is a = 4.2086 Å that is slightly smaller than the experimental value of 4.217 Å [139]. We used a $2 \times 2 \times 4$ supercell containing 128 Mg and O atoms or 64 MgO formula units. The stopping is calculated for H and He atom projectiles in a [001] channel at $(x/a, y/a) = (3/4, 3/4)$. Electronic stopping power is extracted as the slope of a straight line fitted on the electronic energy as described in section 4.2.1.

Alumina or corundum, Al_2O_3, has corundum structure with lattice parameters of its hexagonal crystal lattice $a = b = 4.7540$ Å and $c = 12.9820$ Å [140]. It has 6 formula units per unit cell. We used a $2 \times 2 \times 1$ supercell containing 120 Al and O atoms or 24 Al_2O_3 formula units. The electronic stopping power of H, He and Li atom projectiles is calculated for a [001] channel in the middle of the supercell shown in Fig. 9.2. The projectile atom is shown placed in the channel as the smaller aqua sphere. Electronic stopping power is computed as the slope of a straight line fitted on the electronic excitation energy.

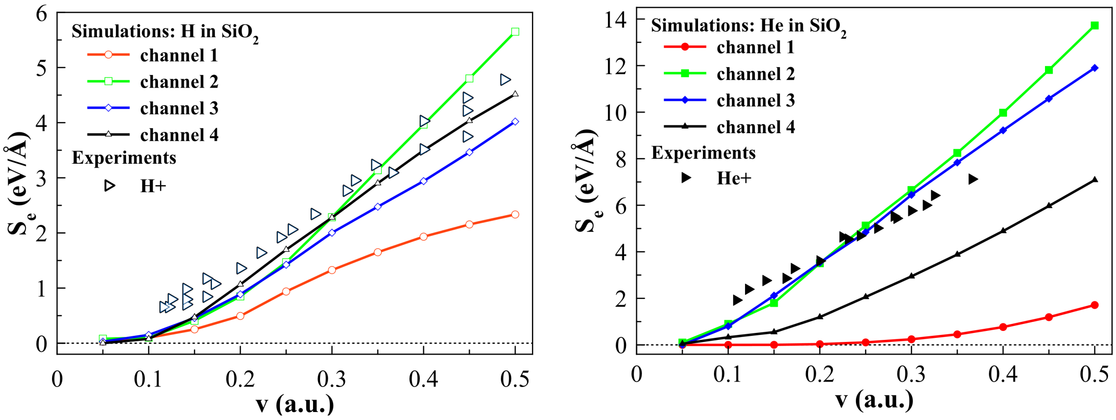

Figure 9.5: Electronic stopping power of H (left) and He (right) in α-quartz in the four channels 1-4 shown in Fig. 9.1. Comparison is made with the experimental results taken from Refs. [37, 42, 141].

9.1.3 Results and Discussion

Fig. 9.5 shows the electronic stopping of H and He in SiO$_2$ in four channels shown in Fig. 9.1. Experimental results [42] for polycrystalline SiO$_2$ are also plotted for comparison. We see that, just like the LiF case in chapter 8, simulations agree with the experiments mainly for the channels for which the projectile trajectory is closer to the target atoms. Similar to LiF case, the stopping power of H varies less when we move from a channel with low valence electron density to a channel with high valence electron density in SiO$_2$. As mentioned before in chapter 8, this difference in H and He stopping behaviour is likely to be due to the difference in the size and the density of electron clouds of these projectiles. The dependence of stopping on the channel in SiO$_2$ is more sensitive as compared to the LiF case. This makes sense because of the presence of channels with much lower density in SiO$_2$.

For H, we find a velocity threshold of $v_{th} \sim 0.05$ a.u. which is the same as obtained by linearly extrapolating the experimental data. However, for He projectile, unlike the experiments that would give no threshold by a linear extrapolating down to $v = 0$, we find that the stopping power practically vanishes at $v \leq 0.05$ a.u. for all four channels considered. For channel 1 that, compared

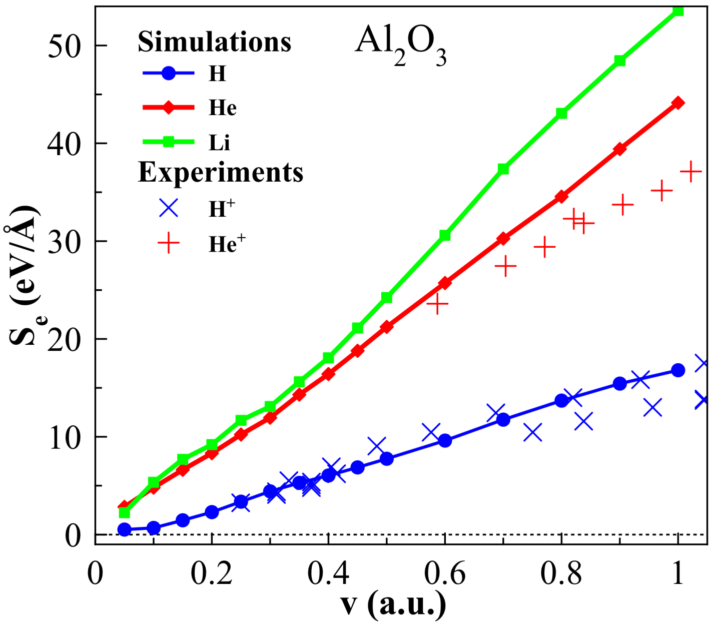

Figure 9.6: Electronic stopping power of H, He and Li in Al_2O_3. Comparison is made with the experimental results taken for H from Refs. [37, 142, 143] and for He from Ref. [141].

to other channels, has a lower density of valence electrons and offers a large impact parameter to the projectile moving on its axis centre, we find almost no electronic stopping even for a projectile moving with velocity as large as $v = 0.2$ a.u. (red curve with filled circles in Fig. 9.5). Interestingly, the ratio of stopping power of He to that of H is less than unity for channel 1 and larger than unity for other channels. That is, in the low density channel the stopping of H goes above that of He, in agreement with the stopping acting as if it depended on the low local density. It also raises the further point on how to average for directions and impact parameters in the calculations to compare with the experiments. Not easy! It seems, however, that the higher density ones have more weight in the averaging for some reason just like LiF case.

Fig. 9.6 shows our results for the electronic stopping power of H, He and Li in Al_2O_3. Experimental data for H [37, 142, 143] and He [141] is also plotted for comparison. First, we see that there is a good agreement between the calculated stopping powers and the experimental results. The slope of the He curve is

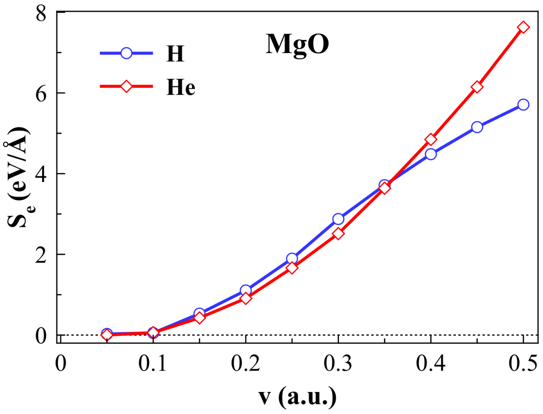

Figure 9.7: Electronic stopping power of H and He in MgO.

slightly higher than the experimental data but the latter extrapolates to it at lower velocities. It is interesting that stopping power of Li is only slightly higher than He at $v < 0.5$ a.u. and, at $v = 0.05$ a.u., it even becomes smaller than He. We find a threshold velocity $v_{th} \simeq 0.05$ a.u. for H but there is still appreciable electronic energy loss for He and Li at this velocity. A linear extrapolation of calculated stopping powers of these two projectiles gives no threshold for He and $v_{th} \simeq 0.02$ a.u. for Li.

Fig. 9.7 shows the electronic stopping power of H and He in MgO. We see that the energy loss in MgO for both H and He projectiles up to a velocity of $v = 0.1$ a.u. is negligible. Further, the stopping is quite similar for the two projectiles at $v \leq 0.4$ a.u. but the increasing slope of the He curve means that it is going to be substantially higher at higher velocities.

Let's now compare the three materials considered above — SiO_2, MgO and Al_2O_3. Since we present electronic stopping that is energy loss per distance travelled, we need to consider the compactness of the materials along the channel axes for a valid comparison. The values of the average volume per atom for SiO_2, MgO and Al_2O_3 are 2.95, 2.21 and 2.05 Å^3 per atom. Now coming to the channel openness that would affect the local electron density along the projectile trajectory (which does not deviate much from the channel axis in all cases), we have approximate average distances to the nearest neighbours along the channel axis as 2.46, 1.48 and 1.19 Å for SiO_2 (channel 1), MgO and Al_2O_3. From

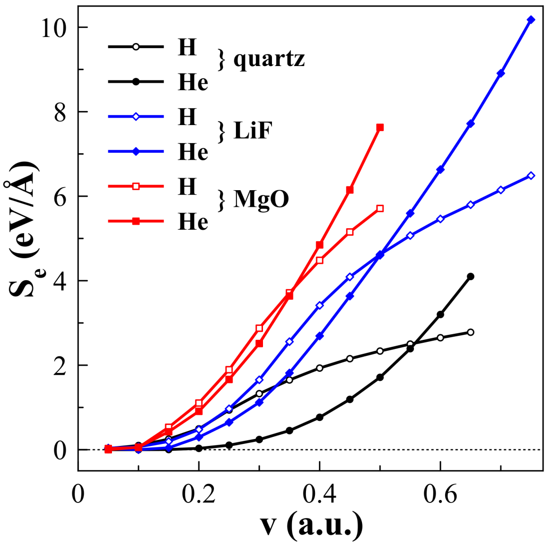

Figure 9.8: Electronic stopping power of H (open symbols) and He (filled symbols) in three wide band gap insulators: α-quartz (channel 1 shown in Fig. 9.1), LiF (channel 1 shown in Fig. 8.1), and MgO.

Figs. 9.5-9.7, we see that the stopping increases when we go from SiO_2 to Al_2O_3 through MgO as the local electron density increases as a result of small impact parameter and more compact atomic structure. At $v = 0.5$ a.u. for example, values of S_e for these three materials are approximately 2.33, 5.7 and 7.5 eV/Å for H and 1.71, 7.6 and 21 for He projectile, just in the expected order of decreasing impact parameter. Interestingly, adiabatic simulations with a phenomenological descriptions of the electronic stopping are performed by introducing the latter as a friction term dependent on the local electron density in the nuclear dynamics [144–146].

In Fig. 9.8, we compare our results for SiO_2, LiF and MgO. We see that like in a low density jellium (with $r_s < 2.77$), electronic stopping of H is higher than that of He in these media for a range of low velocities. In the velocity range shown in Fig. 9.8, the slopes of He stopping curves show two distinct velocity regimes: at low velocities it is continuously increasing and at higher velocities it is constant. In contrast, the slope of the H stopping curves decreases after an initial increase. Why this happens is an interesting question. We leave it as an open question for the future work.

9.2 H and He in zircon

9.2.1 Introduction

Zircon, $ZrSiO_4$, is an important material considering its potential for the nuclear waste encapsulation due to its mechanical and chemical durability. Nuclear waste contains radioactive elements that constantly tend to damage the structure of the host material. For example when a U^{238} atom decays to a Th^{234} atom, an α particle is released with an energy of 4.198 MeV while the recoiling Th has 72 keV. The emitted α particle moves at a speed of 6.50 a.u., whereas the recoiling Th moves at a speed of about 0.11 a.u.. The former is the main source of electronic heating in an α-decay event. However, the speed of the recoiling heavy atom is large enough that it may fall in the super-threshold regime for the electronic stopping. If so, the radiation damage simulations employing the Born-Openhenimer approximation would not work as the forces on the nuclei are modified due to the electronic excitations. Although, most of the damage produced is caused by the heavy recoiling atom, the contribution of the lighter particle is also substantial as it slows down [147, 148]. Here we study slow lighter particles moving in zircon crystal under channeling conditions. We calculate the electronic stopping of H and He in zircon. We find that the threshold velocity for these two projectiles is much smaller than Th recoil velocity in an α-decay. Thus assuming that the threshold does not strongly depend on the projectile, the electronic stopping effects even for a slow moving Th atom are important and should be included in the radiation damage simulations. Furthermore, we find that compared to LiF, quartz and MgO, the velocity dependence of the electronic stopping of He in zircon is very different below $v = 0.2$ a.u..

9.2.2 Computational Details

Zircon has tetragonal crystal lattice with lattice parameters $a = b = 6.6069$ Å and $c = 5.9894$ Å [149]. It has 4 formula units per unit cell. We used a $3\times1\times1$ supercell

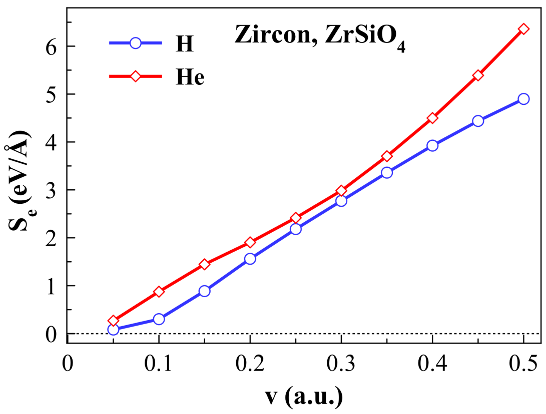

Figure 9.9: Electronic stopping power of H and He in zircon.

containing 12 $ZrSiO_4$ formula units, i.e., 72 atoms. The H or He atom projectile is given a velocity along the x-direction in a channel at $(y/b, z/c) = (1/2, 1/2)$ shown in Fig. 9.3 and the electronic stopping power is calculated. Other details are the same as given in section 9.1.2. Electronic stopping power is extracted as the average slope of the electronic energy vs distance curve, the same method that is used in case of MgO above.

9.2.3 Results

Fig. 9.9 shows the electronic stopping power of H and He in Zircon. Just like in MgO, the electronic stopping of the two projectiles in zircon is of comparable magnitudes and of the same order as in MgO and LiF. However, compared to LiF, SiO_2 and MgO, the stopping power of He in $ZrSiO_4$ shows a different behaviour with the projectile velocity v below $v \sim 0.2$ a.u. where its slope is higher at lower velocities and decreases with the velocity. We see that in $ZrSiO_4$ the threshold velocity v_{th} for H and He projectiles is smaller than 0.05 a.u. and is a little higher for H than He. This shows the importance of the methods simulating the radiation damage, for example, by Duffy et al. [4–8], which include the electronic stopping that in some materials can be significant even when the atoms are moving as slow as with a velocity of about 0.1 a.u..

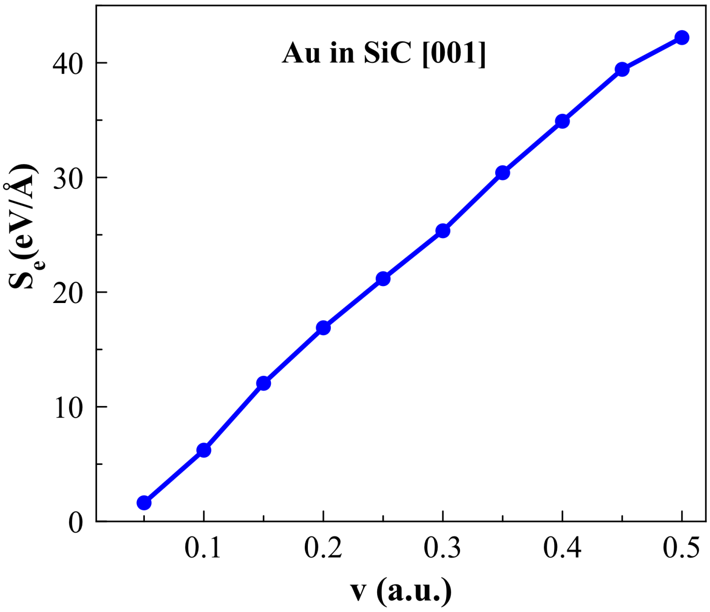

Figure 9.10: Electronic stopping power of gold in [001] channel of SiC.

9.3 Au in SiC

9.3.1 Introduction

SiC is an important material for high temperature and high voltage applications due to its chemical and mechanical stability under these conditions. The effects of ionising radiations, that are present in harsh environment of nuclear reactors, on various allotropic forms of SiC has been extensively studied due to its relevance to the fusion reactors, e.g., International Thermonuclear Experimental Reactor (ITER) [150, 151], see for example, Ref. [152] and references therein. Experimental characterisation of heavy ions irradiation on SiC has been done for many elements, for example, Ag, Pd, Pt and Au [136, 137, 153–155]. Not only that the electronic stopping of heavy projectiles in compound targets is not well described in the literature, the available experimental and theoretical data is not consistent [152]. Here, in this section, using our *ab initio* method, we calculate the stopping of a slow Au atom ($v = 0.05 - 0.50$ a.u.) in [001] channel of SiC. Experimental data is not available at such low velocites though.

9.3.2 Computational Details

We considered β-SiC or $3C$-SiC. It has Zinc Blend structure with lattice parameter $a = 4.36$ Å [156, 157]. We used a $2 \times 2 \times 4$ supercell containing 128 Si and C atoms or 64 SiC formula units. The stopping is calculated for a gold atom projectile in a [001] channel at $(x/a, y/a) = (1, 3/4)$, shown in Fig. 9.4, by shooting it along the z-direction with a given initial velocity. Other details are the same as given in section 9.1.2. Electronic stopping power is extracted using the fitting scheme described in section 4.2.2. That is, using the rate of change of the electronic excitation energy with the distance travelled by the projectile.

9.3.3 Results

Electronic stopping power of Au in SiC is shown in Fig. 9.10. We see that the electronic stopping has a linear dependence on velocity in the velocity range shown. Au has a finite stopping power at velocities as low as $v = 0.05$ a.u., but, as expected for an insulator target, extrapolation of our results shows a threshold effect with $v_{th} = 0.025$ a.u. below which the energy transfer to the electrons in SiC becomes negligible.

9.4 Summary

We calculated the electronic stopping power of H and He in α-quartz, magnesia, zircon and β-alumina and a heavy projectile, Au, in SiC. The behaviour of the impact parameter dependence when changing projectile from H to He found for LiF target is also observed for quartz. Compared to the quartz, MgO and alumina that can offer relatively lower impact parameter show an increased stopping as expected. At very low velocities ($v \leq 0.2$ a.u.), the velocity dependence of the electronic stopping of He is very different in zircon than in other insulators considered in this thesis. In contrast to the extrapolated experimental results, we find a threshold velocity $v_{th} \simeq 0.05$ a.u. for He in quartz, the same as that for H in it. For the same two projectiles $v_{th} \simeq 0.1$ a.u. in MgO, but $v_{th} < 0.05$ a.u. in zircon. In alumina, $v_{th} \simeq 0.1$ for H, but extrapolation of our results finds no threshold effect for He. Unlike the jellium model prediction, for the

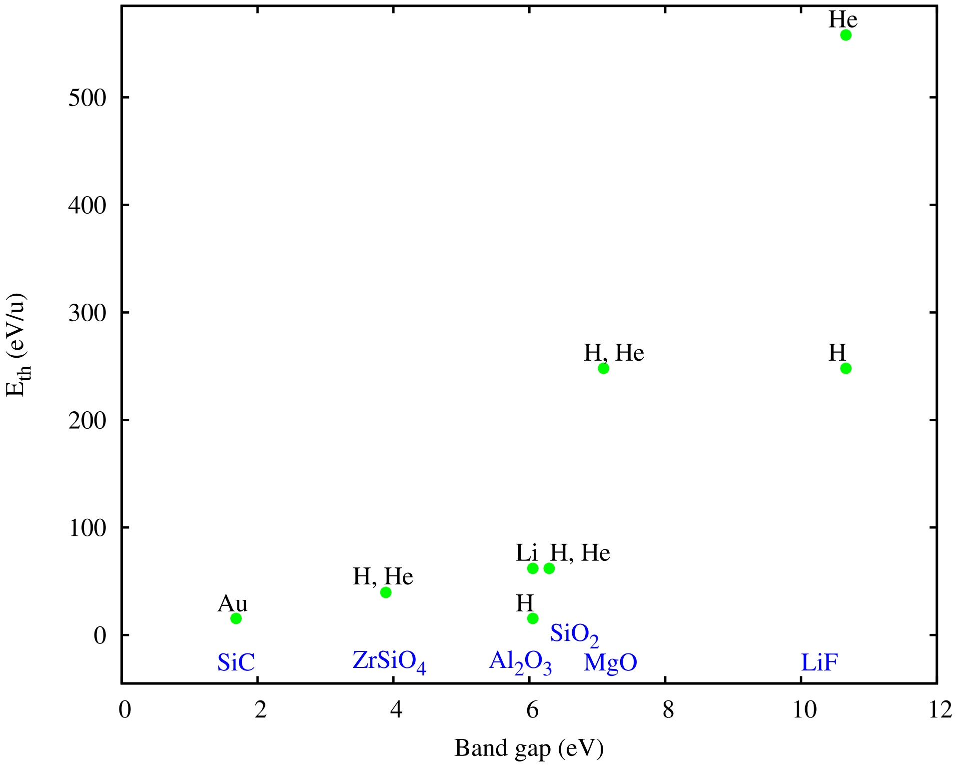

Figure 9.11: Energy corresponding to the threshold velocity plotted against the DFT band gap of various insulators. For quartz and LiF, results are for the lowest density or the highest impact parameter channels are plotted.

projectile-target combinations investigated in this chapter, stopping power is not linear with velocity at low velocities in general.

For the adiabatic molecular dynamics simulations that include the effect of electronic excitations, e.g., Refs. [4–8], the only input needed is the electronic stopping power and the threshold velocity of energy. Thus, the results presented in this thesis can be directly used with these methods for the radiation damage simulations.

In Fig. 9.11, the energy per nucleon E_{th} corresponding to the threshold velocity v_{th} of various projectiles is plotted against the DFT band gap of various insulators targets considered. For H and He projectiles, we see that v_{th} and E_{th} increase with the band gap. Electronic excitations across the band gap in a direct band gap insulator with parabolic bands would require E_{th} proportional to the band gap [34]. However, as we see in Fig. 9.11, there seems no systematic dependence of E_{th} on the band gap and its values are quite scattered. The fact that the model of Ref. [34] is not holding is not surprising as it was based on perturbation theory, but the projectile represents a large perturbation.

Chapter 10

Summary and outlook

In this thesis, non-adiabatic dynamics of a system of ions and electrons at the Ehrenfest level using TDDFT and SIESTA is used to simulate the passage of slow ions through solid matter and calculate the corresponding electronic energy gain. The pseudopotential description of atoms is employed and numerical atomic orbital basis set is used to describe the single particle electronic wavefunctions. As the ion-electron interaction depends mainly on the chemistry in this low energy regime, the pseudopotentials description of the core electrons is quite appropriate. The dynamics of the electrons is governed by the time evolution of the electronic wavefunctions while the nuclei follow the classical equations of motion under the action of forces calculated using the instantaneous electron density. Even though this is a mean field description of the electrons, here we show for the first time that it produces reasonably good agreement with the experimental results for the electronic stopping power of slow H and He in various types of materials considered in this thesis. The implementation of this TDDFT-Ehrenfest dynamics in SIESTA code can also serve a more general purpose of studying other non-adiabatic processes in large systems with usual first-principles accuracy.

We calculate the electronic stopping power of slow projectiles in various crystalline metals and ceramics as a function of projectile velocity v for $v \sim 0.05-0.50$ a.u.. We calculate stopping of H and He in gold, Al (three impact parameters), Na (bulk and an 8 unit cell thick film), LiF (six impact parameters), quartz (both wide and narrow [001] channels), MgO, zircon; and H, He and Li in alumina; and gold in SiC. We find reasonably good qualitative and quantitative agreement with the available experimental data. For H and He moving in gold, we also calculate the electron-hole pair spectrum around the fermi level by projecting the time evolved electronic state onto the ground state for the instantaneous nuclear configuration. We analyse the role of s and d-band electrons in stopping and, in contrast to the usual idea that at low projectile velocity only electrons close to the Fermi energy contribute to the stopping, we find that there is a significant contribution from deep lying states even for a slow projectile. In LiF and quartz for which we considered channels offering a variety of impact parameters, interestingly, impact parameter dependance for H is very different than that of He, which we speculate is due to their different effective sizes.

Owing to the diversity of the applications of the non-adiabatic processes due to the ion-election interactions in various areas of physics, chemistry and biology, a large number of future directions exist for our work. Limiting ourselves to just interaction of slow ions with matter, we still have a number of important things to understand.

For example, in experiments measuring the electronic energy loss and electronic stopping power, the target material is bombarded with a beam of ions. However, in our calculations, the coupled dynamics of ions and electrons is started, in contrast to the experiments, with the projectile being an atom just like all the other atoms in the simulation cell. To understand the charge capture by the ions and their neutralisation process as they enter the target, simulations are to be performed with the projectile ion initially outside the target solid with a well defined charge on it. In chapter 7, we considered a film but not only that film is too thin, the projectile starts with the self-consistent state just like the bulk target cases. To perform a more realistic simulation, with a thick enough film, parallelisation of the code is essential. If the projectile is away enough from the target at the beginning that the single particle states localised on the projectile can be separated from the target states, the experimental situation can be achieved with simply leaving the projectile state empty at each self consistent iteration and filling only the target states hoping to find a converged solution. Similarly, ions moving at grazing angles or parallel to the film surface can reveal the details of the charge exchange processes.

The oscillating rate of excitation energy with the projectile position or the "local" electronic stopping seen in case of small impact parameter channels in LiF (Fig. 8.5) is another interesting open question. Multiple regimes for the slope of the stopping vs velocity curves for H projectile in case of three insulators, SiO_2, LiF and MgO, (Fig. 9.8) is also not understood.

For a heavy projectile atom with internal electronic structure and a large enough size, the role of the dynamics of the core states on the electronic energy loss can be of interest in case of small impact parameter channels in solids. This can also be important in case of light projectiles as even the valence states are pseudised within a significant volume around the nucleus.

The effect of the electronic stopping on the nuclear energy loss is another interesting question that can be answered using the coupled ion-electron dynamics. However, it is more involved than it seems because the integrity of the answer depends very much on the accuracy of the forces on the nuclei.

Another more ambitious problem is treating the light nuclei like the protons quantum mechanically. This might not have much effect on the electronic stopping power but it might be relevant to diffusion of light nuclei through solids. How to treat negative ions and electron projectiles are other open questions.

In conclusion, a line of first principles simulations has been opened here, which should prove helpful in many different research fields from the space and nuclear industries to the treatment of cancer, and from quite applied to very fundamental. The importance of the electronic excitations in the radiation damage simulations is evident from the magnitude of the electronic stopping power of ions as slow as moving with a velocity of ~ 0.1 a.u., showing that the non-adiabatic electronic effects should be taken into account in these types of simulations. Our method can complement the adiabatic molecular dynamics methods that include these effects via a friction term in the equations of motion of the ions. For this purpose, our method can be used to compile a database of the electronic stopping power as a function of velocity and impact parameter for various projectiles and target materials that can be used in these computationally more efficient adiabatic methods.

Appendix A

Supplementary material of chapter 5.

1 Pseudopotentials

The pseudopotentials were generated using the Troullier-Martins scheme [114] for the electronic configurations mentioned below. The numbers in parenthesis are the cutoff radii (in Bohrs) beyond which the pseudopotentials reproduce the all-electron orbitals and potential. The pseudopotential for Au included scalar relativistic effects. No non-linear core corrections have been taken into account.
Au: $6s^1(2.63), 6p^0(2.77), 5d^{10}(2.63), 5f^0(2.63)$
H: $1s^1(1.33), 2p^0(1.33), 3d^0(0.37), 4f^0(1.33)$
He: $1s^2(1.14), 2p^0(1.14), 3d^0(1.14), 4f^0(1.14)$

2 Basis set details and tests

The parameters used for the generation of the basis sets used are as follows:
H:
DZP: $1s(6.0, 2.56; 50.0, 5.0), 2p(6.0; 1000.0, 0.0)$
TZP: $1s(6.0, 3.8, 1.9; 50.0, 5.5), 2p(6.0; 1000.0, 0.0)$
He:
DZP:$1s(8.0, 3.0), 2p(8.0; 50.0, 0.0)$

TZP: $1s(8.0, 2.0, 3.0), 2p(8.0; 50.0, 0.0)$

TZDP: $1s(8.0, 2.0, 3.0), 2p(8.0, 2.0; 50.0, 0.0)$

Au:

DZP: $6s(6.5, 5.7; 30.0, 5.6), 6p(6.5; 10.0, 2.3), 5d(6.0, 3.9)$

Where DZP, TZP and TZDP stand for double-ζ polarized, triple-ζ polarized and triple-ζ doubly polarized basis sets. In parenthesis, the first number (or the first two or three numbers separated by a comma) is the cutoff radius (radii) of the radial function of the first, second and third-ζ orbitals. The last two numbers after semicolon, if present, are V_0 and r_i that determine a soft confinement potential of the form $V(r) = V_0 \frac{e^{-\frac{r_c - r_i}{r - r_i}}}{r_c - r}$, used for continuity of higher derivatives of the radial dependence of the orbital at its cutoff radius r_c [113]. Results of convergence tests are summarized in Tables I, II and III, and in Figure 1.

E_c (Ry)	250	300	350	400
S_H (eV/Å)	6.417	6.417	6.417	6.417
S_{He} (eV/Å)	13.189	13.189	13.189	13.189

Table 1: Effect of the fineness of the real-space grid on the electronic stopping power for projectile velocity $v = 0.50$ a.u. E_c is the mesh cutoff [45]. All other parameters are as stated in the main chapter, chapter 5.

Grid	3x3x2	3x3x3	4x4x2	4x4x3	4x4x4
S_H (eV/Å)	6.480	6.454	6.465	6.470	6.471
S_{He} (eV/Å)	13.199	13.221	13.189	13.161	13.162

Table 2: Effect of the fineness of the k-space grid on the electronic stopping power for projectile velocity v=0.50 a.u. The grid is specified according to Ref. [119]. All other parameters are as stated in the main chapter, chapter 5.

	v (a.u.)	DZP	TZP	TZDP
S_H (eV/Å)	0.08	0.187	0.191	
	0.10	0.269	0.283	
	0.50	6.334	6.870	
S_{He} (eV/Å)	0.08	0.769	0.802	0.849
	0.10	1.126	1.168	1.172
	0.50	13.005	13.204	13.699

Table 3: Basis set convergence: Effect of the projectile basis size on the electronic stopping power. All other parameters are the same as stated in the main chapter, chapter 5.

References

[1] J. F. Ziegler, J. P. Biersack, and M. D. Ziegler. *SRIM - The Stopping and Range of Ions in Matter*. SRIM Co., 2008. (Page 4).

[2] M. W. Finnis, P. Agnew, and A. J. E. Foreman. "Thermal excitation of electrons in energetic displacement cascades". In: *Phys. Rev. B* 44 (2 1991), pp. 567–574. (Page 4).

[3] A. Caro and M. Victoria. "Ion-electron interaction in molecular-dynamics cascades". In: *Phys. Rev. A* 40 (5 1989), pp. 2287–2291. (Page 4).

[4] D. M. Duffy and A. M. Rutherford. "Including the effects of electronic stopping and electron-ion interactions in radiation damage simulations". In: *Journal of Physics: Condensed Matter* 19.1 (2007), p. 016207. (Pages 4, 76, 79).

[5] A. M. Rutherford and D. M. Duffy. "The effect of electron-ion interactions on radiation damage simulations". In: *Journal of Physics: Condensed Matter* 19.49 (2007), p. 496201. (Pages 4, 76, 79).

[6] D. M. Duffy, N. Itoh, A. M. Rutherford, and A. M. Stoneham. "Making tracks in metals". In: *Journal of Physics: Condensed Matter* 20.8 (2008), p. 082201. (Pages 4, 76, 79).

[7] D. M. Duffy and A. M. Rutherford. “Including electronic effects in damage cascade simulations”. In: *Journal of Nuclear Materials* 386-388.0 (2009), pp. 19 –21. (Pages 4, 76, 79).

[8] D. M. Duffy, S. Khakshouri, and A. M. Rutherford. “Electronic effects in radiation damage simulations”. In: *Nuclear Instruments and Methods in Physics Research Section B: Beam Interactions with Materials and Atoms* 267.18 (2009), pp. 3050 –3054. (Pages 4, 76, 79).

[9] A. P. Sutton, T. N. Todorov, M. J. Cawkwell, and J. Hoekstra. “A simple model of atomic interactions in noble metals based explicitly on electronic structure”. In: *Philosophical Magazine A* 81.7 (2001), pp. 1833–1848. (Pages 4, 17).

[10] T. N. Todorov. “Time-dependent tight binding”. In: *Journal of Physics: Condensed Matter* 13.45 (2001), p. 10125. (Pages 4, 17).

[11] C. P. Race, D. R. Mason, and A. P. Sutton. “Electronic excitations and their effect on the interionic forces in simulations of radiation damage in metals”. In: *Journal of Physics: Condensed Matter* 21.11 (2009), p. 115702. (Pages 4, 17).

[12] J. le Page, D. R. Mason, C. P. Race, and W. M. C. Foulkes. “How good is damped molecular dynamics as a method to simulate radiation damage in metals?” In: *New Journal of Physics* 11.1 (2009), p. 013004. (Pages 4, 17).

[13] C. P. Race, D. R. Mason, M. W. Finnis, W. M. C. Foulkes, A. P. Horsfield, and A. P. Sutton. “The treatment of electronic excitations in atomistic

models of radiation damage in metals". In: *Reports on Progress in Physics* 73.11 (2010), p. 116501. (Pages 4, 17, 34).

[14] D. R. Mason, J. le Page, C. P. Race, W. M. C. Foulkes, M. W. Finnis, and A. P. Sutton. "Electronic damping of atomic dynamics in irradiation damage of metals". In: *Journal of Physics: Condensed Matter* 19.43 (2007), p. 436209. (Pages 4, 17).

[15] D. R. Mason, C. P. Race, M. H. F. Foo, A. P. Horsfield, W. M. C. Foulkes, and A. P. Sutton. "Resonant charging and stopping power of slow channelling atoms in a crystalline metal". In: *New Journal of Physics* 14.7 (2012), p. 073009. (Pages 4, 17).

[16] C. P. Race, D. R. Mason, M. H. F. Foo, W. M. C. Foulkes, A. P. Horsfield, and A. P. Sutton. "Quantum-Classical simulations of the electronic stopping force and charge on slow heavy channelling ions in metals". In: *Journal of Physics: Condensed Matter* 25.12 (2013), p. 125501. (Pages 4, 17).

[17] J. E. Valdés, P. Vargas, and N. R. Arista. "Electronic energy loss of slow protons channeled in metals". In: *Phys. Rev. A* 56 (6 1997), pp. 4781–4785. (Pages 5, 6, 17, 35).

[18] P. Echenique, R. Nieminen, and R. Ritchie. "Density functional calculation of stopping power of an electron gas for slow ions". In: *Solid State Communications* 37.10 (1981), pp. 779 –781. (Pages ix, xi, xii, 5–7, 16, 34, 38, 40, 41, 45, 48, 55, 56).

[19] P. M. Echenique, R. M. Nieminen, J. C. Ashley, and R. H. Ritchie. “Nonlinear stopping power of an electron gas for slow ions”. In: *Phys. Rev. A* 33 (2 1986), pp. 897–904. (Pages 5, 16).

[20] S. N. Markin, D. Primetzhofer, M. Spitz, and P. Bauer. “Electronic stopping of low-energy H and He in Cu and Au investigated by time-of-flight low-energy ion scattering”. In: *Phys. Rev. B* 80 (20 2009), p. 205105. (Pages ix, x, 6, 34–37).

[21] S. N. Markin, D. Primetzhofer, S. Prusa, M. Brunmayr, G. Kowarik, F. Aumayr, and P. Bauer. “Electronic interaction of very slow light ions in Au: Electronic stopping and electron emission”. In: *Phys. Rev. B* 78 (19 2008), p. 195122. (Pages ix–xi, 6, 34–37, 40, 41).

[22] J. E. Valdés, G. Martínez-Tamayo, G. H. Lantschner, J. C. Eckardt, and N. R. Arista. “Electronic energy loss of low velocity H+ beams in Al, Ag, Sb, Au and Bi”. In: *Nuclear Instruments and Methods in Physics Research Section B: Beam Interactions with Materials and Atoms* 73.3 (1993), pp. 313 –318. (Pages 5, 6, 17, 34, 35).

[23] G. Martínez-Tamayo, J. C. Eckardt, G. H. Lantschner, and N. R. Arista. “Energy loss of H^+ and He^+ in Al, Zn, and Au in the very low- to intermediate-energy range”. In: *Phys. Rev. A* 54 (4 1996), pp. 3131–3138. (Pages 5, 34).

[24] M. Quijada, A. G. Borisov, I. Nagy, R. D. Muiño, and P. M. Echenique. “Time-dependent density-functional calculation of the stopping power for protons and antiprotons in metals”. In: *Phys. Rev. A* 75 (4 2007), p. 042902. (Pages 6, 34).

[25] P. Echenique, F. Flores, and R. Ritchie. "Dynamic Screening of Ions in Condensed Matter". In: ed. by H. Ehrenreich and D. Turnbull. Vol. 43. Solid State Physics. Academic Press, 1990, pp. 229 –308. (Pages 6, 7, 34, 35).

[26] R. Hatcher, M. Beck, A. Tackett, and S. T. Pantelides. "Dynamical Effects in the Interaction of Ion Beams with Solids". In: *Phys. Rev. Lett.* 100 (10 2008), p. 103201. (Pages 6, 35).

[27] J. E. Valdés, J. C. Eckardt, G. H. Lantschner, and N. R. Arista. "Energy loss of slow protons in solids: Deviation from the proportionality with projectile velocity". In: *Phys. Rev. A* 49 (2 1994), pp. 1083–1088. (Pages 6, 17, 35, 37).

[28] P. Vargas, J. E. Valdés, and N. R. Arista. "Energy loss of slow protons channeled in Au". In: *Phys. Rev. A* 53 (3 1996), pp. 1638–1643. (Pages 6, 17, 35).

[29] J. M. Pruneda, D. Sánchez-Portal, A. Arnau, J. I. Juaristi, and E. Artacho. "Electronic Stopping Power in LiF from First Principles". In: *Phys. Rev. Lett.* 99 (23 2007), p. 235501. (Pages xii, 6–9, 18, 35, 45, 58–61).

[30] E. D. Cantero, G. H. Lantschner, J. C. Eckardt, and N. R. Arista. "Velocity dependence of the energy loss of very slow proton and deuteron beams in Cu and Ag". In: *Phys. Rev. A* 80 (3 2009), p. 032904. (Pages 6, 17, 34, 35).

[31] R. Blume, W. Eckstein, H. Verbeek, and K. Reichelt. "Electronic energy loss of H, D and He in single crystal gold films in the energy range below

15 keV". In: *Nuclear Instruments and Methods in Physics Research* 194 (1982), pp. 67 –70. (Pages 6, 35).

[32] E. A. Figueroa, E. D. Cantero, J. C. Eckardt, G. H. Lantschner, J. E. Valdés, and N. R. Arista. "Threshold effect in the energy loss of slow protons and deuterons channeled in Au crystals". In: *Phys. Rev. A* 75 (1 2007), p. 010901. (Pages x, 6, 17, 34–37).

[33] D. Primetzhofer, S. Rund, D. Roth, D. Goebl, and P. Bauer. "Electronic Excitations of Slow Ions in a Free Electron Gas Metal: Evidence for Charge Exchange Effects". In: *Phys. Rev. Lett.* 107 (16 2011), p. 163201. (Pages xi, 6, 14, 43, 45, 46).

[34] E. Artacho. "Electronic stopping in insulators: a simple model". In: *Journal of Physics: Condensed Matter* 19.27 (2007), p. 275211. (Pages 7, 58, 80).

[35] D. Semrad. "Coulomb effect and threshold effect in electronic stopping power for slow protons". In: *Phys. Rev. A* 33 (3 1986), pp. 1646–1652. (Page 7).

[36] B. Solleder, L. Wirtz, and J. Burgdörfer. "Vanishing gap in LiF for electronic excitations by slow antiprotons". In: *Phys. Rev. B* 79 (12 2009), p. 125107. (Page 7).

[37] K. Eder, D. Semrad, P. Bauer, R. Golser, P. Maier-Komor, F. Aumayr, M. Peñalba, A. Arnau, J. M. Ugalde, and P. M. Echenique. "Absence of a "Threshold Effect" in the Energy Loss of Slow Protons Traversing Large-Band-Gap Insulators". In: *Phys. Rev. Lett.* 79 (21 1997), pp. 4112–4115. (Pages xiii, 7, 58, 71, 72).

[38] J. I. Juaristi, C. Auth, H. Winter, A. Arnau, K. Eder, D. Semrad, F. Aumayr, P. Bauer, and P. M. Echenique. “Unexpected Behavior of the Stopping of Slow Ions in Ionic Crystals”. In: *Phys. Rev. Lett.* 84 (10 2000), pp. 2124–2127. (Pages 7, 58).

[39] S. P. Møller, A. Csete, T. Ichioka, H. Knudsen, U. I. Uggerhøj, and H. H. Andersen. “Stopping Power in Insulators and Metals without Charge Exchange”. In: *Phys. Rev. Lett.* 93 (4 2004), p. 042502. (Pages 7, 58).

[40] C. Auth, A. Mertens, H. Winter, and A. Borisov. “Threshold in the Stopping of Slow Protons Scattered from the Surface of a Wide-Band-Gap Insulator”. In: *Phys. Rev. Lett.* 81 (22 1998), pp. 4831–4834. (Pages 7, 58).

[41] M. Draxler, S. P. Chenakin, S. N. Markin, and P. Bauer. “Apparent Velocity Threshold in the Electronic Stopping of Slow Hydrogen Ions in LiF”. In: *Phys. Rev. Lett.* 95 (11 2005), p. 113201. (Pages xii, xiii, 7, 18, 58, 60, 61).

[42] S. N. Markin, D. Primetzhofer, and P. Bauer. “Vanishing Electronic Energy Loss of Very Slow Light Ions in Insulators with Large Band Gaps”. In: *Phys. Rev. Lett.* 103 (11 2009), p. 113201. (Pages xii, xiii, 7, 58–63, 71).

[43] N. Shenvi, S. Roy, and J. C. Tully. “Dynamical Steering and Electronic Excitation in NO Scattering from a Gold Surface”. In: *Science* 326.5954 (2009), pp. 829–832. (Page 8).

[44] P. Ordejón, E. Artacho, and J. M. Soler. "Self-consistent order-N density-functional calculations for very large systems". In: *Phys. Rev. B* 53 (16 1996), R10441–R10444. (Pages 8, 25, 26, 44, 49, 59, 67).

[45] J. M. Soler, E. Artacho, J. D. Gale, A. García, J. Junquera, P. Ordejón, and D. Sánchez-Portal. "The SIESTA method for ab initio order-N materials simulation". In: *Journal of Physics: Condensed Matter* 14.11 (2002), p. 2745. (Pages 8, 18, 25, 26, 36, 44, 49, 59, 67, 85).

[46] A. Tsolakidis, D. Sánchez-Portal, and R. M. Martin. "Calculation of the optical response of atomic clusters using time-dependent density functional theory and local orbitals". In: *Phys. Rev. B* 66 (23 2002), p. 235416. (Pages 8, 18, 25).

[47] M. A. Zeb, J. Kohanoff, D. Sánchez-Portal, A. Arnau, J. I. Juaristi, and E. Artacho. "Electronic Stopping Power in Gold: The Role of d Electrons and the H/He Anomaly". In: *Phys. Rev. Lett.* 108 (22 2012), p. 225504. (Pages 8, 43).

[48] M. A. Zeb, J. Kohanoff, D. Sánchez-Portal, and E. Artacho. "Electronic stopping power of H and He in Al and LiF from first principles". In: *Nuclear Instruments and Methods in Physics Research Section B: Beam Interactions with Materials and Atoms* 303.0 (2013), pp. 59 –61. (Page 8).

[49] N. Bohr. "Scattering and Stopping of Fission Fragments". In: *Phys. Rev.* 58 (7 1940), pp. 654–655. (Page 10).

[50] N. Bohr. "Velocity-Range Relation for Fission Fragments". In: *Phys. Rev.* 59 (3 1941), pp. 270–275. (Page 10).

[51] L. C. Northcliffe. “Energy Loss and Effective Charge of Heavy Ions in Aluminum”. In: *Phys. Rev.* 120 (5 1960), pp. 1744–1757. (Page 10).

[52] N. Bohr. “II. On the theory of the decrease of velocity of moving electrified particles on passing through matter”. In: *Philosophical Magazine Series 6* 25.145 (1913), pp. 10–31. (Page 10).

[53] N. Bohr. “LX. On the decrease of velocity of swiftly moving electrified particles in passing through matter”. In: *Philosophical Magazine Series 6* 30.178 (1915), pp. 581–612. (Page 10).

[54] N. Bohr and H. Lutz. “9. Interactions of Particles with Solids”. In: *Atomic and Electron Physics Atomic Interactions.* Ed. by B. Bederson and W. L. Fite. Vol. 7, Part B. Methods in Experimental Physics. Academic Press, 1968, pp. 231 –305. (Page 10).

[55] H. Bethe. “Zur Theorie des Durchgangs schneller Korpuskularstrahlen durch Materie”. In: *Annalen der Physik* 397 (3 1930), p. 325. (Pages 12, 15).

[56] H. Bethe. “Bremsformel für Elektronen relativistischer Geschwindigkeit”. German. In: *Zeitschrift für Physik* 76.5-6 (1932), pp. 293–299. (Page 12).

[57] H. Bethe and J. Ashkin. *In Experimental Nuclear Physics.* Wiley, New York, 1953-59. (Page 12).

[58] C. Møller. “Zur Theorie des Durchgangs schneller Elektronen durch Materie”. In: *Annalen der Physik* 406.5 (1932), pp. 531–585. (Page 12).

[59] F. Bloch. “Zur Bremsung rasch bewegter Teilchen beim Durchgang durch Materie”. In: *Annalen der Physik* 408.3 (1933), pp. 285–320. (Page 12).

[60] F. Bloch. “Bremsvermögen von Atomen mit mehreren Elektronen”. German. In: *Zeitschrift für Physik* 81.5-6 (1933), pp. 363–376. (Page 12).

[61] U. Fano. “Ionization Yield of Radiations. II. The Fluctuations of the Number of Ions”. In: *Phys. Rev.* 72 (1 1947), pp. 26–29. (Page 12).

[62] U. Fano. “Differential Inelastic Scattering of Relativistic Charged Particles”. In: *Phys. Rev.* 102 (2 1956), pp. 385–387. (Page 12).

[63] U. Fano. “Atomic Theory of Electromagnetic Interactions in Dense Materials”. In: *Phys. Rev.* 103 (5 1956), pp. 1202–1218. (Page 12).

[64] U. Fano. “Penetration of Protons, Alpha Particles, and Mesons”. In: *Annual Review of Nuclear Science* 13.1 (1963), pp. 1–66. (Page 12).

[65] L. C. Northcliffe and R. F. Schilling. “Range and stopping-power tables for heavy ions”. In: *Atomic Data and Nuclear Data Tables* 7.34 (1970), pp. 233 –463. (Page 12).

[66] M. Inojuti. “Inelastic Collisions of Fast Charged Particles with Atoms and Molecules - The Bethe Theory Revisited”. In: *Rev. Mod. Phys.* 43 (3 1971), pp. 297–347. (Page 12).

[67] W. H. Barkas, J. N. Dyer, and H. H. Heckman. “Resolution of the Σ^--Mass Anomaly”. In: *Phys. Rev. Lett.* 11 (1 1963), pp. 26–28. (Pages 12, 18).

[68] J. C. Ashley, R. H. Ritchie, and W. Brandt. “Z_1^3 Effect in the Stopping Power of Matter for Charged Particles”. In: *Phys. Rev. B* 5 (7 1972), pp. 2393–2397. (Page 12).

[69] J. D. Jackson and R. L. McCarthy. “z^3 Corrections to Energy Loss and Range”. In: *Phys. Rev. B* 6 (11 1972), pp. 4131–4141. (Page 12).

[70] J. C. Ashley, R. H. Ritchie, and W. Brandt. “Z_1^3-Dependent Stopping Power and Range Contributions”. In: *Phys. Rev. A* 8 (5 1973), pp. 2402–2408. (Page 12).

[71] H. Sørensen and H. H. Andersen. “Stopping Power of Al, Cu, Ag, Au, Pb, and U for 5-18 MeV Protons and Deuterons”. In: *Phys. Rev. B* 8 (5 1973), pp. 1854–1863. (Page 12).

[72] J. C. Ashley. “Influence of the Z_1^3 contribution to stopping power on the evaluation of mean excitation potentials and shell corrections”. In: *Phys. Rev. B* 9 (1 1974), pp. 334–336. (Page 12).

[73] J. C. Ashley, R. H. Ritchie, and W. Brandt. “Z_1^3-dependent range contributions”. In: *Phys. Rev. A* 10 (2 1974), pp. 737–737. (Page 12).

[74] H. H. Andersen, J. F. Bak, H. Knudsen, and B. R. Nielsen. “Stopping power of Al, Cu, Ag, and Au for MeV hydrogen, helium, and lithium ions. Z_1^3 and Z_1^4 proportional deviations from the Bethe formula”. In: *Phys. Rev. A* 16 (5 1977), pp. 1929–1940. (Pages 12, 18).

[75] J. M. Pitarke, R. H. Ritchie, and P. M. Echenique. “Quadratic response theory of the energy loss of charged particles in an electron gas”. In: *Phys. Rev. B* 52 (19 1995), pp. 13883–13902. (Page 12).

[76] P. Sigmund and A. Schinner. “Effective charge and related/unrelated quantities in heavy-ion stopping”. In: *Nuclear Instruments and Methods in*

Physics Research Section B: Beam Interactions with Materials and Atoms 174.4 (2001), pp. 535 –540. (Page 12).

[77] P. Sigmund and A. Schinner. “Binary theory of antiproton stopping”. English. In: *The European Physical Journal D - Atomic, Molecular, Optical and Plasma Physics* 15.2 (2001), pp. 165–172. (Page 12).

[78] H. Bichsel. *American Institute of Physics Handbook*. McGraw-Hill, New York, 1972, pp. 8–142. (Page 12).

[79] P. Sigmund. *Radiation Damage Processes in Materials*. Noordhoff, Leiden, 1975. (Page 12).

[80] S. P. Ahlen. “Theoretical and experimental aspects of the energy loss of relativistic heavily ionizing particles”. In: *Rev. Mod. Phys.* 52 (1 1980), pp. 121–173. (Pages 12, 13).

[81] P. Sigmund and A. Schinner. “Binary stopping theory for swift heavy ions”. In: *Eur. Phys. J. D.* 12 (2000), p. 425. (Page 12).

[82] P. Sigmund. “Shell correction in Bohr stopping theory”. English. In: *The European Physical Journal D - Atomic, Molecular, Optical and Plasma Physics* 12.1 (2000), pp. 111–116. (Page 12).

[83] P. Sigmund and A. Schinner. “Barkas effect, shell correction, screening and correlation in collisional energy-loss straggling of an ion beam”. In: *Eur. Phys. J. D* 23 (2003), pp. 201–209. (Page 12).

[84] P. Sigmund. “Charge-dependent electronic stopping of swift nonrelativistic heavy ions”. In: *Phys. Rev. A* 56 (5 1997), pp. 3781–3793. (Page 12).

[85] E. Uggerhøj. "Some Energy-Loss and Channeling Phenomena for GeV Particles". In: *Physica Scripta* 28.3 (1983), p. 331. (Page 12).

[86] J. R. Sabin and J. Oddershede. "Shell corrections to electronic stopping powers from orbital mean excitation energies". In: *Phys. Rev. A* 26 (6 1982), pp. 3209–3219. (Page 12).

[87] J. Oddershede and J. R. Sabin. "Orbital and whole-atom proton stopping power and shell corrections for atoms with Z≤ 36". In: *Atomic Data and Nuclear Data Tables* 31.2 (1984), pp. 275 –297. (Page 12).

[88] H. Bichsel. "Shell corrections in stopping powers". In: *Phys. Rev. A* 65 (5 2002), p. 052709. (Page 12).

[89] C. Amsler et al. "Review of Particle Physics". In: *Physics Letters B* 667 (2008), pp. 1 –6. (Page 12).

[90] J. Beringer et al. "Review of Particle Physics, **30** Passage of particles through matter". In: *Phys. Rev. D* 86 (1 2012), p. 010001. (Page 12).

[91] J. F. Ziegler. "The Stopping of Energetic Light Ions in Elemental Matter". In: *J. Appl. Phys* 85 (1999), p. 1249. (Pages 13, 18).

[92] P. Sigmund. *Stopping of Swift Ions: Solved and Unsolved Problems.* Royal Danish Academy of Sciences and Letters, 2006, p. 557. (Page 13).

[93] J. Lindhard and M. Scharff. "Energy Dissipation by Ions in the kev Region". In: *Phys. Rev.* 124 (1 1961), pp. 128–130. (Page 14).

[94] B. A. Trubnikov and Y. N. Yavlinskii. "Energy Loss of Slow Protons in Metals". In: *Sov. Phys. JETP* 21 (1965), p. 167. (Page 14).

[95] I. S. Tilinin. "Quasiclassical expression for inelastic energy losses in atomic particle collisions below the Bohr velocity". In: *Phys. Rev. A* 51 (4 1995), pp. 3058–3065. (Page 14).

[96] E. Fermi and E. Teller. "The Capture of Negative Mesotrons in Matter". In: *Phys. Rev.* 72 (5 1947), pp. 399–408. (Page 14).

[97] E. Fermi. "Über die Theorie des Stoßes zwischen Atomen und elektrisch geladenen Teilchen". In: *Zeitschrift für Physik* 29.1 (1924), pp. 315–327. (Page 14).

[98] J. Lindhard. "On the properties of a gas of charged particles". In: *Dan. Mat. Fys. Medd.* 28 (8 1954). (Pages 14, 15).

[99] R. H. Ritchie. "Interaction of Charged Particles with a Degenerate Fermi-Dirac Electron Gas". In: *Phys. Rev.* 114 (3 1959), pp. 644–654. (Page 15).

[100] J. Finneman. PhD dissertation. The Institute of Physics, Aarhus University. 1968. (Page 16).

[101] T. L. Ferrell and R. H. Ritchie. "Energy losses by slow ions and atoms to electronic excitation in solids". In: *Phys. Rev. B* 16 (1 1977), pp. 115–123. (Pages 16, 56).

[102] F. Calogero. *Variable Phase Approach to Potential Scattering.* Academic, New York, 1967. (Page 16).

[103] J. Friedel. "XIV. The distribution of electrons round impurities in monovalent metals". In: *Philosophical Magazine Series 7* 43.337 (1952), pp. 153–189. (Page 16).

[104] Z. D. Popovic and M. J. Stott. “Nonlinear, Self-Consistent Theory of Proton Screening in Metals Applied to Hydrogen in Al and Mg”. In: *Phys. Rev. Lett.* 33 (19 1974), pp. 1164–1167. (Page 16).

[105] C. O. Almbladh, U. von Barth, Z. D. Popovic, and M. J. Stott. “Screening of a proton in an electron gas”. In: *Phys. Rev. B* 14 (6 1976), pp. 2250–2254. (Page 16).

[106] C. Celedón, N. Arista, J. Valdís, and P. Vargas. “Threshold effect in the energy loss of hydrogen and helium ions transmitted in channeling conditions in gold single crystal”. In: *Microelectronics Journal* 39.11 (2008), pp. 1358 –1359. (Pages 17, 34, 35).

[107] E. A. Figueroa, E. D. Cantero, J. C. Eckardt, G. H. Lantschner, and N. R. Arista. “Threshold effect in the energy-loss straggling of protons channeled in Au [100] at very low velocities”. In: *Phys. Rev. A* 75 (6 2007), p. 064902. (Pages x, 17, 34–37).

[108] E. A. Figueroa and N. R. Arista. “The screening and stopping coefficients of slow light ions”. In: *Journal of Physics: Condensed Matter* 22.1 (2010), p. 015602. (Page 17).

[109] W. M. C. Foulkes and R. Haydock. “Tight-binding models and density-functional theory”. In: *Phys. Rev. B* 39 (17 1989), pp. 12520–12536. (Page 17).

[110] A. P. Sutton, M. W. Finnis, D. G. Pettifor, and Y. Ohta. “The tight-binding bond model”. In: *Journal of Physics C: Solid State Physics* 21.1 (1988), p. 35. (Page 17).

[111] E. Runge and E. K. U. Gross. “Density-Functional Theory for Time-Dependent Systems”. In: *Phys. Rev. Lett.* 52 (12 1984), pp. 997–1000. (Page 17).

[112] J. K. Tomfohr and O. F. Sankey. In: *Phys. Status Solidi (b)* 226 (2001), p. 115. (Pages 23, 24).

[113] J. Junquera, O. Paz, D. Sánchez-Portal, and E. Artacho. “Numerical atomic orbitals for linear-scaling calculations”. In: *Phys. Rev. B* 64 (23 2001), p. 235111. (Pages 26, 85).

[114] N. Troullier and J. L. Martins. “Efficient pseudopotentials for plane-wave calculations. II. Operators for fast iterative diagonalization”. In: *Phys. Rev. B* 43 (11 1991), pp. 8861–8869. (Pages 26, 84).

[115] R. H. Ritchie. “Interaction of Charged Particles with a Degenerate Fermi-Dirac Electron Gas”. In: *Phys. Rev.* 114 (3 1959), pp. 644–654. (Page 34).

[116] M. Kitagawa and Y. H. Ohtsuki. “Inelastic scattering of slow ions in channeling”. In: *Phys. Rev. B* 9 (11 1974), pp. 4719–4723. (Page 34).

[117] R. Blume, W. Eckstein, and H. Verbeek. “Electronic energy loss of H, D and He in Au below 20 keV”. In: *Nuclear Instruments and Methods* 168 (1980), pp. 57 –62. (Page 35).

[118] J. P. Perdew, K. Burke, and M. Ernzerhof. “Generalized Gradient Approximation Made Simple”. In: *Phys. Rev. Lett.* 77 (18 1996), pp. 3865–3868. (Page 35).

[119] H. J. Monkhorst and J. D. Pack. “Special points for Brillouin-zone integrations”. In: *Phys. Rev. B* 13 (12 1976), pp. 5188–5192. (Pages 36, 85).

[120] A. A. Correa, J. Kohanoff, E. Artacho, D. Sánchez-Portal, and A. Caro. “Nonadiabatic Forces in Ion-Solid Interactions: The Initial Stages of Radiation Damage”. In: *Phys. Rev. Lett.* 108 (21 2012), p. 213201. (Page 43).

[121] A. A. Correa, J. Kohanoff, E. Artacho, D. Sanchez-Portal, and A. Caro. “Erratum: Nonadiabatic Forces in Ion-Solid Interactions: The Initial Stages of Radiation Damage [Phys. Rev. Lett. 108, 213201 (2012)]”. In: *Phys. Rev. Lett.* 109 (6 2012), p. 069901. (Page 43).

[122] D. M. Ceperley and B. J. Alder. “Ground State of the Electron Gas by a Stochastic Method”. In: *Phys. Rev. Lett.* 45 (7 1980), pp. 566–569. (Pages 43, 49, 59, 67).

[123] J. P. Perdew and A. Zunger. “Self-interaction correction to density-functional approximations for many-electron systems”. In: *Phys. Rev. B* 23 (10 1981), pp. 5048–5079. (Pages 43, 49, 59, 67).

[124] D. Isaacson. *Compilation of r_s Values.* National Auxiliary Publication Service, New York, 1975. (Page 45).

[125] J. M. Peek. “Free-electron-gas approximation for the stopping power of ionic targets”. In: *Phys. Rev. A* 26 (2 1982), pp. 1030–1034. (Page 48).

[126] Y. Chen, D. Li, G. Wang, L. Lin, S. Oak, G. Shrivastav, A. Tasch, and S. Banerjee. “Quantum Mechanical Model of Electronic Stopping Power for Ions in a Free Electron Gas”. English. In: *Journal of Computational Electronics* 1.1-2 (2002), pp. 241–245. (Page 48).

[127] C. Yang, D. Li, G. Wang, L. Lin, A. Tasch, and S. Banerjee. “Quantum mechanical model of electronic stopping power for ions in a free electron

gas". In: *Ion Implantation Technology. 2002. Proceedings of the 14th International Conference on*. 2002, pp. 556–559. (Page 48).

[128] N.-p. Wang and I. Nagy. "Electronic energy loss of helium ions in aluminum". In: *Phys. Rev. A* 55 (3 1997), pp. 2083–2086. (Page 48).

[129] N.-p. Wang and I. Nagy. "Nonlinear calculations of the stopping power for slow hydrogen and helium projectiles in solids". In: *Phys. Rev. A* 56 (6 1997), pp. 4795–4798. (Page 48).

[130] M. Bergsmann, P. Hörlsberger, F. Kastner, and P. Bauer. "Electronic stopping power of protons and He ions in a dilute electron gas of a metal". In: *Phys. Rev. B* 58 (9 1998), pp. 5139–5142. (Page 48).

[131] D. G. Arbó, M. S. Gravielle, and J. E. Miraglia. "Second-order Born collisional stopping of ions in a free-electron gas". In: *Phys. Rev. A* 62 (3 2000), p. 032901. (Page 48).

[132] E. Wigner and F. Seitz. "On the Constitution of Metallic Sodium". In: *Phys. Rev.* 43 (10 1933), pp. 804–810. (Page 48).

[133] E. Wigner and F. Seitz. "On the Constitution of Metallic Sodium. II". In: *Phys. Rev.* 46 (6 1934), pp. 509–524. (Page 48).

[134] J. C. Slater. "Electronic Energy Bands in Metals". In: *Phys. Rev.* 45 (11 1934), pp. 794–801. (Page 48).

[135] J. Bardeen. "An Improved Calculation of the Energies of Metallic Li and Na". In: *J. Chem. Phys.* 6 (1938), p. 367. (Page 48).

[136] W. Jiang, Y. Zhang, and W. J. Weber. “Temperature dependence of disorder accumulation and amorphization in Au-ion-irradiated $6H - SiC$”. In: *Phys. Rev. B* 70 (16 2004), p. 165208. (Pages 66, 77).

[137] Y. Zhang, W. J. Weber, and C. M. Wang. “Electronic stopping powers in silicon carbide”. In: *Phys. Rev. B* 69 (20 2004), p. 205201. (Pages 66, 77).

[138] L. Levien, C. T. Prewitt, and D. J. Weidner. “Structure and elastic properties of quartz at pressure P = 1 atm”. In: *American Mineralogist'* 65 (1980), pp. 920–930. (Page 68).

[139] S. Sasaki, K. Fujino, and Y. Takeuchi. “X-ray determination of electron-density distributions in oxides, MgO, MnO, CoO, and NiO, and atomic scattering factors of their constituent atoms”. In: *Proceedings of the Japan Academy* 55 (1979), pp. 43–48. (Page 70).

[140] E. N. Maslen, V. A. Streltsov, N. R. Streltsova, N. Ishizawa, and Y. Satow. “Synchrotron X-ray study of the electron density in α-Al_2O_3”. In: *Acta Crystallographica Section B* 49.6 (1993), pp. 973–980. (Page 70).

[141] P. Bauer, R. Golser, D. Semrad, P. Maier-Komor, F. Aumayr, and A. Arnau. “Influence of the chemical state on the stopping of protons and He-ions in some oxides”. In: *Nuclear Instruments and Methods in Physics Research Section B: Beam Interactions with Materials and Atoms* 136.0 (1998), pp. 103 –108. (Pages xiii, 71, 72).

[142] A. V. Wijngaarden and H. E. Duckworth. “Energy loss in condensed matter of H^1 and He^4 in the energy range $4 < E < 30$ KeV”. In: *Canadian Journal of Physics* 40.12 (1962), pp. 1749–1764. (Pages xiii, 72).

[143] P. Bauer, W. Rossler, and P. Mertens. “Stopping of hydrogen ions in oxides: influence of the chemical bond”. In: *Nuclear Instruments and Methods in Physics Research Section B: Beam Interactions with Materials and Atoms* 69.1 (1992), pp. 46 –52. (Pages xiii, 72).

[144] J. I. Juaristi, M. Alducin, R. D. Muiño, H. F. Busnengo, and A. Salin. “Role of Electron-Hole Pair Excitations in the Dissociative Adsorption of Diatomic Molecules on Metal Surfaces”. In: *Phys. Rev. Lett.* 100 (11 2008), p. 116102. (Page 74).

[145] L. Martin-Gondre, M. Alducin, G. A. Bocan, R. D. Muiño, and J. I. Juaristi. “Competition between Electron and Phonon Excitations in the Scattering of Nitrogen Atoms and Molecules off Tungsten and Silver Metal Surfaces”. In: *Phys. Rev. Lett.* 108 (9 2012), p. 096101. (Page 74).

[146] H. Winter, J. I. Juaristi, I. Nagy, A. Arnau, and P. M. Echenique. “Energy loss of slow ions in a nonuniform electron gas”. In: *Phys. Rev. B* 67 (24 2003), p. 245401. (Page 74).

[147] L. Nasdala, J. M. Hanchar, A. Kronz, and M. J. Whitehouse. “Long-term stability of alpha particle damage in natural zircon”. In: *Chemical Geology* 220.1-2 (2005), pp. 83 –103. (Page 75).

[148] W. J. W. Ian Farnan Herman Cho. “Quantification of actinide alpha-adiation damage in minerals and ceramics”. In: *Nature* 7124 (2007), 190193. (Page 75).

[149] Z. Mursic, T. Vogt, and F. Frey. “High-temperature neutron powder diffraction study of ZrSiO up to 1900 K”. In: *Supplement to Acta Cryst. B* 48 (1992), 584590. (Page 75).

[150] L. L. Snead, T. Nozawa, Y. Katoh, T.-S. Byun, S. Kondo, and D. A. Petti. “Handbook of SiC properties for fuel performance modeling”. In: *Journal of Nuclear Materials* 371.1-3 (2007), pp. 329 –377. (Page 77).

[151] A.-A. F. Tavassoli. “Present limits and improvements of structural materials for fusion reactors - a review”. In: *Journal of Nuclear Materials* 302.2-3 (2002), pp. 73 –88. (Page 77).

[152] Y. Zhang, I.-T. Bae, K. Sun, C. Wang, M. Ishimaru, Z. Zhu, W. Jiang, and W. J. Weber. “Damage profile and ion distribution of slow heavy ions in compounds”. In: *J. Appl. Phys.* 105 (2009), p. 104901. (Page 77).

[153] H. Y. Xiao, Y. Zhang, L. L. Snead, V. Shutthanandan, H. Z. Xue, and W. J. Weber. “Near-surface and bulk behavior of Ag in SiC”. In: *Journal of Nuclear Materials* 420.1-3 (2012), pp. 123 –130. (Page 77).

[154] H. Z. Xue, Y. Zhang, Z. Zhu, W. M. Zhang, I.-T. Bae, and W. J. Weber. “Damage profiles and ion distribution in Pt-irradiated SiC”. In: *Nuclear Instruments and Methods in Physics Research Section B: Beam Interactions with Materials and Atoms* 286.0 (2012), pp. 114 –118. (Page 77).

[155] E. J. Olivier and J. H. Neethling. “The role of Pd in the transport of Ag in SiC”. In: *Journal of Nuclear Materials* 432.1-3 (2013), pp. 252 –260. (Page 77).

[156] A. Taylor and R. M. Jones. *Silicon Carbide - A High Temperature Semiconductor.* Pergamon Press, Oxford, London, New York, Paris, 1960, p. 147. (Page 78).

[157] O. Madelung and L. Brnstein, eds. *Numerical Data and Functional Relationships in Science and Technology, Physics of Group IV Elements and III V Compounds*. Vol. 17. Springer Verlag, Berlin, 1982. (Page 78).

Appendix B

Interplay between spin-orbit coupling and Hubbard interaction in SrIrO3 and related Pbnm perovskites

This work is done under supervision of and in collaboration with H. Y. Kee. It is published in Physical Review B [Phys. Rev. B 86, 085149 (2012)].

ABSTRACT

There has been a rapidly growing interest on the interplay between spin-orbit coupling (SOC) and Hubbard interaction U in correlated materials. A current consensus is that the stronger the SOC, the smaller is the critical interaction U_c required for a spin-orbit Mott insulator, because the atomic SOC splits a band into different total angular momentum bands narrowing the effective bandwidth. It was further claimed that at large enough SOC, the stronger the SOC, the weaker the U_c because in general the effective SOC is enhanced with increasing electron-electron interaction strength. Contrary to this expectation, we find that, in orthorhombic perovskite oxides (Pbnm), the stronger the SOC, the bigger the U_c. This is originated from a line of Dirac node in $J_{eff} = 1/2$ bands near the Fermi level inherited from a combination of the lattice structure and a large SOC. Due to this protected line of nodes, there are small hole and electron pockets in $SrIrO_3$, and such a small density of states makes Hubbard interaction less efficient in building a magnetic insulator. The full phase diagram in U vs. SOC is obtained, where non-magnetic semimetal, magnetic metal, and magnetic insulator are found. Magnetic ordering patterns beyond U_c are also presented. We further discuss implications of our finding in relation to other perovskites such as $SrRhO_3$ and $SrRuO_3$.

INTRODUCTION

Perovskite oxides with the chemical formula AMO_3 where A is a cation and M is a transition metal, exhibit an exceptionally wide range of properties including anomalous Hall effect, colossal magnetoresistance, ferroelectricity, ferromagnetism, and superconductivity. Such an ample variety in a rather simple structure indicates that a detailed balance between charge, spin, structure, and correlation is important in determining the ground state.

In particular, orthorhombic perovskite (point group symmetry, Pbnm) oxides are a large class of anisotropic oxides based on AMO_3 where MO_6 octahedra are distorted from the symmetric cubic structure. Among them, $SrRuO_3$, $SrRhO_3$ and $SrIrO_3$ (called perovskite ruthenates, rhodates, and iridates respectively), display correlated metallic ground states. However, their magnetic properties differ hinting a crucial role of electron interaction. $SrRuO_3$ is a ferromagnetic metal [1–3] and $SrRhO_3$ a metal near a critical point [4–6], while $SrIrO_3$ is a semimetal with an extremely small number of charge carriers without any magnetic moment [7–9]. Given that Ir has 5d orbitals in the outer shell, while Rh and Ru have 4d orbitals, Hubbard interaction is expected to be smaller in iridates [10]. Indeed it was found that the optical gap due to Hubbard interaction is about 0.5eV in Sr_2IrO_4[11], a sister compound of $SrIrO_3$. This leads to a naive conclusion that iridates should be better metal than rhodates or ruthenates, but the reality is the opposite.

What is missing in the above discussion is the SOC. Ir is heavier than Rh and the SOC strength is comparable to Hubbard interaction in iridates [11]. Since the atomic SOC is a local interaction, the electronic energy level splits into different total angular momentum J levels. For example, starting from the atomic limit, five d-orbitals split into t_{2g} and e_g levels due to the octahedral crystal field, and t_{2g} further splits into $J_{eff} = 3/2$ and $J_{eff} = 1/2$ via the SOC when the crystal field splitting is larger than the strength of SOC. Once these bands form, a larger SOC leads to a smaller bandwidth of $J_{eff} = 1/2$ separated from $J_{eff} = 3/2$. Thus, the larger the SOC, the larger the ratio between Hubbard interaction(U) and the bandwidth(W), U/W where W is the bandwidth of $J_{eff} = 1/2$. While the absolute strength of U is smaller in iridates, its effect (given by the ratio U/W) is amplified. This is indeed observed in a layered perovskite, Sr_2IrO_4, dubbed a spin-orbit Mott insulator [12–18]. To explain the metallicity of $SrIrO_3$ compared to insulating Sr_2IrO_4, it was further suggested that $SrIrO_3$ has a larger bandwidth comparing to quasi-two dimensional Sr_2IrO_4 [19, 20]. A growing consensus is that the larger the SOC, the smaller the critical interaction strength U_c that is required for the phase transition from metal to Mott insulator [13, 21]

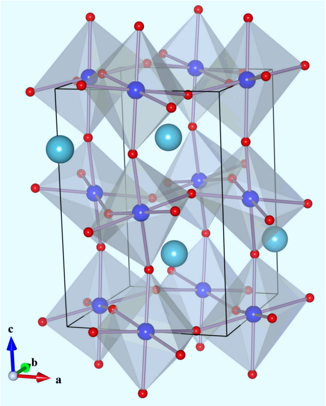

FIG. 1: Crystal structure of orthorhombic perovskite $SrIrO_3$. Sr, Ir and O atoms are shown in aqua, blue and red. The octahedra shown are rotated about the z−axis and tilted about [110]-axis making the unit cell four time bigger than that of the cubic perovskite structure.

However, once the SOC splits the t_{2g} bands into different J_{eff} bands, its effect on the bandwidth of $J_{eff} = 1/2$ is minimal, and the interplay between the SOC and the electron-electron interaction is intriguing. It was claimed that in general the effective spin-orbit coupling is enhanced with increasing strength of the electron-electron interaction leading to the same conclusion that a larger SOC leads to a smaller U_c.[19, 21]

In this paper, we show a counter example where the common wisdom does not apply. We study the interplay between SOC and Hubbard interaction in orthorhombic perovskite oxides (Pbnm). It is found that the bigger the SOC, the larger the U_c in orthorhombic perovskites inherited to the lattice structure. When SOC is moderate (close to the true SOC in $SrIrO_3$), the band dispersion exhibit a line of Dirac node protected by the symmetry of the lattice. We propose that semimetallicity in $SrIrO_3$ compared to insulating Sr_2IrO_4 is due to such a small density of states, which in turn requires a larger U_c for the transition to a Mott insulator. Hubbard interaction in iridates is smaller than this U_c, and thus $SrIrO_3$ remains metallic with small Fermi pockets . Beyond U_c, non-collinear and non-coplanar magnetic structures appear, and the overall phase diagram contains ferromagnetic metal, non-magnetic semimetal and magnetic insulator. Below we will show the band structures computed for $SrIrO_3$, where we use Hubbard U and SOC strength α as tuning parameters to understand different phases realised in other orthorhombic perovskite oxides such as $SrRuO_3$ and $SrRhO_3$. Our findings suggest that the SOC together with Hubbard interaction U plays an important role in realising different ground states in $SrRuO_3$ [22–27], $SrRhO_3$ [4], and $SrIrO_3$ [28–30].

The paper is organised as follows. In the following section, the details about the crystal structure is presented. In Sec. 3, computational method is explained, and the band structures and phase diagram in U vs. SOC are presented in Sec. 4. Magnetic metal and insulator appear at small and large U respectively, and their magnetic ordering patterns depend on the SOC which will be shown in Sec. 5. A brief summary and implications of our findings are listed in the final section.

CRYSTAL STRUCTURE

Fig. 1 shows the crystal structure of the orthorhombic perovskite $SrIrO_3$ with Sr, Ir and O atoms as aqua, blue and red balls. As can be seen in Fig. 1, the octahedra enclosing the Ir atoms are rotated about the $z-$axis and tilted about [110]-axis. Due to these rotations and tilts, there are four formula units of $SrIrO_3$ in a unit cell and the octahedra also get distorted. For any two connected octahedra, the rotations are in the same (opposite) direction if the two enclosed Ir atoms lie in different (the same) layers, whereas the tilts are opposite for all nearest neighbour octahedra.

The experimental lattice parameters of this Pbnm phase of $SrIrO_3$ are $a = 10.5136$ a.u., $b = 10.5688$ a.u. and $c = 14.9$ a.u., and an asymmetrical unit is: a Sr at $(0.5085, 0.4901, 0.25)$, an Ir at $(0.5, 0, 0)$ and two O at $(0.506, 0.073, 0.25)$ and $(0.292, 0.714, 0.044)$ [31].

This structure is primitive orthorhombic for which the symmetry elements include two b glide planes perpendicular to x-axis at $x/a = 1/4$ & $3/4$, two n glide planes perpendicular to y-axis at $y/b = 1/4$ & $3/4$ and two mirror planes perpendicular to z-axis at $z/c = 1/4$ & $3/4$. Here, a b (n) glide plane means that a reflection across the plane followed by a translation of $\mathbf{a}/2$ ($[\mathbf{a}+\mathbf{c}]/2$, i.e, along the diagonal) transforms the structure to self coincidence. Furthermore, there are four 2_1 screw axes parallel to each of the three primitive lattice vectors **a**,**b** and **c**. The 2_1 screw axes parallel to **a** or x-axis are at $(y/b, z/c) = (1/4, 0), (1/4, 1/2), (3/4, 0)$ & $(3/4, 1/2)$; those parallel to **b** or y-axis are at $(x/a, z/c) = (1/4, 1/4), (1/4, 3/4), (3/4, 1/4)$ & $(3/4, 3/4)$; and those parallel to **c** or z-axis are at $(x/a, y/b) = (0, 0), (0, 1/2), (1/2, 0)$ & $(1/2, 1/2)$.

There are eight inversion centres at $x/a, y/b, z/c \in \{0, 1/2\}$. The four Ir atoms in the unit cell sit at four of these. This also means that all the octahedra in Fig. 1 are inversion symmetric. While this is obvious in case of a cubic perovskite structure which forms regular octahedra around the Ir atoms, it is not so in this case where the octahedra are distorted. Two of the 2_1 screw axes parallel to **c** passes through the Ir atoms. These screw axes and the four inversion centres at Ir locations are necessary for the existence of the mirror planes at $z/c = 1/4$ & $3/4$, which connect the octahedra in two different layers through the reflection symmetry. It was found in Ref. [32] that breaking this mirror plane symmetry is a way to generate a strong topological insulator.

FIRST PRINCIPLE CALCULATIONS

We performed density functional theory (DFT) [33, 34] calculations including Hubbard U and SOC using the full-potential linearised augmented-plane-wave (FP-LAPW) method as implemented in the elk code [35]. The local density approximation (LDA) for the exchange and correlation energy functional in the Ceperley-Alder [36] form parametrized by Perdew and Zunger [37] was employed. We used the "around mean field" (AMF) scheme [38] for the double-counting-correction. That is, to correct our DFT+U calculations for the Coulomb repulsion already present in the DFT Hamiltonian. We treated up to $3d$ of Sr, up to $5s$ of Ir excluding $4f$, and $1s$ of O with the radial Dirac equation, while the scaler relativistic approximation is used to include the SOC for the higher states in the second variational step [39].

To confirm that our main results are robust to the choice of double counting correction, we have also computed the band structures using the "fully localized limit" (FLL) correction [40–42] near the phase boundary. We found that at large SOC, U_c is essentially the same. However, for small SOC, U_c is shifted towards a lower value than that found with AMF correction in such a way that our main conclusion (the larger the SOC, the larger the U_c) does not alter. The phase boundaries obtained by these two different corrections are denoted by different colours in the phase diagram shown in Fig. 3, and will be discussed below.

To obtain the phase diagram of $SrIrO_3$ in the U-SOC phase space, we tune the SOC term for the $5d$ orbitals of Ir atoms. Since the strength of the SOC increases sharply with the atomic number Z (as Z^4) , it is much stronger for Ir ($Z = 77$) as compared to Sr ($Z = 38$) or O ($Z = 8$). This means that Ir

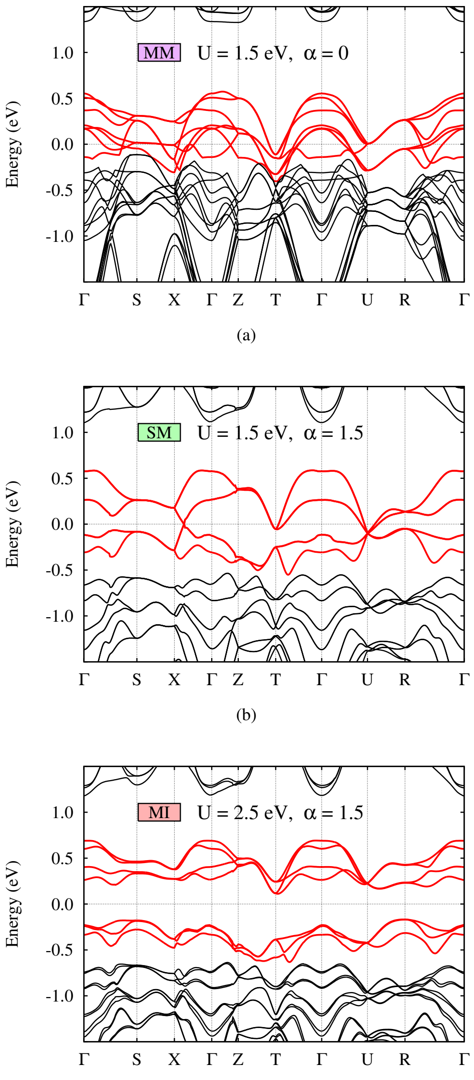

(a)

(b)

(c)

FIG. 2: Some representative band structure diagrams of orthorhombic perovskite oxides for (a) magnetic metal (MM) at $U = 1.5$ eV and $\alpha = 0$, (b) semimetal (SM) at $U = 1.5$ eV and $\alpha = 1.5$, and (c) magnetic insulator at $U = 2.5$ eV and $\alpha = 1.5$. The bands near the Fermi energy are denoted by red color, and remains knotted near U in SM phase.

contributes almost exclusively to the SOC energy in $SrIrO_3$. This allows us to safely tune the SOC for all valence states, because its effect on Sr and O atoms does not count much. A scaling factor α in the SOC term of the Hamiltonian is introduced in the second variational step [39]. This way, we can enhance the effect of SOC by taking $\alpha > 1$ or reduce it by taking $\alpha < 1$. For instance, $\alpha = 0$ would mean no SOC at all, while $\alpha = 1$ is the atomic SOC in Ir atoms. A small magnetic field is used to set the quantisation direction for the angular momentum. This field reduces exponentially to zero during the self consistency iterations so it has no other effects.

In the FP-LAPW method, the real space is divided into spheres around the atoms (muffin-tins) and interstitials elsewhere. In the present calculations, the muffin-tin radii 1.86 a.u. , 2.08 a.u. and 1.51 a.u. are used for Strontium (Sr), Iridium (Ir) and Oxygen (O), respectively. The basis set consists of APW functions with angular momentum l up to 8 and plane waves with cut-off energy equal to 231.3 eV. The number of empty states in the basis set in the second variational step was 10. The Brillouin Zone integrations were performed using a $3 \times 3 \times 3$ grid, which is equivalent to using 10 points in the irreducible part of the Brillouin Zone. This works well, given that the primitive unit cell of orthorhombic perovskite $SrIrO_3$ is almost four times bigger than that of the cubic structure with only one formula unit. We checked the k-grid convergence in the metallic phase using $8 \times 8 \times 8$ grid. We only used U for $5d$ orbitals of Iridium.

BAND STRUCTURES AND PHASE DIAGRAM

The octahedral crystal field splits the bands derived from the d-orbitals of transition metal atoms into high energy e_g and low energy t_{2g} groups. Due to the distortion of octahedra, there are twelve t_{2g} and eight e_g bands (each band is doubly degenerate due to time reversal symmetry). Fig. refrep-bands shows band structures for various values of U and SOC denoted in the inset. The crystal field gap between e_g and t_{2g} is evident for all cases, and only bottom of e_g bands are shown in the plots.

When $\alpha = 0$ that corresponds to the absence of SOC, a ferromagnetic order is present, and t_{2g} bands are all mixed as shown in panel (a). In contrast, when $\alpha = 1.5$, panel (b) and (c), the t_{2g} bands form two groups, the higher four half filled bands originate from the $J_{eff} = 1/2$ denoted by red colour (the lower two bands near Γ point are mainly $J_{eff} = 3/2$ though), and the lower eight completely filled bands from the $J_{eff} = 3/2$. Increasing the SOC increases the splitting between the $J_{eff} = 1/2$ and $J_{eff} = 3/2$ bands.

For smaller U of panel (b), the phase is nonmagnetic semimetal, where four $J_{eff} = 1/2$ bands are near the Fermi level forming small pockets of Fermi surface. While in nonmagnetic semimetal (SM) and magnetic metal (MM) phases, panel (a) and (b), there is a finite density of states at Fermi energy, the band topologies are very different in these two phases. In the non-magnetic semimetallic (SM) phase, the bands at the fermi energy cross near U point resulting in a line node, and the magnetisation is zero everywhere in this phase. In the MM phase, as well as in the magnetic insulator (MI) phase shown in panel (c), there is no such band crossing. In both these phases, Ir atoms have finite magnetic moments with

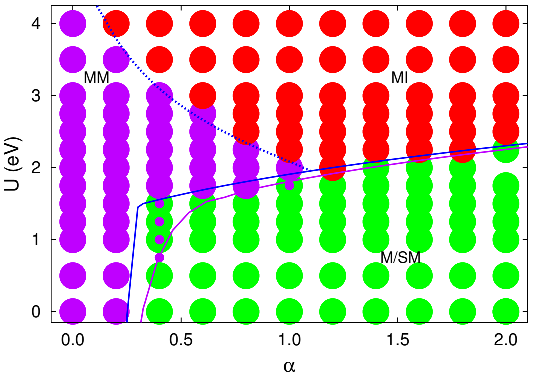

FIG. 3: The phase diagram of orthorhombic perovskite oxides in the U-SOC plane. Three phases for U up to 4 eV and $\alpha = 0 - 2$ are Magnetic Metal (MM), non-magnetic Metal or Semimetal(M/SM), and Magnetic Insulator (MI). The colour circles show the points for which calculations have been performed and magenta, green and red denote MM, M/SM, and MI, respectively. Small magenta circles are FLL results showing MM phase where AFM gives M/SM phase. The solid line separates two phases connected via a first order phase transition (where blue line is obtained by AMF while magenta line is by FLL), whereas the dotted line is the phase boundary for a second order phase transition.

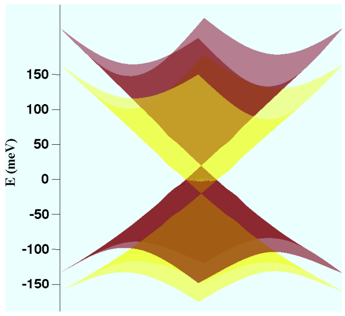

FIG. 4: The $J_{eff} = 1/2$ bands of SrIrO$_3$ close to U in the XURS-plane computed with LDA (without +U) at $\alpha = 1$ (atomic SOC). These bands form two pairs of touching cones shown in yellow and brown. The two pairs are interpenetrated into each other forming a circular nodal line at the fermi energy. When the time reversal symmetry is broken (as the magnetic ordering occurs), these band crossings disappear and a band gap form.

a long range order. Increasing U, keeping the same strength of SOC, leads to a metal-insulator transition at a critical U_c, where the insulating state such as panel (c) has an interesting magnetic ordering pattern. Since the time reversal symmetry is broken due to the magnetic ordering, there are eight $J_{eff} = 1/2$ bands in this phase as displayed in panel (c). A further discussion about the magnetic ordering pattern will be presented below.

These three electronic phases shown in Fig. 2 are found in the U-SOC phase diagram; (*i*) M/SM, (*ii*) MM, and (*iii*) MI. The overall phase diagram in U vs. SOC is presented in Fig. 3, where M/SM, MM, and MI are shown in green, magenta, and red. M/SM is connected to MM and MI via a first order phase transition whereby the magnetisation jumps from zero to a finite value along with a sudden change in the band structure topology. On the other hand, MM and MI transform into one another continuously with opening or closing up of a band gap.

Let us discuss the phase diagram by checking along different cuts. First vertical cuts, i.e., changing U for a given α. When $\alpha = 0$, the system remains a pure ferromagnetic metal at all U. This results from a large density of states at the Fermi level leading to a Stoner ferromagnet. Tuning SOC to finite but still small values (for $\alpha < 0.3$), U interaction does not make any difference, and system stays in the magnetic metal phase even for very high values of U (for U close to 5eV, it becomes ferromagnetic insulator, which is not shown here). However, as the SOC does not favour a pure ferromagnetic ordering, it turns the magnetic ordering pattern to a slightly non-coplanar order with a large ferromagnetic component. In contrast, for $\alpha > 0.3$, increasing U induces a first order phase transition from non-magnetic semimetal to magnetic phases. Whether the magnetic phase is metal or insulator depends on the strengths of both U and α. The phase boundary separating the non-magnetic semimetal phase from the two other phases, MM and MI, is shown as a solid line in Fig. 3. For $\alpha > 1.1$, increasing U transforms M/SM directly to MI, while for $0.3 < \alpha < 1.1$, increasing U changes the phase from non-magnetic metal, to magnetic metal followed by magnetic insulator.

Let us explore the phase diagram using horizontal cuts – changing α for a fixed U. For small U, increasing α leads to a first order phase transition from magnetic metal to non-magnetic metal/semimetal phase. The critical value of α, α_c, at which this transition takes place stays between $0.2 - 0.4$ for $0 \leq U < 1.5$ eV. This is rather expected, as SOC disfavours spin density wave ordering within a weak coupling theory. Fig. 3 shows results for α up to 2. As can be seen, there is no further phase transitions by increasing α. We checked this for α up to 5.

For $U \geq 1.5$ eV, α_c increases sharply with U with an increasing separation between the bands at the Fermi level in magnetic metal phase. It is also interesting to note that for $2 \leq U \leq 2.35$ eV, the system undergoes a change in phase by increasing α from magnetic metal to magnetic insulator, and then into non-magnetic semimetal, i.e, a re-entrance of metallicity (metal-insulator-metal by changing SOC for a given U). For $U \geq 2.35$ eV, increasing α transforms magnetic metal smoothly to magnetic insulating phase with opening up of a band gap. The higher the value of U, the lower is the value of α for this transition. The phase boundary between these two phases is shown as a dotted line in Fig. 3.

As can be seen in Fig. 3, the dotted line have the expected phase boundary curvature in the U-SOC plane. That is, the critical value of U for MM to MI transition decreases with increasing α since the phase space of magnetic insulator should be wider as U increases. However, the most unexpected result presented in Fig. 3 is the opposite phase boundary curvature for transition to magnetic phases from non-magnetic metallic phase, the solid line. It shows that a stronger SOC requires a stronger electron-electron interaction to transform non-magnetic metal to magnetic insulator. The origin of this unexpected behaviour is likely to be the special band topology in the semimetal phase as described below.

Fig. 4 shows the band structure near U in the XURS-plane. The four $J_{eff} = 1/2$ bands form two interpenetrated pairs of cones, each pair consisting of a lower and a higher band (a yellow and a brown). One pair touches below the fermi level while the other above it, forming two Dirac-like points and a circular line node in the XURS-plane at the fermi energy. Due to this node, there is an extremely small density of states near the Fermi level, which in turn requires a high Hubbard U to splits these cones resulting in a magnetic insulator. We propose that this is the main mechanism whereby $SrIrO_3$ is a semimetal with a small carrier density, different from its sister compounds Sr_2IrO_4 [12, 43–45] and $Sr_3Ir_2O_7$ [46–48].

We also checked the bandwidth of the upper two bands of $J_{eff} = 1/2$ at the Fermi level when SOC is large enough to separate $J_{eff} = 1/2$ top two bands from the rest (except at the nodal points). W is plotted in Fig. 5 against α for various values of U for $\alpha \geq 0.5$, since $\alpha < 0.5$, $J_{eff} = 1/2$ is not well defined. Contrary to the expectation [20], the bandwidth increases with α and U in the non-magnetic semi-metallic phase most likely due to a steeper slope of Dirac node that confirms our conclusion above. Whereas in the magnetic phases (the plots for $U = 2.5 - 5$ eV), W decreases with α and U as expected. This makes us believe that the transition from the non-magnetic to magnetic phases in $SrIrO_3$ is controlled by the electronic state of the non-magnetic semimetal where the bandwidth is not relevant. This is further supported by the fact that the semimetal phase has a special band topology as described below.

J. M. Carter *et al* showed in Ref. [32] using a tight binding model that this line node is proteced by the lattice symmetry. In other words, any term that opens up a gap near U-point should break either time reversal, inversion, or Pbnm lattice symmetry. For example, it was shown that when the mirror symmetry between the two layers of IrO_2 in $SrIrO_3$ is broken with a staggered potential, this line node changes to a point node. When the strength of this staggered potential is increased beyond a critical value that takes the node to the R point, a change in the topology of the bands occurs owing to the inversion of the $J_{eff} = 1/2$ bands at R. The system is turned into a strong topological insulator when this happens. Further increase of this staggered potential leads to inversion of the bands at Z point, changing the band topology back to trivial, making the system a band insulator.

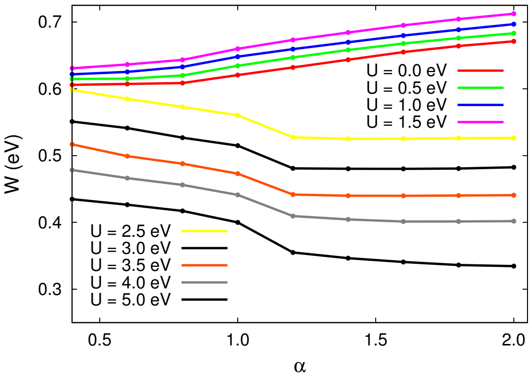

FIG. 5: The bandwidth W of top two bands at fermi level as a function of α for various values of U. W decreases with α and U in MM/MI phase ($U \geq 2.5$ eV) as expected but increases in SM phase ($U \leq 1.5$ eV).

MAGNETIC ORDERING PATTERNS

As discussed above, when $\alpha = 0$, there is a pure ferromagnetic (FM) order in the MM phase at all values of U. This happens down to $U = 0$, because the electron-electron repulsion is not completely absent even at $U = 0$, partly due to its imperfect removal in the $5d$ orbitals of Ir and partly due to the presence of many other occupied states in the system. The magnitude of the magnetic moment of Ir depends on U. It increases with U from $0.38\mu_B$ at $U = 0$ to $0.95\mu_B$ at $U = 4$ eV, where it is almost saturated — a rather expected behaviour. A small contribution to the magnetisation also comes from O when $\alpha \sim 0$.

As we move away from $\alpha = 0$, system develops a canted antiferromagnetic (CAFM) order. At smaller U, transition from FM to CAFM is more gradual leaving a net ferromagnetic component. This behaviour persists up to $\alpha \sim 1$. For higher α a very small ferromagnetic component develops in the magnetic insulator phase at higher U. This is expected since an antiferromagnetic order in the insulating phase lowers the energy via virtual hopping of electrons to the nearest neighbour with the oppositely aligned spin. A small ferromagnetic component is then due to an effective Dzyalonshinsky-Moriya interaction as found in Sr_2IrO_4 [12, 17, 49]. Fig. 6 shows the magnetic structure at $\alpha = 0.2$ as U is changed from 2 to 4 eV, and at $U = 4$ eV as α is changed from 0.2 to 1. The quantisation axis is set along the x-axis.

For any two nearest neighbour Ir atoms in different layers along **c** (i.e, those with yellow and green or red and blue arrows in Fig. 6) the components of moments along the y and the z-axis are always cancelled out. The size and orientation/direction of individual moments depend on the values of α and U as does their sum or the total moment per unit cell. As can be seen in Fig. 6(a), at $U = 2$ eV and $\alpha = 0.2$, the mo-

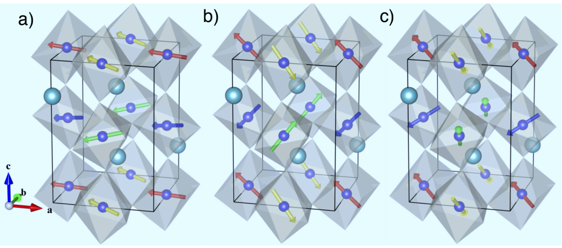

FIG. 6: The magnetic structure of orthorhombic perovskite oxides at $U = 2$ eV and $\alpha = 0.2$ (a), $U = 4$ eV and $\alpha = 0.2$ (b), $U = 4$ eV and $\alpha = 1$ (c). In (a), the system has a canted antiferromagnetic order with a large ferromagnetic component. In (b), the system has a canted antiferromagnetic order with negligible ferromagnetic component. The average magnetisation per unit cell is also zero in (c), but the moments are aligned in a very different way.

ments are almost co-planer with a large ferromagnetic component. Fig. 6(b) shows the magnetic order at $U = 4$ eV and $\alpha = 0.2$. It is clear from this figure that raising the strength of Coulomb interaction at finite α suppresses the ferromagnetic component. The magnetic order at the same value of U (4 eV) and a higher α, $\alpha = 1$, is shown in Fig. 6(c), where a stronger SOC has changed the orientations and reduced the sizes of the individual moments.

DISCUSSION AND SUMMARY

The SOC is an essential ingredient in numerous exciting phenomena including spintronics and topological insulators. However, in transition metal oxides with 3d orbitals such as high temperature cuprates, the SOC has been ignored, while the strong correlation represented by Hubbard interaction determines their physical properties. Very recently, iridates with 5d-orbital has been a topic of much attractive research due to intriguing combined effects of the SOC and Hubbard interaction. It was found that the SOC in iridates is unusually strong, which differs from other 5d compounds such as Re-oxides [50] even though the atomic SOC should be similar for Ir and Re.

A set of iridates is the perovskite iridates forming Ruddlesden Popper series from single layer Sr_2IrO_4 to three dimensional structure $SrIrO_3$. While both single layer and bilayer iridates exhibit a magnetic insulating behavior, $SrIrO_3$ shows a metallic phase with a small number of charge carriers. Given that the SOC and Hubbard interaction are local, their strengths should be similar in this series, and thus it was suggested that the bandwidth should control metal-insulator transition as the number of layers changes in perovskite iridates.[20] Here we show that the metallicity is innate to the lattice structure of three dimensional orthorhombic perovskites in addition to a large SOC. Due to this combined effect, there are tiny hole and electron Fermi pockets with small density of states, which in turn makes Hubbard interaction less efficient in $SrIrO_3$. Due to strong SOC, the magnetic field dependence of physical properties would be interesting to study.

We investigate an overall phase diagram of the orthorhombic perovskite structure (space group Pbnm) in U vs. SOC using density functional theory. The computation is based on $SrIrO_3$, where tuning U and SOC (by changing α) allows us to explore other possible phases nearby non-magnetic semimetal in isostructural systems. Three phases – non-magnetic metal/semimetal, magnetic metal, and magnetic insulator – were found by tuning U and SOC. At smaller α, a magnetic metal is always found, which is similar to $SrRuO_3$. While Ru^{4+} has 4 electrons at the outer shell and thus the chemical potential is different from $SrRhO_3$, the bands near the Fermi level are strongly mixed leading to a similar phenomena. Indeed, earlier electronic calculation on $SrRuO_3$ reported it a ferromagnetic metal.At $\alpha > 0.3$ and $U < 1.5eV$, the system becomes non-magnetic metal which resembles the ground state of $SrRhO_3$. Indeed, our computations of the electronic structure of $SrRhO_3$ shows that it is similar to the one found at $\alpha = 0.4$ close to the instability towards magnetic metallic phase. While Rh and Ru are next to each other in the periodic table, our results imply that the SOC must have a stronger effect on $SrRhO_3$ than $SrRuO_3$, and agree with an earlier suggestion that $SrRhO_3$ is near a magnetic critical point [4–6]. Increasing α further, the bands near the Fermi level changes to semimetallic-like, and a stronger U_c is required for a magnetic insulator. The shape of phase boundary between the non-magnetic semimetal and the magnetic insulator is emerged from a line of Dirac node leading a small density of states near the Fermi level. A tight binding approach for a series of $Sr_{n+1}Ir_nO_{3n+1}$ has found the same conclusion that U_c is larger for $n = \infty$ than $n = 1$ or $n = 2$.[51]

In summary, we have studied the interplay between the SOC and Hubbard interaction in orthorhombic perovskite oxide with the point group symmetry of Pbnm. Three different phases were identified. A magnetic metal with a finite ferromagnetic component found in smaller SOC at all values of U investigated in this study. Increasing the SOC leads to a phase transition to a non-magnetic metal for small U, and to a magnetic insulator for large U. The detailed band structures near the Fermi level in these phases strongly depend on the strength of the SOC rather than U, unless the interaction U leads to another magnetic phase. Our study may be useful in understanding different ground states found among isostructural perovskites including $SrRuO_3$, $SrRhO_3$, and $SrIrO_3$. It also provides a microscopic mechanism for semimetallic behaviour in $SrIrO_3$ distinct from its sister compounds, Sr_2IrO_4 and $Sr_3Ir_2O_7$.

[1] G. Cao, S. McCall, M. Shepard, J. E. Crow, and R. P. Guertin, Phys. Rev. B 56, 321 (1997).

[2] Y. Kats, L. Klein, J. W. Reiner, T. H. Geballe, M. R. Beasley,

and A. Kapitulnik, Phys. Rev. B 63, 054435 (2001).

[3] Y. J. Chang, C. H. Kim, S.-H. Phark, Y. S. Kim, J. Yu, and T.W. Noh, Phys. Rev. Lett. 103, 057201 (2009).

[4] K. Yamaura and E. Takayama-Muromachi, Phys. Rev. B 64, 224424 (2001).

[5] T. Shimura, M. Itoh, and T. Nakamura, J. Solid State Chem. 98, 198 (1992).

[6] D. J. Singh, Phys. Rev. B 67, 054507 (2003).

[7] H. Takagi, private communication.

[8] J. M. Longo, J.A. Kafalas, and R.J. Arnott, J. Solid State Chem. 3, 174 (1971).

[9] Y. X. Liu, H. Masumoto, and T. Goto, Mater. Trans. 46, 100 (2005).

[10] W. D. Ryden, A. W. Lawson, and C. C. Sartain, Phys. Rev. B 1, 1494 (1970).

[11] S. J. Moon, Hosub Jin, W. S. Choi, J. S. Lee, S. S. A. Seo, J. Yu, G. Cao, T. W. Noh, Y. S. Lee, Phys. Rev. B 80, 195110 (2009).

[12] B. J. Kim, Hosub Jin, S. J. Moon, J.-Y. Kim, B.-G. Park, C. S. Leem, J. Yu, T. W. Noh, C. Kim, S.-J. Oh, J.-H. Park, V. Durairaj, G. Cao, and E. Rotenberg, Phys. Rev. Lett. 101, 076402 (2008).

[13] H. Watanabe, T. Shirakawa, and S. Yunoki, Phys. Rev. Lett. 105, 216410 (2010).

[14] C. Martins, M. Aichhorn, Loïg Vaugier, and S. Biermann, Phys. Rev. Lett. 107, 266404 (2011).

[15] R. Arita, J. Kunes, A. V. Kozhevnikov, A. G. Eguiluz, and M. Imada, Phys. Rev. Lett. 108, 086403 (2012).

[16] S. Fujiyama, H. Ohsumi, T. Komesu, J. Matsuno, B. J. Kim, M. Takata, T. Arima, and H. Takagi, Phys. Rev. Lett. 108, 247212 (2012).

[17] B. J. Kim, H. Ohsumi, T. Komesu, S. Sakai, T. Morita, H. Takagi, T. Arima, Science 323,1329 (2009).

[18] H. Jin, H. Jeong, T. Ozaki, and J. Yu, Phys. Rev. B 80, 075112 (2009).

[19] Guo-Qiang Liu, V. N. Antonov, O. Jepsen, and O. K. Andersen, Phys. Rev. Lett. 101, 026408 (2008).

[20] S. J. Moon, H. Jin, K. W. Kim, W. S. Choi, Y. S. Lee, J. Yu, G. Cao, A. Sumi, H. Funakubo, C. Bernhard, and T. W. Noh, Phys. Rev. Lett. 101, 226402 (2008).

[21] D. Pesin and L. Balents, Nature Phys. 6, 376 (2010).

[22] B. C. Chakoumakos, S. E. Nagler, S. T. Misture and H. M. Christen, Phyica B 241, 358 (1998).

[23] J. J. Hamlin, S. Deemyad, J. S. Schilling, M. K. Jacobsen, R. S. Kumar, A. L. Cornelius, G. Cao, and J. J. Neumeier, Phys. Rev. B 76, 014432 (2007).

[24] C. S. Alexander, S. McCall, P. Schlottmann, J. E. Crow, and G. Cao, Phys. Rev. B 72, 024415 (2005).

[25] D. Kim, B. L. Zink, F. Hellman, S. McCall, G. Cao, and J. E. Crow, Phys. Rev. B 67, 100406(R) (2003).

[26] J. S. Ahn, J. Bak, H. S. Choi, T. W. Noh, J. E. Han, Y. Bang, J. H. Cho, and Q. X. Jia, Phys. Rev. Lett. 82, 5321 (1999).

[27] X. Ke, M. S. Rzchowskia, L. J. Belenky, and C. B. Eom, Appl. Phys. Lett. 84, 5458 (2004).

[28] G. Cao, V. Durairaj, S. Chikara, L. E. DeLong, S. Parkin, and P. Schlottmann, Phys. Rev. B 76, 100402(R) (2007).

[29] M. A. Laguna-Marco, D. Haskel, N. Souza-Neto, J. C. Lang, V. V. Krishnamurthy, S. Chikara, G. Cao, and M. van Veenendaal, Phys. Rev. Lett. 105, 216407 (2010).

[30] S. Y. Jang, H. Kim, S. J. Moon, W. S. Choi, B. C. Jeon, J. Yu, and T. W. Noh, J. Phys.: Condens. Matter 22, 485602 (2010).

[31] J. G. Zhao, L. X. Yang, Y. Yu, F. Y. Li, R. C. Yu, Z. Fang, L. C. Chen, and C. Q. Jin, Jour. of Appl. Phys. 103, 103706 (2008).

[32] J.-M. Carter, V. V. Shankar, M. A. Zeb, and H.-Y. Kee, Phys. Rev. B 85, 115105 (2012).

[33] P. Hohenberg and W. Kohn, Phys. Rev. 136, 864 (1964).

[34] W. Kohn and L. J. Sham, Phys. Rev. 140, 1133 (1965).

[35] http://elk.sourceforge.net .

[36] D. M. Ceperley and B. J. Alder, Phys. Rev. Lett. 45, 566 (1980).

[37] J. P. Perdew and A. Zunger, Phys. Rev. B 23, 5048 (1981).

[38] M. T. Czyżyk and G. A. Sawatzky, Phys. Rev. B 49, 14211 (1994).

[39] D. D. Koelling and B. N. Harmon, J. Phys. C: Solid State Phys 10, 3107 (1977).

[40] V. I. Anisimov, I. V. Solovyev, M. A. Korotin, M. T. Czyżyk and G. A. Sawatzky, Phys. Rev. B 48, 16929 (1993).

[41] A. I. Liechtenstein, V. I. Anisimov, and J. Zaanen, Phys. Rev. B 52, R5467 (1995).

[42] E. R. Ylvisaker, W. E. Pickett, and K. Koepernik, Phys. Rev. B 79, 035103 (2009).

[43] M. K. Crawford, M. A. Subramanian, R. L. Harlow, J. A. Fernandez-Baca, Z. R. Wang, and D. C. Johnston, Phys. Rev. B 49, 9198 (1994).

[44] T. Shimura, Y. Inaguma, T. Nakamura, and M. Itoh, and Y. Morii, Phys. Rev. B 52, 9143 (1995).

[45] J. Kim, D. Casa, M. H. Upton, T. Gog, Y.-J. Kim, J. F. Mitchell, M. van Veenendaal, M. Daghofer, J. van den Brink, G. Khaliullin, and B. J. Kim, Phys. Rev. Lett. 108, 177003 (2012)

[46] G. Cao, J. Bolivar, S. McCall, J. E. Crow, and R. P. Guertin, Phys. Rev. B 57, 11039(R) (1998).

[47] G. Cao,Y. Xin, C. S. Alexander, J. E. Crow, P. Schlottmann, M. K. Crawford, R. L. Harlow, and W. Marshall, Phys. Rev. B 66, 214412 (2002).

[48] I. Nagai, Y. Yoshida, S. I. Ikeda, H. Matsuhata, H. Kito, and M. Kosaka, J. Phys.: Condens. Matter 19, 136214 (2007).

[49] G. Jackeli and G. Khaliullin, Phys. Rev. Lett. 102, 017205 (2009).

[50] J. P. Clancy, N. Chen, C. Y. Kim, W. F. Chen, K. W. Plumb, B. C. Jeon, T. W. Noh, Y.-J. Kim, arXiv:1205.6540

[51] Jean-Michel Carter and Hae-Young Kee, arXiv:1207.2183.